

# NANOSECOND UPCONVERSION OPTICAL PARAMETRIC OSCILLATORS

A DISSERTATION SUBMITTED TO  
THE DEPARTMENT OF ELECTRICAL AND ELECTRONICS  
ENGINEERING  
AND THE INSTITUTE OF ENGINEERING AND SCIENCE  
OF BILKENT UNIVERSITY  
IN PARTIAL FULFILLMENT OF THE REQUIREMENTS  
FOR THE DEGREE OF  
DOCTOR OF PHILOSOPHY

By  
Ziya Gürkan Figen  
September, 2005

I certify that I have read this thesis and that in my opinion it is fully adequate, in scope and in quality, as a dissertation for the degree of doctor of philosophy.

---

Prof. Dr. Orhan Aytür (Supervisor)

I certify that I have read this thesis and that in my opinion it is fully adequate, in scope and in quality, as a dissertation for the degree of doctor of philosophy.

---

Prof. Dr. Ayhan Altıntaş

I certify that I have read this thesis and that in my opinion it is fully adequate, in scope and in quality, as a dissertation for the degree of doctor of philosophy.

---

Prof. Dr. Ekmel Özbay

I certify that I have read this thesis and that in my opinion it is fully adequate, in scope and in quality, as a dissertation for the degree of doctor of philosophy.

---

Prof. Dr. Levent Gürel

I certify that I have read this thesis and that in my opinion it is fully adequate, in scope and in quality, as a dissertation for the degree of doctor of philosophy.

---

Prof. Dr. Cengiz Beşikçi

Approved for the Institute of Engineering and Science:

---

Prof. Dr. Mehmet Baray  
Director of the Institute

*dedicated to my father,  
who fights bravely and patiently  
against the unexpected*

# ABSTRACT

## NANOSECOND UPCONVERSION OPTICAL PARAMETRIC OSCILLATORS

Ziya Gürkan Figen

Ph.D. in Electrical and Electronics Engineering

Supervisor: Prof. Dr. Orhan Aytür

September, 2005

In this thesis, we demonstrate a technique for highly efficient red beam generation using nanosecond upconversion optical parametric oscillators based on  $\text{KTiOAsO}_4$  crystals that are simultaneously phase matched for optical parametric generation and sum-frequency generation. Pumped at a wavelength of 1064 nm by a  $Q$ -switched Nd:YAG laser, these devices produce red output beams at 627 nm with 1064-nm-to-627-nm energy conversion efficiencies reaching 20% for the single-pass pumping and 30% for the double-pass pumping. Our devices are simpler in architecture compared to other devices converting nanosecond Nd:YAG laser radiation into red wavelengths. A typical nanosecond upconversion optical parametric oscillator is comprised of three cavity mirrors which are all high reflectors at the signal wavelength (1525 nm), a 2-cm-long  $\text{KTiOAsO}_4$  crystal, and an intracavity retarder plate for rotating the polarization of the signal beam. The total cavity length is under 5 cm. With its small size, the device can be shaped into a module to be placed in front of Nd:YAG lasers for highly efficient red beam generation. The single-pass sum-frequency generating optical parametric oscillator is the first demonstration of a nanosecond optical parametric oscillator using simultaneous phase matching. We have fully characterized these devices in terms of their energy output as functions of polarization rotation angle and input pump energy, time profiles, spatial beam profiles, and spectra of the output. In this thesis, we also present our work on modelling continuous-wave intracavity optical parametric oscillators.

*Keywords:* nonlinear frequency conversion, optical parametric oscillators, sum-frequency generation, simultaneous phase matching,  $Q$ -switched Nd:YAG laser, red beam generation, modelling continuous-wave intracavity optical parametric oscillators.

## ÖZET

# NANOSANIYE YUKARI-ÇEVİRİM OPTİK PARAMETRİK OSİLATÖRLERİ

Ziya Gürkan Figen

Elektrik ve Elektronik Mühendisliği, Doktora

Tez Yöneticisi: Prof. Dr. Orhan Aytür

Eylül, 2005

Bu tezde, optik parametrik üretim ile toplam-frekans üretiminin aynı anda faz uyumunun sağlandığı  $\text{KTiOAsO}_4$  kristallerine dayalı, nanosaniye yukarı-çevirim optik parametrik osilatörleri kullanarak yüksek verimli kırmızı ışın üretimi için bir teknik gösteriyoruz.  $Q$ -anahtarlanmış bir Nd:YAG lazeri tarafından 1064 nm dalgaboyunda pompalandığında bu cihazlar, 1064 nm dalgaboyundan 627 nm dalgaboyuna enerji dönüşüm verimi tek-geçiş pompalama için %20'e ve iki-geçiş pompalama için %30'a varan 627 nm dalgaboyunda kırmızı çıktı üretmektedirler. Cihazlarımız, nanosaniye Nd:YAG lazer ışınmasını kırmızı dalgaboylarına dönüştüren diğer cihazlarla karşılaştırıldığında daha basit bir mimari yapıdadırlar. Tipik bir nanosaniye yukarı-çevirim optik parametrik osilatörü, sinyal dalgaboyunda (1525 nm) hepsi yüksek yansıtıcı olan üç kovuk aynasından, 2-cm uzunluğunda bir  $\text{KTiOAsO}_4$  kristalinden ve sinyal ışımının polarizasyonunu döndürmek için bir kovuk-içi geciktirici plakadan oluşmaktadır. Toplam kovuk uzunluğu 5 cm'nin altındadır. Küçük boyutları olan cihaz, yüksek verimli kırmızı ışın üretimi için, Nd:YAG lazerlerinin önüne konulmak üzere bir modül şekline sokulabilir. Tek-geçişli toplam-frekans üreten optik parametrik osilatör, aynı anda faz uyumu sağlanmış nanosaniye bir optik parametrik osilatörün ilk kez gösterilişidir. Bu cihazları, polarizasyon döndürme açısının ve giriş pompa enerjisinin bir fonksiyonu olan enerji çıktıları, çıkış zaman profilleri, uzaysal ışın profilleri ve spektrumları bakımından etraflıca karakterize ettik. Bu tezde ayrıca, sürekli-dalga kovuk-içi optik parametrik osilatörlerin modellenmesi konusundaki çalışmamızı sunuyoruz.

*Anahtar sözcükler:* doğrusal olmayan frekans dönüştürme, optik parametrik osilatörler, toplam frekans üretimi, aynı anda faz uyumu sağlama,  $Q$ -anahtarlanmış Nd:YAG lazeri, kırmızı ışın üretimi, sürekli-dalga kovuk-içi optik parametrik osilatörlerin modellenmesi.

# Acknowledgement

I would like to express my sincere gratitude to my supervisor Prof. Dr. Orhan Aytür for his guidance, suggestions and encouragement throughout the development of this thesis and especially for giving me the opportunity to work in a wonderful laboratory.

I am deeply grateful to Prof. Dr. Ekmel Özbay for the equipment, financial support and help that he provided for me during my Ph.D. studies.

I would like to express my special thanks to the members of the thesis committee for showing keen interest to the subject matter and reviewing the thesis.

I would like to also express my special thanks to Birol Erentürk of ASELSAN, Inc. for providing some of the equipment that we used in our experiments.

I would like to thank Prof. Dr. J. Gary Eden of University of Illinois at Urbana-Champaign who introduced me to the field of optics and has been a wonderful friend.

I would also like to express my thanks to the academicians at the Electrical and Electronics Department of Gazi University, Prof. Dr. Müzeyyen Sarıtaş, Prof. Dr. Sezai Dinçer, Prof. Dr. Cengiz Taplamacıoğlu, Assist. Prof. Dr. Timur Aydemir, Assist. Prof. Dr. Cem Nakiboğlu, and others for their support and understanding during the initial years of my Ph.D. studies.

I would like thank Assist. Prof. Dr. Vakur Ertürk, Dr. Tolga Kartaloğlu, Dr. Murat Akgül, and Assist. Prof. Dr. Güçlü Köprülü for their help and support. Special thanks to the department secretary Mürüvet Parlakay and the laboratory technicians Ersin Başar and Ergün Hırlakoğlu for their help.

I would like to thank my parents and my sister for their love and support that they gave me all my life without asking for any return. Special thanks to my brother-in-law for his strong support.

# Contents

<b>1</b>	<b>Introduction</b>	<b>1</b>
<b>2</b>	<b>Optical Parametric Interactions</b>	<b>12</b>
2.1	Nonlinear Polarization . . . . .	13
2.2	Second-order Nonlinear Polarization . . . . .	14
2.3	Coupled-Mode Equations . . . . .	15
2.4	Sum-Frequency Generation . . . . .	18
2.5	Second-Harmonic Generation . . . . .	21
2.6	Optical Parametric Amplifier . . . . .	22
2.7	Optical Parametric Oscillator . . . . .	24
2.8	Simultaneously Phase-Matched Interactions . . . . .	27
2.9	Phase Matching . . . . .	31
2.9.1	Birefringent Phase Matching . . . . .	31
2.9.2	Quasi-Phase Matching . . . . .	34
2.9.3	Simultaneous Phase Matching with BPM . . . . .	35

2.9.4	Simultaneous Phase Matching with QPM . . . . .	37
<b>3</b>	<b>Nanosecond OPO Experiments</b>	<b>39</b>
3.1	Potassium Titanly Arsenate (KTA) Crystal . . . . .	40
3.2	Experimental Configuration . . . . .	42
3.3	Characterization . . . . .	44
3.4	OPOs Based on Crystal-1 . . . . .	45
3.4.1	Output Energy versus Input Energy . . . . .	46
3.4.2	Time Profiles . . . . .	47
3.4.3	Signal Spectra . . . . .	50
3.5	OPOs Based on Crystal-2 . . . . .	51
3.5.1	Output Energy versus Input Energy . . . . .	52
3.5.2	Time Profiles . . . . .	54
3.5.3	Signal Spectrum . . . . .	54
3.6	OPOs Based on Crystal-3 . . . . .	55
3.6.1	Output Energy versus Input Energy . . . . .	56
3.6.2	Time Profiles . . . . .	57
3.6.3	Signal Spectrum . . . . .	57
3.7	Summary . . . . .	58
<b>4</b>	<b>Nanosecond SF-OPO Experiments</b>	<b>59</b>
4.1	Experimental Configurations . . . . .	60

4.1.1	Single-pass SF-OPO Based on Crystal-2 . . . . .	60
4.1.2	Double-pass and Single-pass SF-OPOs Based on Crystal-3 . . . . .	63
4.2	Characterization . . . . .	65
4.3	Results for the Single-Pass SF-OPO Based on Crystal-2 . . . . .	66
4.3.1	Output Energy versus Polarization Rotation Angle . . . . .	66
4.3.2	Output Energy versus Input Energy . . . . .	68
4.3.3	Time Profiles . . . . .	69
4.3.4	Spectra of the Pump and Sum-Frequency . . . . .	70
4.3.5	Spatial Profiles of the Sum-Frequency Beam . . . . .	72
4.3.6	Simultaneous Phase-Matching Angle and Signal Wavelengths with Angle-Tuning . . . . .	72
4.3.7	Single-Pass Crystal-2 SF-OPO with Output Coupler . . . . .	75
4.4	Results for the Double-Pass and Single-Pass SF-OPOs Based on Crystal-3 . . . . .	78
4.4.1	Output Energy versus Polarization Rotation Angle . . . . .	78
4.4.2	Output Energy versus Input Energy . . . . .	79
4.4.3	Time Profiles . . . . .	81
4.4.4	Spectrum of the Sum-Frequency . . . . .	82
4.4.5	Spatial Profiles of the Sum-Frequency Beam . . . . .	83
4.4.6	Simultaneous Phase-Matching Angle and Signal Wavelengths with Angle-Tuning . . . . .	83
4.5	Numerical Modelling . . . . .	85

4.5.1	Models for Nanosecond OPOs . . . . .	85
4.5.2	Numerical Model for the SF-OPO . . . . .	86
4.5.3	Predictions of the Model and Discussion . . . . .	90
4.6	Summary . . . . .	93
<b>5</b>	<b>Plane-Wave Modelling of cw IOPO</b>	<b>94</b>
5.1	Device Configuration, Operation and Model Assumptions . . . . .	96
5.2	Laser Equations . . . . .	100
5.3	Travelling-Wave IOPO Equations . . . . .	102
5.4	Results and Conclusions . . . . .	106
5.4.1	Example-1 . . . . .	107
5.4.2	Example-2 . . . . .	110
5.4.3	Example-3 . . . . .	112
<b>6</b>	<b>Conclusions</b>	<b>118</b>

# List of Figures

2.1	Photon flux densities for $\Delta kl = 0, 2, 10,$ and $50.$ . . . . .	19
2.2	Evolution of the photon flux densities for SHG. . . . .	22
2.3	Evolution of the photon flux densities for the OPA. . . . .	24
2.4	Signal gain ( $G$ ) as a function of the normalized signal photon flux density at the input. . . . .	26
2.5	Dependence of the refractive index on light propagation direction. . . . .	32
2.6	Phase-matching geometries for the three-wave mixing process. . . . .	34
2.7	Polarization diagram for our SF-OPO. . . . .	36
3.1	Experimental setup for the OPO. . . . .	42
3.2	Spatial profile of the pump beam. . . . .	43
3.3	Signal energy, energy conversion efficiency and pump depletion of the crystal-1 OPO as functions of input pump energy. . . . .	46
3.4	Time profiles of the pump and depleted pump pulses of the crystal-1 OPO with the $R = 85\%$ OC for various pump energies. . . . .	48
3.5	Time profiles of the signal pulse of the crystal-1 OPO with the $R = 85\%$ OC for various pump energies. . . . .	49

3.6	Time profiles of the pump, depleted pump and signal of the crystal-1 OPO with the $R = 74\%$ OC. . . . .	50
3.7	Spectra of the signal beam of the crystal-1 OPO. . . . .	51
3.8	Signal energy, energy conversion efficiency and pump depletion of the crystal-2 OPO as functions of input pump energy. . . . .	52
3.9	Time profiles of the pump, depleted pump and signal of the crystal-2 OPO with the $R = 85\%$ OC. . . . .	54
3.10	Spectrum of the signal beam of the crystal-2 OPO. . . . .	55
3.11	Signal energy, energy conversion efficiency and pump depletion of the crystal-3 OPO as functions of input pump energy. . . . .	56
3.12	Time profiles of the pump, depleted pump and signal of the crystal-3 OPO with the $R = 74\%$ OC. . . . .	57
3.13	Spectrum of the signal beam of the crystal-3 OPO. . . . .	58
4.1	Experimental setup for the single-pass SF-OPO. . . . .	62
4.2	Spatial profile of the pump beam of the single-pass SF-OPO based on crystal-2. . . . .	63
4.3	Experimental setup for the double-pass SF-OPO. . . . .	64
4.4	Energy conversion efficiency as a function of polarization rotation angle of the crystal-2 SF-OPO. . . . .	67
4.5	Output energy as a function of pump energy of the crystal-2 SF-OPO. . . . .	68
4.6	Optimum polarization rotation angle and maximum energy conversion efficiency as functions of pump energy. . . . .	69
4.7	Time profiles of the pulses of the crystal-2 SF-OPO. . . . .	70

4.8	Spectra of the pump and sum-frequency beams of the crystal-2 SF-OPO. . . . .	71
4.9	Spatial profiles of the sum-frequency beam of the single-pass crystal-2 SF-OPO. . . . .	71
4.10	Sum-frequency energy with angle-tuning for the crystal-2 SF-OPO.	73
4.11	Tuning curves of the signal wavelength. . . . .	74
4.12	Energy conversion efficiencies as a function of $\alpha$ of the crystal-2 SF-OPO with the $R = 85\%$ OC. . . . .	75
4.13	Sum-frequency energy as a function of pump energy of the crystal-2 SF-OPO with the $R = 85\%$ OC. . . . .	76
4.14	Signal energy as a function of pump energy of the crystal-2 SF-OPO with the $R = 85\%$ OC. . . . .	76
4.15	Spectra of the signal and sum-frequency beams of the crystal-2 SF-OPO with the $R = 85\%$ OC. . . . .	77
4.16	Energy conversion efficiency as a function of $\alpha$ of the double-pass crystal-3 SF-OPO. . . . .	79
4.17	Output energies as functions of pump energy of the double-pass and single-pass crystal-3 SF-OPOs. . . . .	80
4.18	Optimum polarization rotation angle and maximum energy conversion efficiency as functions of pump energy of the double-pass crystal-3 SF-OPO. . . . .	81
4.19	Time profiles of the pump and sum-frequency pulses of the double-pass and single-pass SF-OPOs. . . . .	82
4.20	Spectra of the sum-frequency beam for the double-pass and single-pass configurations. . . . .	82

4.21	Spatial profiles of the sum-frequency beam of the double-pass crystal-3 SF-OPO. . . . .	83
4.22	Signal wavelengths measured for various values of $\phi$ for the crystal-3 SF-OPO. . . . .	84
4.23	Calculated and measured energy conversion efficiency as a function of $\alpha$ for the double-pass configuration. . . . .	91
4.24	Calculated and measured output sum-frequency energy as a function of pump energy for the double-pass configuration. . . . .	91
4.25	Calculated and measured time profile of the sum-frequency pulse for the double-pass configuration. . . . .	92
5.1	Schematic arrangement of the travelling-wave IOPO. . . . .	97
5.2	Energy-level diagram of the four-level system. . . . .	101
5.3	Photon flux densities of the intracavity laser, signal, and idler as functions of the input photon flux density for varying $L_{oc}$ values. . . . .	108
5.4	Photon flux densities of the intracavity laser, signal, and idler as functions of the input photon flux density for varying $\eta_c$ values. . . . .	111
5.5	Contour plots for the maximum pump-to-signal photon conversion efficiency and the corresponding $L_{oc}$ for $\alpha_l = 0.01 \text{ cm}^{-1}$ . . . . .	113
5.6	Contour plots for the maximum pump-to-signal photon conversion efficiency and the corresponding $L_{oc}$ for $\alpha_l = 0.07 \text{ cm}^{-1}$ . . . . .	114
5.7	Contour plots for the maximum pump-to-idler photon conversion efficiency and the corresponding $L_{oc}$ for $\alpha_l = 0.01 \text{ cm}^{-1}$ . . . . .	116
5.8	Contour plots for the maximum pump-to-idler photon conversion efficiency and the corresponding $L_{oc}$ for $\alpha_l = 0.07 \text{ cm}^{-1}$ . . . . .	117

# List of Tables

2.1	Phase matching geometries for the SD-OPO. . . . .	28
2.2	Phase matching geometries for the SF-OPO. . . . .	29
3.1	Cut-angles of the crystals and corresponding signal wavelengths generated using these crystals. . . . .	39
3.2	Pulse-widths (FWHM) for various pump energies. . . . .	49
5.1	Parameters of the laser system based on a Ti:sapphire crystal. . .	106

# Chapter 1

## Introduction

Soon after the discovery of the laser [1], the first observation of coherent nonlinear optical effects was made by Franken *et al.* who demonstrated second-harmonic generation (SHG) of light in the crystal of quartz using the ruby laser [2]. The conversion efficiency of the device was less than one part per billion due to the lack of phase matching, however this discovery marks the beginning of an era of new optical devices which can convert the laser beams into regions of the spectrum where no laser sources are available.

The three-wave mixing processes, namely sum-frequency generation (SFG), SHG, and difference-frequency generation (DFG), are parametric interactions which are facilitated by the second-order nonlinearity of a material, usually a nonlinear crystal. In SFG, two input fields frequency-mix to produce a sum-frequency output. In SHG, which is a special case of SFG, the two input fields are at the same frequency, hence frequency-doubling is achieved. Similarly, in DFG, a difference-frequency output is generated. The DFG process also facilitates optical parametric amplification of a laser beam. The efficiencies of these interactions are strongly dependent on several factors such as phase-matching characteristics, effective second-order nonlinearity, length of the nonlinear crystal, temporal and spatial profiles, spectral content, and intensities of the input beams.

An optical parametric oscillator (OPO) is formed by placing an optical parametric amplifier (OPA) into an optical resonator or a cavity. A higher frequency input pump field is downconverted to signal and idler fields at the output of the device. An OPO can be either a singly resonant oscillator (SRO), where only the signal is resonated inside the cavity, or doubly-resonant oscillator (DRO), where both signal and idler fields are resonated. In an SRO, provided that the gain for the signal is higher than all cavity losses combined, the signal field builds up from parametric noise and is amplified by means of optical parametric amplification. The pump intensity which provides this required gain level for starting up the oscillation is known as the pump threshold. Since both signal and idler fields are resonated in DROs, they have much lower pump thresholds than SROs, however the stability and smooth tuning are compromised in these devices [3]. Consequently, their use remained rather restricted to continuous-wave (cw) OPOs, where available peak intensities of pump lasers are relatively low and reduction of the oscillation threshold is crucial. In addition to the factors mentioned for a three-wave mixing process, the efficiency of downconversion of the pump field into signal and idler fields in an OPO strongly depends on the cavity parameters, such as residual and output coupling losses experienced by the resonated field(s), physical structure of the cavity, and spatial characteristics of the cavity modes.

For efficient nonlinear interaction, the phase velocities of the interacting waves should be matched over the interaction length. The conventional method for achieving phase matching is to use the natural birefringence of the nonlinear crystal to compensate for dispersion [4, 5], which is known as birefringent phase matching (BPM). An alternative technique, first proposed by Armstrong *et al.* [6] in 1962 and known as quasi-phase matching (QPM), uses a periodic modulation of the sign of the nonlinear coefficient to periodically reset the optical phase. The phase-matching condition also facilitates the mechanism that makes the OPO a tunable device. For instance, in the case of BPM, changing the crystal temperature (temperature-tuning) or propagation direction (angle-tuning), alters the dispersion parameters of the material, hence the frequencies of the signal and idler waves of the OPO need to change so that the phase-matching condition is maintained.

The idea of parametric amplification and generation of tunable light was proposed and analyzed by Armstrong *et al.*, Kroll, Kingston, and Akhmanov *et al.* [6–9]. Wang *et al.* [10] have provided the first experimental demonstration of parametric gain in a three-wave mixing interaction. The first successful demonstration of an OPO was a nanosecond oscillator based on lithium niobate ( $\text{LiNbO}_3$ ) and pumped by a frequency-doubled,  $Q$ -switched  $\text{Nd:CaWO}_4$  laser at 529 nm [11]. This demonstration led to an intense research interest in parametric devices and an extensive search for new nonlinear materials and pump sources began. In 1968, Smith *et al.* achieved cw oscillation in the near infrared in  $\text{Ba}_2\text{NaNb}_5\text{O}_{15}$  [12] and the first cw visible parametric oscillator was demonstrated by Byer *et al.* [13]. This OPO based on  $\text{LiNbO}_3$  was pumped by an argon-ion laser at 514 nm. The initial rapid progress in the field of optical parametric devices later slowed down due to the lack of suitable nonlinear materials and absence of laser sources of high spatial and spectral coherence and sufficient intensities. In 1980's new nonlinear crystals such as  $\beta$ - $\text{BaB}_2\text{O}_4$  (BBO),  $\text{LiB}_3\text{O}_5$  (LBO), and  $\text{KTiOPO}_4$  (KTP) were invented. The relatively high damage thresholds and large nonlinear coefficients of these crystals reignited the research in this field.

Crystals that cannot be phase matched because of the lack of adequate birefringence to offset dispersion in a BPM scheme can be phase-matched using QPM. Due to difficulties in manufacturing, there is a delay of almost three decades between the first proposal of QPM in 1962 [6] and practical implementation of QPM devices. Although there were a few previous methods for creating the modulation of the nonlinear coefficient necessary for QPM, such as chemical diffusion and electron-beam poling, the most practical and reliable one for the production of a QPM device was proposed and demonstrated by Yamada *et al.* [14], which is known as the electric-field poling technique. Following this demonstration, quasi-phase-matched second-harmonic generation [15] and OPOs [16] in bulk periodically-poled  $\text{LiNbO}_3$  (PPLN) were demonstrated.

OPOs operating in the nanosecond pulsed regime have been the most extensively developed parametric devices due to the high-peak-pump powers (hundreds of megawatts) provided by the widely-used  $Q$ -switched lasers. As mentioned

above, the first OPO reported was a nanosecond OPO [11]. This device was a DRO, however SROs covering mainly infrared region of the spectrum based on materials such as  $\text{LiNbO}_3$  [17, 18],  $\text{LiIO}_3$  [19],  $\text{CdSe}$  [20],  $\text{Ag}_3\text{AsS}_3$  [21], and  $\text{AgGaS}_2$  [22] were subsequently demonstrated. The pump sources for these OPOs were mostly  $Q$ -switched neodymium (Nd) lasers and their harmonics.

In 1980's and 1990's, several nanosecond BBO OPOs were reported [23–27]. BBO OPOs were usually pumped with frequency-tripled Nd:YAG lasers at 355 nm; however pumping using the XeCl excimer laser at 308 nm was also demonstrated [28, 29]. These OPOs produced tunable outputs from 400 nm to 2.5  $\mu\text{m}$ . Several nanosecond LBO OPOs were also reported [30, 31]. LBO has an effective nonlinear coefficient ( $\sim 1$  pm/V) which is considerably lower than that of BBO ( $\sim 3$  pm/V), however its noncritical phase-matching (NCPM) capability and small walk-off angle allow the use of longer interaction lengths, thus comparable efficiencies to those obtained with BBO were achieved using this crystal.

KTP,  $\text{KTiOAsO}_4$  (KTA) and  $\text{KNbO}_3$  (KNB) are other nonlinear crystals which have been of particular interest for wavelength generation in the 3- to 5- $\mu\text{m}$  spectral range due to their longer infrared transmission beyond 4  $\mu\text{m}$ . These crystals have considerably larger effective nonlinear coefficients than LBO. In particular, KTP has been extensively used in nanosecond OPOs [32, 33]. KTA exhibits reduced idler idler absorption and a wider transparency range (up to 5.3  $\mu\text{m}$ ) than those of KNB and KTP. The first efficient nanosecond 1064-nm pumped KTA OPO with the capability of tuning in the 1.5- to 5- $\mu\text{m}$  range was reported by Bosenberg *et al.* [34] and the potential of this material for mid-infrared parametric generation was clearly demonstrated.  $\text{RbTiOAsO}_4$  (RTA) and  $\text{CsTiOAsO}_4$  (CTA) are other arsenate crystals which are useful for parametric generation in the 3- to 5- $\mu\text{m}$  spectral range.

Nanosecond OPOs based on QPM nonlinear materials such as PPLN [35, 36] and periodically poled KTP (PPKTP) [37, 38] were also reported. Large optical nonlinearities of QPM materials, their NCPM capabilities and long interaction lengths enables the realization of pulsed OPOs at considerably lower pump pulse

energies than are achievable with materials employing BPM. PPLN has a relatively low damage threshold but a quite large nonlinearity, hence it is especially suitable for use in nanosecond OPOs that are pumped by cw-diode-pumped  $Q$ -switched lasers with high repetition rates (larger than 1 kHz) which have high average power outputs (larger than 1 W) with relatively low pulse energies and peak powers. However, small apertures of the periodically-poled crystals (the material thickness is usually 0.5 to 1 mm for PPLN and 1 to 2 mm for PPKTP) and its arsenate analogs, such as PPKTA and PPRTA prevents the energy scaling of such devices. Recently, there have been efforts to produce large aperture QPM materials and a few nanosecond OPOs based on 3-mm-thick QPM materials, such as periodically poled MgO:LiNbO<sub>3</sub> [39], PPKTP [40], and PPRTA [41], were recently demonstrated.

Detailed background information on the advances in the field of optical parametric devices including nanosecond, femtosecond, picosecond, and cw OPOs, and applications can be found in the three feature issues of the *Journal of Optical Society of America B* [42–44]. Also, an extensive summary on this subject is available in Ref. [45].

In recent years, several theoretical investigations or experimental demonstrations of simultaneous phase matching of multiple nonlinear interactions within the same crystal have been reported [46–85]. Such simultaneous phase matching allows efficient wavelength conversion of lasers to wavelengths that cannot be reached with a single nonlinear process. For example, the combination of optical parametric oscillation with second-harmonic generation SHG [48–51, 58] or SFG [52, 53, 57, 59] in the same second-order nonlinear crystal facilitates efficient conversion to wavelengths shorter than those of the source laser. The same wavelength range could be reached by using a second crystal for SHG or SFG placed either internal or external to the OPO cavity, however the conversion efficiency of the two-step process is usually low and this second crystal increases the system complexity and cost.

Both BPM [46–49, 52, 53, 57] and QPM [54–56, 61–64] have been used for

simultaneous phase matching of two different processes within the same nonlinear crystal. When the BPM method is used, the coincidental crossing of the phase-matching curves facilitates the simultaneous phase matching for a set of wavelengths and polarization directions, a particular direction of propagation, and a particular temperature. In the case of simultaneous phase matching with QPM, the fundamental Fourier component of the grating momentum cancels the phase-mismatch term of one process, whereas one of the harmonics cancels the phase-mismatch term of the second process. This can only happen by coincidence, as well. Furthermore, in neither BPM nor QPM, the relative strengths of the two simultaneously phase-matched processes cannot be freely adjusted.

Recently, quasi-periodic or aperiodic grating structures have been proposed for use in simultaneous phase matching with QPM [50,51,65–85]. Of these, aperiodic grating structures provide the highest degree of flexibility for simultaneous phase matching of multiple interactions for any given set of wavelengths and furthermore enable the free-adjustment of the relative strength of the processes [50,51,80–84].

Laser sources in the red part of the spectrum have several important applications in areas such as display technologies, holography, biomedical systems, materials processing, and basic science. Broad-area InGaAlP diodes and diode arrays [86] have been extensively used as an alternative to rather inefficient krypton-ion lasers for red beam generation. Although the power available from red laser diodes has increased up to multiwatt levels and various types of beam shaping techniques are under investigation, their output power levels are still lower and beam shapes are poorer than those of the solid-state lasers employing laser crystals. Furthermore, red laser diodes exhibit a reduced lifetime with respect to laser diodes that are widely used for pumping solid-state lasers near 808 nm.

Efficient conversion of solid-state lasers based on Nd doped laser crystals to red wavelengths is an attractive approach to red generation, especially beyond power or energy levels that are attainable with semiconductor lasers.

Nd:YAG [87–89], Nd:YLF [90,91], Nd:YVO<sub>4</sub> [92,93] and Nd:GdVO<sub>4</sub> [94,95] lasers operating at around 1.3  $\mu\text{m}$  were converted into red wavelengths using

either extracavity or intracavity doubling schemes in the cw, nanosecond or picosecond pulsed regimes. In particular, a diode-end-pumped  $1.34\ \mu\text{m}$  Nd:GdVO<sub>4</sub> cw laser was intracavity-doubled using a lithium triborate (LBO) nonlinear crystal and as much as 2.4 W output at 670 nm in a nearly TEM<sub>00</sub> mode was obtained for an absorbed pump power of 9.2 W, yielding a conversion efficiency of 26% [94]. In another experiment, a diode-end-pumped  $Q$ -switched Nd:GdVO<sub>4</sub> laser with a repetition rate of 47 kHz was intracavity-doubled using an LBO crystal and a red output with an average power of 6 W at 671 nm, corresponding to an optical conversion efficiency of 12.8%, was obtained [95]. The highest average power for a red output reported to date is 11.5 W and was achieved by frequency-doubling a side-pumped Nd:YAG laser operating at  $1.32\ \mu\text{m}$  and at a repetition rate of 3.5 kHz using a 4-cm-long LBO crystal [89]. However, the optical conversion efficiency of this device was only 2.4%, which is mainly due to the side-pumping scheme employed, and the beam quality was poor since the  $M^2$  value was as high as 15.

Diode-pumped dual-wavelength Nd:YVO<sub>4</sub> (Nd:GdVO<sub>4</sub>) lasers oscillating at 1064 nm (1063 nm) and 1342 nm simultaneously were converted into multiple colors including red using quasi-periodically and aperiodically-poled LiTaO<sub>3</sub> crystals which are simultaneously phase-matched for multiple interactions [81–85]. In particular, simultaneous generation of efficient red, green, and blue (RGB) was achieved by doubling and tripling a diode-pumped  $Q$ -switched 1342 nm and 1063 nm Nd:GdVO<sub>4</sub> laser using an aperiodically poled LiTaO<sub>3</sub> crystal whose grating structure was designed using the method described in Ref. [51]. The crystal was placed external to the laser cavity. When the crystal was kept at a temperature of 115.8°C, the average outputs of the RGB light were 31.3, 18.4, and 3.7 mW, respectively. At the phase-matching temperature for the red beam (122.5°C), up to 252 mW average power was obtained for the red output with a 21% 1342-nm-to-671-nm conversion efficiency. In another experiment, simultaneous generation of efficient red and green was achieved by doubling a diode-pumped  $Q$ -switched 1342 nm and 1064 nm Nd:YVO<sub>4</sub> laser using an quasi-periodically poled LiTaO<sub>3</sub> crystal. At the phase-matching temperature for the red beam (118.5°C), up to

520 mW average power was obtained for the red output with a 30.5% 1342-nm-to-671-nm conversion efficiency.

Second, third, and fourth harmonic generation of Nd:YAG lasers operating at 1064 nm are commonly used to make green or UV sources. However, conversion to red wavelengths usually requires cascading harmonic generation with optical parametric generation. Generation of red laser beams using OPOs that are pumped by various harmonics of the Nd:YAG laser were reported in the nanosecond pulsed regime [23–27, 30, 31, 96]; however, the overall 1064-nm-to-visible energy conversion efficiencies of these systems are typically below 10%. As mentioned before, BBO and LBO are the two nonlinear crystals used in these devices. In particular, a BBO OPO pumped by a frequency-tripled  $Q$ -switched Nd:YAG laser with output at 355 nm generated signal wavelengths within the 412–710 nm range and up to 13% 355-nm-to-615-nm energy conversion efficiency was achieved [24]. Another BBO OPO pumped by a frequency-quadrupled  $Q$ -switched Nd:YAG laser with output at 266 nm provided tunable output from 330 nm to 1370 nm with different sets of mirrors [96]. An LBO OPO pumped by at a frequency-tripled  $Q$ -switched Nd:YAG laser generating pulses at 355 nm provided tunable signal output from 455 nm to 665 nm [30]. An efficient BBO OPO again pumped at 355 nm was capable of producing nanosecond red pulses with a 355-nm-to-615-nm energy conversion efficiency of 22%, however the overall 1064-nm-to-615-nm energy conversion efficiency was only 6.3% [27].

OPOs based on periodically poled crystals and pumped by frequency-doubled  $Q$ -switched Nd:YAG lasers generating nanosecond pulses at 532 nm were also employed for red beam generation. A nanosecond PPLN OPO pumped at 532 nm was reported to achieve a maximum of 12% conversion efficiency [36]; however, the output energy was limited due to the damage threshold of the lithium niobate crystal that is imposed by aperture limitations. Similarly, a recently reported nanosecond PPKTP OPO that is pumped at 532 nm [38] also suffers from output energy limitations imposed by the damage threshold, a general problem resulting from aperture-size constraints in crystal poling.

Only a single OPO pumped by the fundamental of an Nd:YAG laser operating

at 1064 nm for red beam radiation is reported in the literature. This OPO pumped by a cw Nd:YAG laser at 1064 nm was based on two PPLN grating regions in series, one for parametric generation and the other for SFG [97]. A red output power of 2.5 W and a 1064-nm-to-629-nm power conversion efficiency of 21% was achieved. However, there are some drawbacks hindering the practical use of this device. The 5.5-cm-long PPLN crystal had to be kept at a temperature as high as 195°C in a temperature-controlled oven for optimizing the red output. The elevated temperature also eliminates the photorefractive damage, an effect seen in LiNbO<sub>3</sub> crystals which reduces the conversion efficiency. Furthermore, sudden drops occurred in the device output after an operation period of 8-50 hours due to an unknown effect resulting in an index change in the crystal.

Red generation using KTA was previously achieved by sum-frequency mixing the 1535-nm output of an OPO pumped by the 355-nm third harmonic of a mode-locked Nd:YVO<sub>4</sub> oscillator-amplifier system with the residual 1064-nm laser radiation [98]. The total visible (red and blue) output generated by this rather complex system was 6.5 W for a 1064-nm input power of 28 W and the overall 1064-nm-to-629-nm power conversion efficiency was 8%.

Several other methods have been used for red generation. Continuous-wave laser emission at 635 nm was demonstrated in Pr<sup>+3</sup>/Yb<sup>+3</sup>-doped fibers employing upconversion processes [99, 100]. These upconversion fiber lasers were pumped with Ti:sapphire lasers operating at around 850 nm and a maximum of 1 W output power, corresponding to a 850-nm-to-635-nm power conversion efficiency of 19%, was achieved [99]. The output beams of synchronously seeded Yb and Er fiber amplifiers with 7.3 W and 9.4 W, respectively, average output powers and peak powers similar to 0.5 kW were frequency-mixed in a PPKTP crystal to produce a 1.4 W sum-frequency output at 630 nm [101]. Tunable femtosecond pulses were obtained in the 605–635 nm wavelength region by frequency-doubling the output of a regeneratively initiated self-mode-locked Cr:forsterite laser in a LiIO<sub>3</sub> nonlinear crystal and a 1230-nm-to-615-nm conversion efficiency of 10% was achieved [102]. Continuous-wave laser radiation at 693 nm from a LiNbO<sub>3</sub>:ZnO:Nd<sup>3+</sup> nonlinear laser crystal by self-frequency-doubling its fundamental laser line at 1386 nm. The pump source was a Ti:sapphire laser and 0.3%

of the total absorbed pump power of 800-mW was converted into red [103].

In this thesis, we demonstrate an alternative technique for highly efficient red beam generation. We have successfully implemented nanosecond sum-frequency generating OPOs (SF-OPOs) based on KTA that is simultaneously phase matched for optical parametric generation and SFG. Pumped at a wavelength of 1064 nm by a  $Q$ -switched Nd:YAG laser, these devices can produce red outputs at 627 nm with 1064-nm-627-nm energy conversion efficiencies reaching  $\sim 20\%$  for the single-pass pumping and  $\sim 30\%$  for the double-pass pumping. Our devices are simpler in architecture compared to other devices converting the nanosecond Nd:YAG laser radiation into red wavelengths. A typical nanosecond SF-OPO is comprised of three cavity mirrors which are all high reflectors at the signal wavelength (1525 nm), a 2-cm-long KTA crystal, and an intracavity retarder plate for rotating the polarization of the signal beam. The total cavity length is only 4.8 cm. With its small size, the device can be shaped into a module to be placed in front of the most widely-used lasers, Nd:YAG lasers, much like the harmonic generator modules that are used for converting the Nd:YAG laser radiation into 532 nm or 355 nm, and high energy red pulses at 627 nm can be generated with a quite high energy conversion efficiency. There is energy scalability in our devices, that is, the device can operate at larger pulse energies by simply increasing the beam size. Such scaling is not possible for OPOs based on periodically-poled crystals due to the limited aperture size of these devices. With these advantages, our double-pass SF-OPO provides the least costly but most efficient option for converting the nanosecond Nd:YAG laser radiation into a red wavelength. Furthermore, our single-pass SF-OPO is the first demonstration of simultaneous phase matching within an OPO operating in the nanosecond regime.

An intracavity optical parametric oscillator (IOPO) is formed by placing the OPO internal to a laser cavity. These devices have been extensively used for frequency conversion due to the high intracavity intensities that they provide for pumping the OPO, hence cw operation of such devices becomes feasible even for nonlinear crystals having moderate nonlinearities. We have developed a plane-wave model for modelling cw singly-resonant IOPOs. Due to differences between

the operation principles of these devices and the nanosecond OPOs presented as the main theme of this thesis, a separate chapter is devoted to the background information and our model for cw IOPOs.

The organization of the thesis is as follows: Chapter 2 is devoted to a theoretical background on optical parametric interactions. Chapter 3 is devoted to the experimental results of our nanosecond OPOs based on KTA. We used three different KTA crystals with different cut-angles in these experiments and the OPOs based on these crystals have been characterized in terms of their output energies, time profiles and spectra. Chapter 4 is devoted to the experimental results of our nanosecond upconversion OPOs based on KTA. The characterization of these devices is performed in terms of their energy output as functions of polarization rotation angle and input pump energy, time profiles, spatial beam profiles, and spectra of the output. Double-pass and single-pass pumping schemes are compared. In the last of this chapter previous models developed for the nanosecond OPOs are reviewed and the experimental results for the double-pass SF-OPO are compared with the calculations of a numerical model which was recently reported [104]. Chapter 5 is devoted to the explanation of the operation principles of cw IOPOs, our plane-wave model for these devices and results of this model. Finally, remarks and conclusions are provided in Chapter 6.

## Chapter 2

# Optical Parametric Interactions

In a nonlinear material, an intense electric field induces a nonlinear polarization with second-order and higher-order components. The second-order nonlinearity of the medium gives rise to the three-wave mixing processes which are SFG, SHG, and DFG. DFG also facilitates optical parametric amplification of a laser beam making the realization of OPOs possible.

In this chapter, we introduce the coupled-mode equations for the three-wave mixing processes in a lossless nonlinear crystal and give the plane-wave solutions of these equations for SFG, SHG, and optical parametric amplification. It should be noted that these plane-wave solutions usually predict larger conversion efficiencies compared to those achieved in reality. This is due to the fact that plane-waves do not account for the finite size of the beams and the diffraction. However, we will use the plane-wave solutions for explaining the general characteristics of these nonlinear processes.

Next, we describe the parameters that are important in the design of an OPO. Subsequently, we give the possible polarization geometries for simultaneous phase-matching of optical parametric generation and SHG or SFG processes within a single crystal and also present the coupled-mode equations for two examples of such simultaneous phase matching. The last part of the chapter is devoted to the explanation of how phase matching of a single nonlinear process and simultaneous

phase matching of two nonlinear processes in a nonlinear crystal are achieved using BPM and QPM.

## 2.1 Nonlinear Polarization

The polarization  $\mathbf{P}(\mathbf{r},t)$  induced in an anisotropic and dispersionless nonlinear material due to a total electric field  $\mathbf{E}(\mathbf{r},t)$  can be expressed as a power series given by [105]

$$\mathbf{P}(\mathbf{r},t) = \epsilon_0 \boldsymbol{\chi}^{(1)} \cdot \mathbf{E}(\mathbf{r},t) + \epsilon_0 \mathbf{E}(\mathbf{r},t) \cdot \boldsymbol{\chi}^{(2)} \cdot \mathbf{E}(\mathbf{r},t) \quad (2.1)$$

$$\begin{aligned} & + \epsilon_0 \mathbf{E}(\mathbf{r},t) \cdot [\mathbf{E}(\mathbf{r},t) \cdot \boldsymbol{\chi}^{(3)} \cdot \mathbf{E}(\mathbf{r},t)] + \dots \\ & = \mathbf{P}^{(1)}(\mathbf{r},t) + \mathbf{P}^{(2)}(\mathbf{r},t) + \mathbf{P}^{(3)}(\mathbf{r},t) + \dots \end{aligned} \quad (2.2)$$

where  $\epsilon_0$  is the permittivity of free space,  $\boldsymbol{\chi}^{(1)}$  is the linear susceptibility tensor of second rank,  $\boldsymbol{\chi}^{(2)}$  and  $\boldsymbol{\chi}^{(3)}$  are the nonlinear susceptibility tensors of third and fourth ranks, respectively.  $\mathbf{P}^{(1)}(\mathbf{r},t)$ ,  $\mathbf{P}^{(2)}(\mathbf{r},t)$ , and  $\mathbf{P}^{(3)}(\mathbf{r},t)$  are the linear, second-order, and third-order polarization vectors, respectively, with their expressions given on the right-hand side of Equation (2.1) separated with “+” signs. Equation (2.1) is still valid for an electric field that is composed of monochromatic waves in a medium with dispersion. In this case, the values of the tensors  $\boldsymbol{\chi}^{(1)}$ ,  $\boldsymbol{\chi}^{(2)}$ , and  $\boldsymbol{\chi}^{(3)}$  depend on the corresponding frequencies.

$\boldsymbol{\chi}^{(1)}$  is responsible for the linear optical properties of the medium such as refraction, dispersion, absorption, and birefringence.  $\boldsymbol{\chi}^{(2)}$  gives rise to nonlinear three-wave mixing processes such as SHG, SFG, DFG, and optical parametric generation.  $\boldsymbol{\chi}^{(3)}$  is responsible for four-wave mixing, optical bistability, phase conjugation, and the optical Kerr effect. With increasing rank of the nonlinearity, the magnitude of the susceptibility tensors decreases rapidly. For instance, the magnitude ratios of  $\boldsymbol{\chi}^{(1)}$ ,  $\boldsymbol{\chi}^{(2)}$ , and  $\boldsymbol{\chi}^{(3)}$  are similar to  $1 : 10^{-8} : 10^{-16}$  [45]. Hence, nonlinear effects in a medium are only observable when high-intensity lasers are employed. Some media such as gases, liquids, and amorphous solids have inversion symmetry and  $\boldsymbol{\chi}^{(2)}$  vanishes for such media, hence they cannot produce second-order nonlinear interactions.

## 2.2 Second-order Nonlinear Polarization

A second-order nonlinear process involves the parametric interaction of three optical fields at frequencies  $\omega_1$ ,  $\omega_2$ , and  $\omega_3$  such that

$$\omega_3 = \omega_1 + \omega_2. \quad (2.3)$$

For the process of optical parametric amplification, the fields at  $\omega_1$ ,  $\omega_2$ , and  $\omega_3$  are called the idler, the signal and the pump, respectively. For SFG, the lower frequency fields are referred to as the input fields and the field at  $\omega_3$  is the sum-frequency output.

The total electric field produced by these waves is given by

$$\mathbf{E}(\mathbf{r}, t) = \sum_i \text{Re} [\mathbf{E}_i(\mathbf{r})e^{j\omega_i t}] = \frac{1}{2} \sum_i [\mathbf{E}_i(\mathbf{r})e^{j\omega_i t} + \mathbf{E}_i^*(\mathbf{r})e^{-j\omega_i t}], \quad (2.4)$$

where  $\mathbf{E}_i(\mathbf{r})$  is the electric-field phasor at  $\omega_i$  and  $i = 1, 2, 3$ . Using a similar notation, the second-order nonlinear polarization with components each of which is induced at one of these frequencies can be expressed as

$$\mathbf{P}^{(2)}(\mathbf{r}, t) = \sum_i \text{Re} [\mathbf{P}_i^{(2)}(\mathbf{r})e^{j\omega_i t}], \quad (2.5)$$

where  $\mathbf{P}_i(\mathbf{r})$  is the polarization phasor at  $\omega_i$ .

For the interacting waves at  $\omega_1$  and  $\omega_2$ , using Equations (2.1)-(2.2) the corresponding second-order polarization phasor induced at  $\omega_3$  is given by

$$\begin{aligned} \mathbf{P}_3^{(2)}(\mathbf{r}) &= \frac{1}{2}\epsilon_0\mathbf{E}_2(\mathbf{r}) \cdot \boldsymbol{\chi}^{(2)}(\omega_1 + \omega_2, \omega_1, \omega_2) \cdot \mathbf{E}_1(\mathbf{r}) \\ &\quad + \frac{1}{2}\epsilon_0\mathbf{E}_1(\mathbf{r}) \cdot \boldsymbol{\chi}^{(2)}(\omega_1 + \omega_2, \omega_2, \omega_1) \cdot \mathbf{E}_2(\mathbf{r}). \end{aligned} \quad (2.6)$$

For a lossless medium, the full-permutation symmetry and Kleinman's symmetry are applicable [105], thus

$$\boldsymbol{\chi}^{(2)}(\omega_1 + \omega_2, \omega_1, \omega_2) = \boldsymbol{\chi}^{(2)}(\omega_1 + \omega_2, \omega_2, \omega_1). \quad (2.7)$$

which results in a polarization phasor at  $\omega_3$  with the following form

$$\mathbf{P}_3^{(2)}(\mathbf{r}) = \epsilon_0\mathbf{E}_2(\mathbf{r}) \cdot \boldsymbol{\chi}^{(2)}(\omega_1 + \omega_2, \omega_1, \omega_2) \cdot \mathbf{E}_1(\mathbf{r}). \quad (2.8)$$

Similarly, the polarization phasors at  $\omega_1$  and  $\omega_2$  are given by

$$\mathbf{P}_1^{(2)}(\mathbf{r}) = \epsilon_0 \mathbf{E}_2^*(\mathbf{r}) \cdot \boldsymbol{\chi}^{(2)}(\omega_3 - \omega_2, \omega_3, \omega_2) \cdot \mathbf{E}_3(\mathbf{r}) \quad (2.9)$$

and

$$\mathbf{P}_2^{(2)}(\mathbf{r}) = \epsilon_0 \mathbf{E}_1^*(\mathbf{r}) \cdot \boldsymbol{\chi}^{(2)}(\omega_3 - \omega_1, \omega_3, \omega_1) \cdot \mathbf{E}_3(\mathbf{r}), \quad (2.10)$$

respectively. Consequently, each polarization at a particular frequency is induced as a result of the nonlinear interaction of the electric fields at the other two frequencies with the frequencies satisfying the relationship given in Equation (2.3).

We also note that the  $\boldsymbol{\chi}^{(2)}$  tensor has 27 elements, however many of the components vanish under certain symmetry conditions and the number of independent components is generally far fewer. In the literature, another tensor  $\mathbf{d}$  with its elements given by

$$\mathbf{d}_{rpq} = \frac{1}{2} \boldsymbol{\chi}_{rpq}^{(2)}, \quad (2.11)$$

where the indices  $rpq$  refer to the cartesian axes  $x$ ,  $y$ , and  $z$ , is commonly used. When the Kleinman symmetry condition is valid, this tensor can be further reduced to a  $3 \times 6$  matrix, which has only 10 independent elements [105].

## 2.3 Coupled-Mode Equations

Maxwell's equations in a medium where no free currents and charges present are given as

$$\nabla \times \mathbf{E} = -\frac{\partial \mathbf{B}}{\partial t}, \quad (2.12)$$

$$\nabla \times \mathbf{H} = \frac{\partial \mathbf{D}}{\partial t}, \quad (2.13)$$

$$\nabla \cdot \mathbf{D} = 0, \quad (2.14)$$

$$\nabla \cdot \mathbf{B} = 0, \quad (2.15)$$

and the constitutive relations for a nonmagnetic medium are

$$\mathbf{D} = \epsilon_0 \mathbf{E} + \mathbf{P}, \quad (2.16)$$

$$\mathbf{B} = \mu_0 \mathbf{H}, \quad (2.17)$$

where  $\mu_0$  is the permeability of free space,  $\mathbf{H}$  is the magnetic field,  $\mathbf{D}$  and  $\mathbf{B}$  are the electric and the magnetic flux densities, respectively.

The sum of the expression for  $\mathbf{P}^{(1)}$  given in Equation (2.1) and  $\mathbf{P}^{(2)}$  are substituted for  $\mathbf{P}$  into Equation (2.16) while higher-order polarization terms are neglected and the electric flux density is now given as

$$\mathbf{D} = \epsilon_0 \boldsymbol{\epsilon}_{\mathbf{r}} \cdot \mathbf{E} + \mathbf{P}^{(2)} \quad (2.18)$$

where  $\boldsymbol{\epsilon}_{\mathbf{r}}$  is the relative permittivity tensor defined as

$$\boldsymbol{\epsilon}_{\mathbf{r}} = \mathbf{I} + \boldsymbol{\chi}^{(1)} \quad (2.19)$$

and  $\mathbf{I}$  is the  $3 \times 3$  identity matrix.

Taking the curl of Equation (2.12) and using Equations (2.13), (2.18), the driven-wave equation is obtained which is given as

$$\nabla \times \nabla \times \mathbf{E}(\mathbf{r}, t) + \frac{1}{c^2} \frac{\partial^2}{\partial t^2} \boldsymbol{\epsilon}_{\mathbf{r}} \cdot \mathbf{E}(\mathbf{r}, t) = -\mu_0 \frac{\partial^2}{\partial t^2} \mathbf{P}^{(2)}(\mathbf{r}, t), \quad (2.20)$$

where  $c = 1/\sqrt{\mu_0 \epsilon_0}$  is the speed of light.

For plane-waves propagating in the  $+z$  direction, the electric-field and second-order nonlinear polarization phasors which are defined as in Equations (2.4) and (2.5), respectively, can be written as

$$\mathbf{E}_i(z) = \hat{\mathbf{a}}_i A_i(z) e^{-jk_i z}, \quad (2.21)$$

$$\mathbf{P}_i^{(2)}(z) = \hat{\mathbf{a}}'_i B_i(z) e^{-jk'_i z}, \quad (2.22)$$

where  $i = 1, 2, 3$  and unit vectors  $\hat{\mathbf{a}}_i$  and  $\hat{\mathbf{a}}'_i$  represent the direction of polarization.  $A_i(z)$  and  $B_i(z)$  are the spatially slowly varying amplitudes of the electric field and nonlinear polarization, respectively,  $k_i$  and  $k'_i$  are the corresponding wavenumbers.

Using Equations (2.8), (2.9), and (2.10), the complex amplitudes  $A_i(z)$  and  $B_i(z)$  and the wavenumbers  $k_i$  and  $k'_i$  are related as follows

$$\hat{\mathbf{a}}'_1 B_1(z) = \epsilon_0 A_3(z) A_2^*(z) \hat{\mathbf{a}}_2 \cdot \boldsymbol{\chi}^{(2)}(\omega_1 = \omega_3 - \omega_2, \omega_3, \omega_2) \cdot \hat{\mathbf{a}}_3, \quad (2.23)$$

$$\hat{\mathbf{a}}'_2 B_2(z) = \epsilon_0 A_3(z) A_1^*(z) \hat{\mathbf{a}}_1 \cdot \boldsymbol{\chi}^{(2)}(\omega_2 = \omega_3 - \omega_1, \omega_3, \omega_1) \cdot \hat{\mathbf{a}}_3, \quad (2.24)$$

$$\hat{\mathbf{a}}'_3 B_3(z) = \epsilon_0 A_1(z) A_2(z) \hat{\mathbf{a}}_2 \cdot \boldsymbol{\chi}^{(2)}(\omega_3 = \omega_1 + \omega_2, \omega_1, \omega_2) \cdot \hat{\mathbf{a}}_1, \quad (2.25)$$

and

$$k'_1 = k_3 - k_2, \quad (2.26)$$

$$k'_2 = k_3 - k_1, \quad (2.27)$$

$$k'_3 = k_1 + k_2. \quad (2.28)$$

Using the definitions given in Equations (2.21) and (2.22), Equation (2.20) can be written in the frequency domain as

$$\nabla \times \nabla \times [A_i(z)e^{-jk_i z} \hat{\mathbf{a}}_i] - \frac{\omega_i^2}{c^2} A_i(z) e^{-jk_i z} \boldsymbol{\epsilon}_r(\omega_i) \cdot \hat{\mathbf{a}}_i = \mu_0 \omega_i^2 \hat{\mathbf{a}}'_i B_i(z) e^{-jk'_i z}. \quad (2.29)$$

Using the vector identity  $\nabla \times \nabla \times \mathbf{V} = \nabla(\nabla \cdot \mathbf{V}) - \nabla^2 \mathbf{V}$ , where  $\mathbf{V}$  is a vector, dot-multiplying Equation (2.29) with  $\hat{\mathbf{a}}_i$  and making use of the slowly-varying-amplitude approximation which is

$$\left| \frac{d^2 A_i}{dz^2} \right| \ll \left| k_i \frac{dA_i}{dz} \right|, \quad (2.30)$$

three coupled-mode equations governing the parametric interaction are obtained and they are given as

$$\frac{dA_1(z)}{dz} = -j \frac{\omega_1 d_{e1}}{cn_1} A_3(z) A_2^*(z) e^{-j\Delta k z}, \quad (2.31)$$

$$\frac{dA_2(z)}{dz} = -j \frac{\omega_2 d_{e2}}{cn_2} A_3(z) A_1^*(z) e^{-j\Delta k z}, \quad (2.32)$$

$$\frac{dA_3(z)}{dz} = -j \frac{\omega_3 d_{e3}}{cn_3} A_1(z) A_2(z) e^{j\Delta k z}, \quad (2.33)$$

where

$$\Delta k = k_3 - k_2 - k_1 \quad (2.34)$$

is the phase-mismatch term. Here,  $n_i$  represent the refractive indices and the constants  $d_{ei}$  are the effective second-order nonlinear coefficients which are given as

$$d_{e1} = \frac{1}{2} \hat{\mathbf{a}}_1 \cdot [\hat{\mathbf{a}}_2 \cdot \boldsymbol{\chi}^{(2)}(\omega_1 = \omega_3 - \omega_2) \cdot \hat{\mathbf{a}}_3], \quad (2.35)$$

$$d_{e2} = \frac{1}{2} \hat{\mathbf{a}}_2 \cdot [\hat{\mathbf{a}}_1 \cdot \boldsymbol{\chi}^{(2)}(\omega_2 = \omega_3 - \omega_1) \cdot \hat{\mathbf{a}}_3], \quad (2.36)$$

$$d_{e3} = \frac{1}{2} \hat{\mathbf{a}}_3 \cdot [\hat{\mathbf{a}}_2 \cdot \boldsymbol{\chi}^{(2)}(\omega_3 = \omega_1 + \omega_2) \cdot \hat{\mathbf{a}}_1]. \quad (2.37)$$

In a lossless medium all three effective nonlinear coefficients are equal and can be represented by a single effective coefficient

$$d_{\text{eff}} = d_{e1} = d_{e2} = d_{e3} \quad (2.38)$$

due to the full-permutation symmetry.

## 2.4 Sum-Frequency Generation

The solutions of the coupled-mode equations [Equations (2.31)–(2.33)] are given in terms of the well-known Jacobi elliptic functions [106]. The direction of energy flow in a given three-wave mixing process depends on the relative phase of the input fields. In particular, by using simple phasor diagrams for the complex field amplitudes of a phase-matched interaction ( $\Delta k = 0$ ), as done in Ref. [45], it can be shown that for optimum upconversion or SFG, the relative phase of the complex field amplitudes at the input of the nonlinear crystal defined by

$$\theta = \arg [A_3(z = 0)] - \arg [A_1(z = 0)] - \arg [A_2(z = 0)], \quad (2.39)$$

where “arg” denotes the argument or phase of a complex number, must be  $-90^\circ$ . Also, the required phase relation for optimum downconversion or DFG is  $\theta = 90^\circ$ . Furthermore, if the sum-frequency field is absent at the input of the crystal, then the fields will evolve through the crystal with the optimum phasing for upconversion since the initially absent sum-frequency field will be automatically generated with the correct phase. Similarly, the lack of either the idler (the field at  $\omega_1$ ) or signal (the field at  $\omega_2$ ) at the crystal input will automatically provide the optimum phasing for downconversion.

Equations (2.31)–(2.33) can be rewritten in a simpler form by performing the following substitutions for  $A_i$

$$A_1(z) = \sqrt{\frac{2\hbar\omega_1}{n_1 c \epsilon_0}} a_1(z), \quad (2.40)$$

$$A_2(z) = \sqrt{\frac{2\hbar\omega_2}{n_2 c \epsilon_0}} a_2(z), \quad (2.41)$$

$$A_3(z) = -j \sqrt{\frac{2\hbar\omega_3}{n_3 c \epsilon_0}} a_3(z), \quad (2.42)$$

where  $a_i$  are the normalized field amplitudes such that  $|a_i|^2 = \phi_i$  represent the photon flux densities at each frequency  $\omega_i$ . In this case, the coupled-mode equations become

$$\frac{da_1(z)}{dz} = -\kappa a_3(z)a_2^*(z)e^{-j\Delta kz}, \quad (2.43)$$

$$\frac{da_2(z)}{dz} = -\kappa a_3(z)a_1^*(z)e^{-j\Delta kz}, \quad (2.44)$$

$$\frac{da_3(z)}{dz} = \kappa a_1(z)a_2(z)e^{j\Delta kz}, \quad (2.45)$$

where the coupling constant is defined as

$$\kappa = d_{\text{eff}} \sqrt{\frac{2\hbar}{c^3 \epsilon_0}} \sqrt{\frac{\omega_1 \omega_2 \omega_3}{n_1 n_2 n_3}}. \quad (2.46)$$

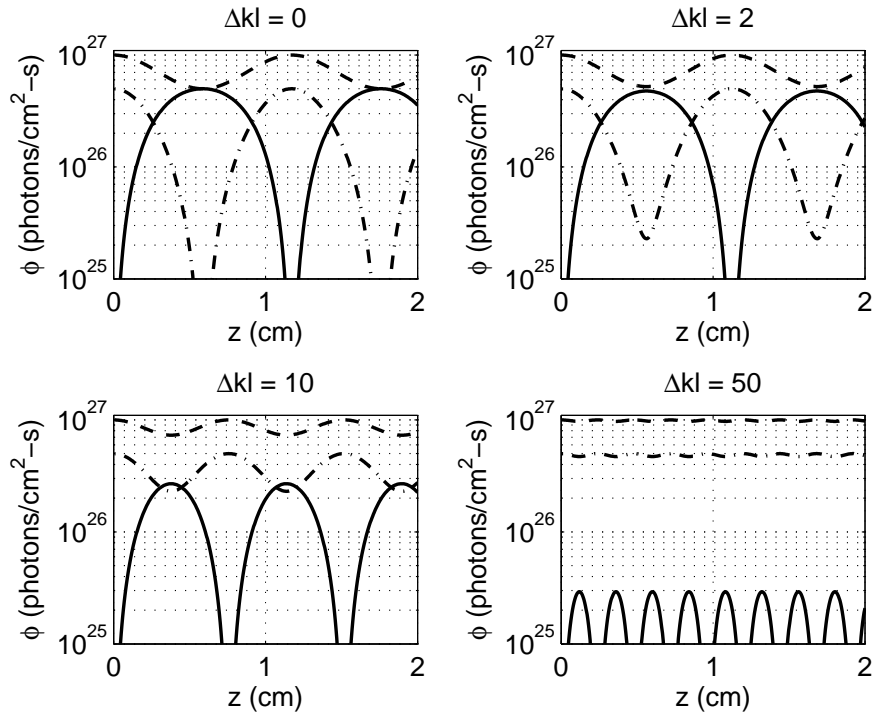


Figure 2.1: Photon flux densities  $\phi_1$  (dashed curves),  $\phi_2$  (dashed-dotted curves), and  $\phi_3$  (solid curves) as functions of  $z$  for  $\Delta kl = 0, 2, 10,$  and  $50$ .

Figure 2.1 shows the evolution of photon flux densities inside a 2-cm-long ( $l = 2$  cm) nonlinear crystal for  $\Delta kl = 0, 2, 10,$  and  $50$ , which are calculated using the Jacobi elliptic functions that are the solutions of Equations (2.43)–(2.45). A typical value of  $\kappa = 1 \times 10^{-13}$  (in  $\text{s}^{1/2}$ ) is used for these calculations.

The initial values of the photon flux densities are  $\phi_3(0) = 0$ ,  $\phi_2(0) = 5 \times 10^{26}$ , and  $\phi_1(0) = 1 \times 10^{27}$  photons/cm<sup>2</sup>-s.

The first subplot shown in Fig. 2.1 is for the phase-matched SFG ( $\Delta k = 0$ ). Since  $\phi_3(0) = 0$ , the sum-frequency field at  $\omega_3$  is generated with the correct phase that provides the optimum relative phase for SFG, hence  $\phi_3$  grows up to a maximum value of  $5 \times 10^{26}$  photons/cm<sup>2</sup>-s which occurs at  $z = 0.6$  cm. At this point,  $\phi_2$  is fully depleted, the field at  $\omega_2$  (or signal) is generated with the correct phase for DFG, and the photons in the sum-frequency field starts to be depleted by backconversion into the signal and idler fields. The backconversion ends at  $z = 1.2$  cm where  $\phi_3(0) = 0$  and SFG starts again. This cyclic behavior continues along the length of the crystal. It should be noted that two quantities,  $\phi_1(z) + \phi_3(z)$  and  $\phi_2(z) + \phi_3(z)$  are constant along the length of the crystal, which are known as Manley-Rowe conserved quantities [105].

In the subplots of Fig. 2.1 where  $\Delta k \neq 0$ , the initial relative phase  $\theta$  of the fields evolve continuously along the length of the crystal, rather than making jumps between  $-90^\circ$  and  $90^\circ$  at only discrete locations where the photon flux of a field goes to zero. As the strength of the phase-mismatch increases, the generation process reverses from SFG to DFG (or DFG to SFG) at shorter distances and hence the generation efficiency decreases. For instance, in the subplot with  $\Delta kl = 50$ ,  $\phi_3$  can only attain a maximum value of  $2.9 \times 10^{25}$  photons/cm<sup>2</sup>-s and  $\phi_1$  and  $\phi_2$  remain almost undepleted. Consequently, phase-matching is of prime importance for a nonlinear interaction to take place efficiently.

We also note that when the sum-frequency field is absent at the crystal input and the interaction is phase-matched ( $\Delta k = 0$ ), the relative phase relation for optimum SFG is readily satisfied when  $a_i$  are real numbers in the expressions for  $A_i$  [Equations (2.40–2.42)]. In this case,  $a_i^2$  represent the photon flux densities  $\phi_i$  and Equations (2.43)–(2.45) can be simplified in appearance by setting  $\Delta k = 0$  and replacing  $a_1^*(z)$  and  $a_2^*(z)$  with  $a_1(z)$  and  $a_2(z)$ , respectively.

## 2.5 Second-Harmonic Generation

In SHG, the fundamental fields are both at  $\omega_1 = \omega_2 = \omega$  and the second-harmonic field is at  $\omega_3 = 2\omega$ . If type-I phase-matching geometry is used, the fundamental fields are indistinguishable from each other since they are polarized along the same direction in addition to having identical frequencies. In type-II phase-matching geometry, the polarizations of the input fields are orthogonal to each other.

The coupled mode equations for the case of type-II phase matching are the same with an ordinary SFG process, which have been already given in the previous section. For the case of type-I phase matching, the coupled-equations are given as

$$\frac{da_1(z)}{dz} = -\kappa a_3(z)a_1(z), \quad (2.47)$$

$$\frac{da_3(z)}{dz} = \frac{1}{2}\kappa a_1^2(z), \quad (2.48)$$

where

$$\kappa = d_{\text{eff}} \sqrt{\frac{2\hbar}{c^3 \epsilon_0}} \sqrt{\frac{2\omega^3}{n_1^2 n_3}}, \quad (2.49)$$

In writing these equations, we assumed that there is perfect phase-matching ( $\Delta k = 0$ ) and the sum-frequency field is absent at the input, hence  $a_i$  are the real and normalized field amplitudes with  $A_1 = (2\hbar\omega/n_1 c \epsilon_0)^{1/2} a_1$  and  $A_3 = -j(4\hbar\omega/n_3 c \epsilon_0)^{1/2} a_3$  and  $a_i^2 = \phi_i$  represent the photon flux densities.

Figure 2.2 shows the evolution of the photon flux densities  $\phi_1$  and  $\phi_3$  as functions of the propagation distance  $z$  inside a 2-cm-long nonlinear crystal for type-I phase-matched SHG. For these calculations,  $\kappa = 1 \times 10^{-13}$  (in  $\text{s}^{1/2}$ ),  $\phi_3(0) = 0$ , and  $\phi_1(0) = 8 \times 10^{26}$  photons/cm<sup>2</sup>-s. In SHG, two input photons are annihilated for creating a single photon at the second-harmonic frequency and the second-harmonic photon flux density  $\phi_3$  asymptotically reaches a value of  $\phi_1(0)/2$ . Hence, at large distances, almost 100% photon conversion efficiency is possible. Furthermore, there is no backconversion of the second-harmonic field into the fundamental, which is a feature of type-I SHG.

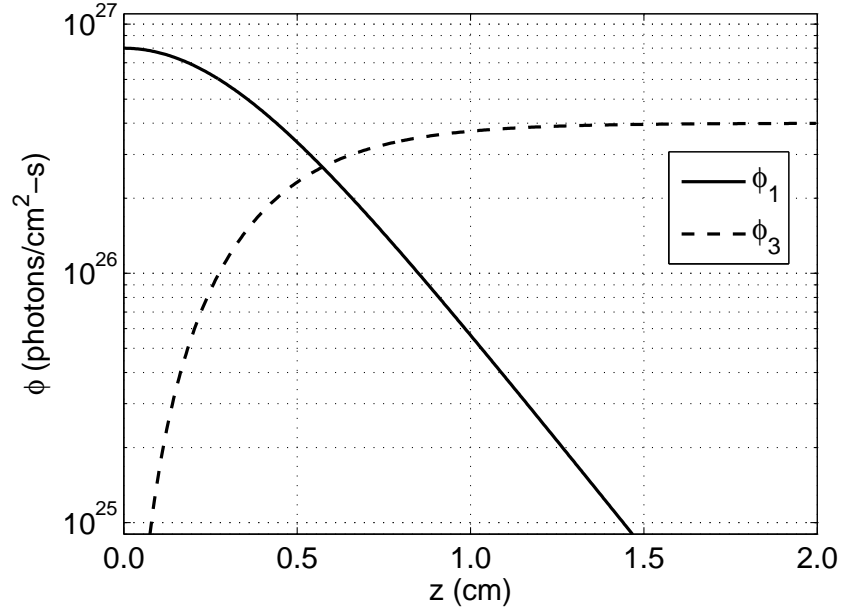


Figure 2.2: Evolution of the photon flux densities inside the nonlinear crystal as functions of the propagation distance for phase-matched SHG.

## 2.6 Optical Parametric Amplifier

In an OPA, a pump field at  $\omega_3$  and a signal field at  $\omega_2$  at the input interact in a nonlinear crystal to produce an idler field at  $\omega_1$ , and in this DFG process the signal field is also amplified with a gain which will be denoted by  $G$ . We first give the coupled-mode equations for the phase-matched OPA and assume that the idler field is absent at the crystal input which enables us to write the equations for real and normalized field amplitudes  $a_i$ . With these assumptions, Equations (2.31)–(2.33) can be rewritten in a simpler form by performing the following substitutions for  $A_i$

$$A_1(z) = -j\sqrt{\frac{2\hbar\omega_1}{n_1c\epsilon_0}}a_1(z), \quad (2.50)$$

$$A_2(z) = \sqrt{\frac{2\hbar\omega_2}{n_2c\epsilon_0}}a_2(z), \quad (2.51)$$

$$A_3(z) = \sqrt{\frac{2\hbar\omega_3}{n_3c\epsilon_0}}a_3(z), \quad (2.52)$$

where the required phase relation for optimum downconversion or DFG is included above, hence  $a_i$  are the real and normalized field amplitudes such that  $|a_i|^2 = \phi_i$  represent the photon flux densities at each frequency  $\omega_i$ . In this case, the coupled-mode equations become

$$\frac{da_1(z)}{dz} = \kappa a_3(z) a_2(z), \quad (2.53)$$

$$\frac{da_2(z)}{dz} = \kappa a_3(z) a_1(z), \quad (2.54)$$

$$\frac{da_3(z)}{dz} = -\kappa a_1(z) a_2(z), \quad (2.55)$$

where the coupling constant  $\kappa$  is defined as in Equation (2.46).

The solutions of Equations (2.53)–(2.55) are given in terms of Jacobi elliptic functions as [106, 107]

$$a_1(z) = \sqrt{C_1} \operatorname{cn}(Z_a | m_a), \quad (2.56)$$

$$a_2(z) = \sqrt{C_2} \operatorname{dn}(Z_a | m_a), \quad (2.57)$$

$$a_3(z) = \sqrt{C_1} \operatorname{sn}(Z_a | m_a), \quad (2.58)$$

where  $C_1$  and  $C_2$  are the Manley-Rowe [105] conserved quantities given as

$$C_1 = a_1^2(z) + a_3^2(z) = a_3^2(0), \quad (2.59)$$

$$C_2 = a_2^2(z) + a_3^2(z) = a_2^2(0) + a_3^2(0), \quad (2.60)$$

and

$$m_a = C_1/C_2, \quad (2.61)$$

$$Z_a = K(m_a) - \kappa_a \sqrt{C_2} z, \quad (2.62)$$

with

$$K(m) = \int_0^{\pi/2} (1 - m \sin^2 \theta)^{-1/2} d\theta, \quad (2.63)$$

which is the definition of the quarter-period of the Jacobi elliptic functions, given by the complete elliptic integral of the first kind [108].

The gain for the signal field is defined as

$$G = \frac{\phi_2(z=l)}{\phi_2(z=0)}, \quad (2.64)$$

where  $l$  is the length of the nonlinear crystal.

Figure 2.3 shows the evolution of the photon flux densities  $\phi_1$ ,  $\phi_2$  and  $\phi_3$  as functions of the propagation distance  $z$  inside a 2-cm-long ( $l = 2$  cm) nonlinear crystal for the phase-matched OPA. The results are calculated using Equations (2.56)–(2.58) with  $\kappa = 1 \times 10^{-13}$  (in  $\text{s}^{1/2}$ ),  $\phi_1(0) = 0$ ,  $\phi_2(0) = 8 \times 10^{24}$ , and  $\phi_3(0) = 8 \times 10^{25}$  photons/ $\text{cm}^2\text{-s}$ . The photon flux density of the signal ( $\phi_2$ ) is amplified with a corresponding gain of  $G = 6.9$ , whereas an idler field is generated with a photon flux density of  $4.7 \times 10^{25}$  photons/ $\text{cm}^2\text{-s}$  at  $z = 2$  cm.

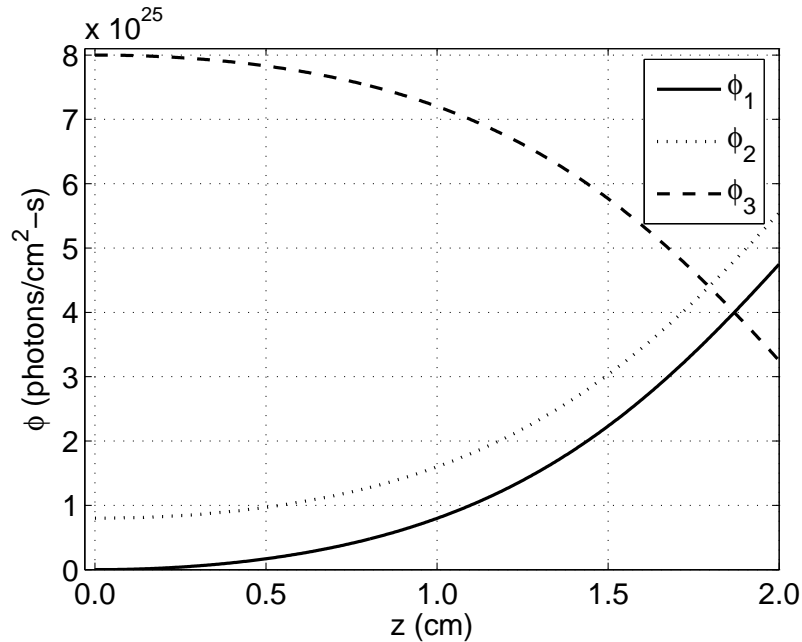


Figure 2.3: Evolution of the photon flux densities as functions of the propagation distance for the phase-matched OPA.  $\phi_1$ ,  $\phi_2$ , and  $\phi_3$  denote the photon flux densities of the idler, signal, and pump, respectively.

## 2.7 Optical Parametric Oscillator

A singly-resonant OPO is formed by placing the OPA inside an optical cavity that is resonant at the signal frequency. The signal field builds up from parametric noise if the unsaturated gain  $G_0$  is higher than all cavity losses combined, which

includes reflection, absorption, and scattering losses (residual losses) and the output coupling loss (useful loss) experienced by the intracavity signal field. In the steady state, an intracavity signal intensity assumes such a value that the saturated gain compensates for the losses exactly and the non-resonant idler leaves the cavity through the output mirror of the cavity that is highly transmitting at the idler frequency.

Denoting the reflectivity of the output coupling mirror of the cavity at the signal wavelength by  $R_{oc}$ , the useful loss is  $L_{oc} = 1 - R_{oc}$ . The intracavity signal photon flux density multiplied with the useful loss gives the signal photon flux density outside the cavity. Denoting the useless loss that the intracavity signal experiences by  $L_s$ , then the cavity reflectance can be written as

$$R_{cav} = R_{oc}(1 - L_s). \quad (2.65)$$

Hence, provided that unsaturated signal gain  $G_0$  is high enough to start up the oscillation, the signal gain saturates to value that will yield a round-trip gain of 1 which means that the steady-state intracavity signal flux density at the crystal input is a solution of

$$G[\phi_2(z = 0)] = \frac{1}{R_{cav}}. \quad (2.66)$$

Figure 2.4 shows the signal gain ( $G$ ) of an OPA as a function of the signal photon flux density at the input  $[\phi_2(0)]$  normalized to the input pump photon flux density  $[\phi_3(0)]$ . For this calculation, Equations (2.56)–(2.58) are employed and the values used for  $\kappa$  and  $\phi_3(0)$  are the same with those given in the example of the previous section. This OPA is placed into a cavity with  $L_s = 4\%$  and  $R_{oc} = 60\%$  which is resonant at the signal wavelength, resulting in an OPO. For very low photon flux densities of the signal provided by the noise,  $G_0 = 9.5$ , which is well above the  $1/R_{cav}$  level, hence the signal field grows in the cavity until the saturated gain is  $G = 1.7$  which compensates for the cavity losses exactly. At this steady-state point, the intracavity signal flux density is  $\phi_2(0) = 0.9\phi_3(0)$ .

An important parameter in the OPO design is the nonlinear drive which is given by

$$D = (\kappa l)^2 \phi_3(z = 0). \quad (2.67)$$

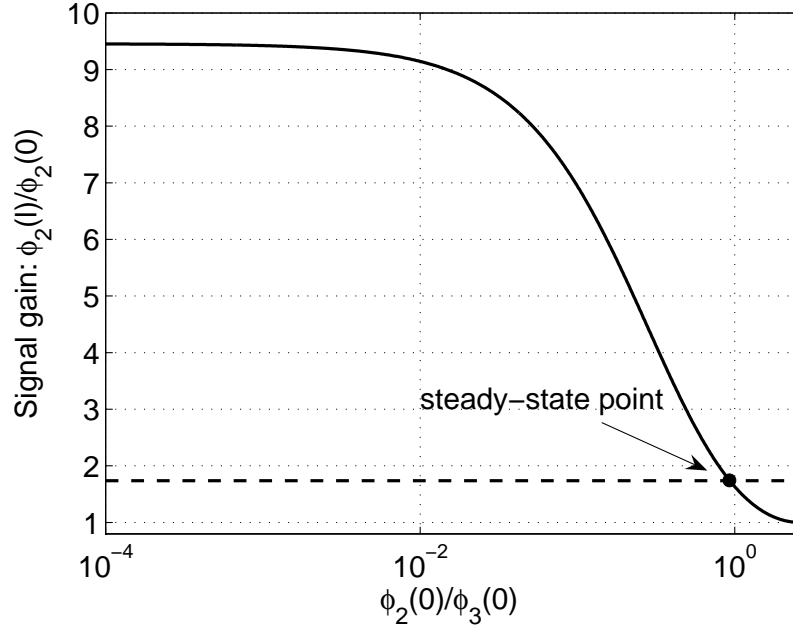


Figure 2.4: Signal gain ( $G$ ) as a function of the normalized signal photon flux density at the input.  $1/R_{\text{cav}}$  level is also indicated by a dashed line. The intersection point corresponds to the steady-state intracavity signal flux density at the crystal input and the saturated gain.

Equations (2.56)–(2.58) can be solved assuming that the pump remains undepleted in the interaction and it can be shown that the small-signal or unsaturated gain is given by

$$G_0 = \cosh^2(\sqrt{D}). \quad (2.68)$$

The threshold value of the input pump photon flux density can be found by solving  $G_0 R_{\text{cav}} = 1$  for  $D$ . The threshold photon flux density decreases with increasing  $\kappa$ ,  $l$  and decreasing cavity losses. When  $R_{\text{oc}} = 0$ , there is no output coupling and when  $R_{\text{oc}} = 100\%$ , the oscillation will never start, therefore there is an optimum output coupler reflectivity that yields the maximum signal output at a given pump power. However, the threshold will decrease and downconversion efficiency will increase simultaneously with a decrease in the useless cavity loss, increase in the crystal length and the  $d_{\text{eff}}$  value of the crystal, provided that the pump limit beyond which there will be backconversion into the pump field is not reached, which is unlikely for OPOs operating in the steady-state regime.

## 2.8 Simultaneously Phase-Matched Interactions

An OPO by itself can provide only downconversion of a pump field into the lower-frequency signal and idler fields. Upconversion is possible through the use of OPOs which are simultaneously phase-matched for SHG or SFG along with the parametric generation. These devices provide efficient conversion by using the high-intensity intracavity fields which are otherwise unavailable if a second crystal is placed external to the OPO cavity for upconversion. Several experimental demonstrations of devices which employ two crystals placed internal to the cavity, one for parametric interaction and the other for SHG or SFG, were also reported [109, 110]. However, this second crystal increases the system complexity and the conversion efficiencies provided by these devices are still lower than those of the single-crystal devices where parametric interaction and SHG or SFG occur simultaneously rather than being separated from each other.

Plane-wave theories for the self-doubling OPOs (SD-OPOs) and sum-frequency generating OPOs (SF-OPOs) using simultaneous phase matching were previously reported by Aytür *et al.* [58] and Dikmelik *et al.* [59]. In these devices, both parametric generation and SHG or both parametric generation and SFG can be phase matched for the same direction of propagation inside the nonlinear crystal. The cavities of these devices are singly-resonant at the signal wavelength and have only a few percent of residual losses for the signal. The output coupling is not linear as provided by an output mirror in the OPOs, but is through the generation of an upconverted field, hence the output coupling mechanism is non-linear. The cavity mirrors are also transparent to the generated second-harmonic or sum-frequency beams.

For SD-OPOs, six polarization geometries are possible depending on the types of OPO and SHG phase matching. Some of these geometries require an intracavity polarization rotation for the signal field while others do not. These polarization geometries can be further grouped under three different classes A, B, or C which are designated depending on the set of coupled-mode equations to be used for the plane-wave description of the SD-OPO. Table 2.1 lists these classes with the corresponding state of the rotation of the intracavity signal polarization and the

corresponding phase-matching polarization geometries of the OPO and SHG.<sup>1</sup>

Class	Rotation	OPO	SHG
A	no	type-I type-II	type-I
B	yes	type-II	type-I
C	yes	type-I type-II	type-II

Table 2.1: Phase matching geometries for the SD-OPO.

In particular, for a class-A SD-OPO, the polarization of the OPO signal is the same as that of the SHG fundamental. As a result, the signal field is common to the OPO and SHG processes, which become coupled to each other through the signal field. The set of coupled-mode equations describing this simultaneously phase-matched interaction is

$$\frac{da_1(z)}{dz} = \kappa_a a_3(z) a_2(z), \quad (2.69)$$

$$\frac{da_2(z)}{dz} = \kappa_a a_3(z) a_1(z) - \kappa_b a_6(z) a_2(z), \quad (2.70)$$

$$\frac{da_3(z)}{dz} = -\kappa_a a_1(z) a_2(z), \quad (2.71)$$

$$\frac{da_6(z)}{dz} = \frac{1}{2} \kappa_b a_2^2(z), \quad (2.72)$$

where  $a_i$  are the real and normalized field amplitudes such that  $a_i^2 = \phi_i$  represent the photon flux densities at each frequency  $\omega_i$ ,  $i = 1, 2, 3$ , and 6 are for the idler, the signal, the pump, and the second-harmonic fields, respectively, and  $\kappa_a$  and  $\kappa_b$  are the coupling constants for the parametric generation and SHG

---

<sup>1</sup>In this dissertation, we do not consider type-III as another type of phase matching. Instead, we label both type-II and type-III as type-II, which means that when only one of the lower frequency fields (the signal and idler for the OPO or the input fields for SHG or SFG), but not both, has a polarization that is orthogonal to that of the highest frequency field (the pump for the OPO and the second-harmonic and sum-frequency fields for the SHG and SFG, respectively) of the particular process, this is a type-II phase matching. If both of the lower frequency fields have polarizations orthogonal to that of the highest frequency field, this is a type-I phase matching. Also, as it will be explained in the next section, in BPM, the highest frequency fields in both processes (OPO and SHG or OPO and SFG) should be polarized along the fast axis of the crystal.

processes, respectively. For deriving these equations, Equations (2.53)–(2.55) for the parametric generation and Equations (2.47)–(2.48) for the type-I SHG are employed.

For SF-OPOs, nine polarization geometries are possible depending on the types of OPO and SFG phase matching. Some of these geometries require a polarization rotation for either the signal or the pump fields, or both. These polarization geometries can be further grouped under four different classes A, B, C, or D which are designated depending on the set of coupled-mode equations to be used for the plane-wave description of the SF-OPO. Table 2.2 lists these classes with the corresponding state of the rotation of the signal and pump polarizations and the corresponding phase-matching polarization geometries of the OPO and SFG.

Class	Rotation	OPO	SFG
A	none	type-I type-II	type-II
B	both	type-I type-II	type-II
C	pump	type-I type-II type-II	type-I type-I type-II
D	signal	type-II	type-II

Table 2.2: Phase matching geometries for the SF-OPO.

In particular, for a class-D SD-OPO, the signal is orthogonally polarized between the OPO and SFG processes, and an intracavity polarization rotation of the signal is necessary. The OPO and SFG processes are coupled to each other through the pump, which is common to both processes inside the crystal. The coupled-mode equations that describe the interaction are

$$\frac{da_1(z)}{dz} = \kappa_a a_3(z) a_2(z), \quad (2.73)$$

$$\frac{da_2(z)}{dz} = \kappa_a a_3(z) a_1(z), \quad (2.74)$$

$$\frac{da_3(z)}{dz} = -\kappa_a a_1(z)a_2(z) - \kappa_b a_6(z)a_4(z), \quad (2.75)$$

$$\frac{da_4(z)}{dz} = -\kappa_b a_6(z)a_3(z), \quad (2.76)$$

$$\frac{da_6(z)}{dz} = \kappa_b a_3(z)a_4(z), \quad (2.77)$$

where  $a_i$  are the real and normalized field amplitudes such that  $a_i^2 = \phi_i$  represent the photon flux densities at each frequency  $\omega_i$ ,  $i = 1, 2, 3, 4$ , and 6 are for the idler, the signal, the pump, the rotated signal, and the sum-frequency fields, respectively, and  $\kappa_a$  and  $\kappa_b$  are the coupling constants for the parametric generation and SFG processes, respectively. These equations can easily be derived using Equations (2.53)–(2.55) for the parametric generation and Equations (2.43)–(2.45) (with  $\Delta k = 0$  and for real and normalized field amplitudes) for the SFG.

Equations (2.69)–(2.72) and (2.73)–(2.77) can be solved using numerical techniques. The solutions of the coupled-mode equations corresponding to different classes of the SD-OPO and SF-OPO are given in detail in Refs. [58] and [59]. Two important parameters which determine the plane-wave dynamics of these devices are the nonlinear drive of the OPO that is defined as

$$D = (\kappa_a l)^2 \phi_3(z=0) \quad (2.78)$$

and the coupling strength of the two processes which is given by

$$\beta = \frac{\kappa_b}{\kappa_a}. \quad (2.79)$$

For instance, in class-D SF-OPOs, an intracavity retarder plate provides the required polarization rotation for the signal field. The photon conversion efficiency, which is the ratio of the twice the output sum-frequency photon density to the total input pump photon flux density,  $\eta = 2\phi_6(l)/\phi_3(0)$  (the coefficient 2 is due to the fact that two pump photons are needed to generate one sum-frequency photon), is maximized at an optimum polarization rotation angle depending on the values of  $D$ ,  $\beta$  and residual cavity loss for the signal. For a fixed  $D$ , as  $\beta$  increases, the maximum  $\eta$  increases up to unity (100%) and the value of the optimum polarization rotation angle decreases. At relatively high values of the nonlinear drive, it is possible to observe period doubling and chaotic behavior.

## 2.9 Phase Matching

For efficient nonlinear interaction, the interacting waves should be phase-matched over the interaction length, hence the condition of  $\Delta k = 0$  should be satisfied. Using Equation (2.34), the open form of this condition for beams propagating in the same direction or collinear beams is given as

$$n_3(\omega_3)\omega_3 - n_2(\omega_2)\omega_2 - n_1(\omega_1)\omega_1 = 0. \quad (2.80)$$

where  $n_i$  are the refractive indices at  $\omega_i$ . The energy conservation condition is restated here as

$$\omega_3 - \omega_2 - \omega_1 = 0. \quad (2.81)$$

The refractive index of materials that are lossless in the frequency range of interest shows an effect known as normal dispersion, that is, the refractive index is an increasing function of frequency. It is easy to see that Equations (2.80) and (2.81) cannot be simultaneously satisfied in an isotropic material that exhibits normal dispersion. However, there are two methods by which phase-matching condition is satisfied for a parametric interaction, which are BPM and QPM. In this section, we explain these methods and further give explanations of how simultaneous phase matching of two different processes is achieved by BPM and QPM.

### 2.9.1 Birefringent Phase Matching

The conventional method for achieving phase matching is to use the natural birefringence of the nonlinear crystal to compensate for dispersion. In a birefringent crystal, there are two normal modes of propagation and two different refractive indices associated with these modes. Phase-matching condition can be satisfied through the selection of the polarization of the fields involved in the nonlinear process from the polarization directions of these modes.

We consider the most general class of birefringent crystals, biaxial crystals.

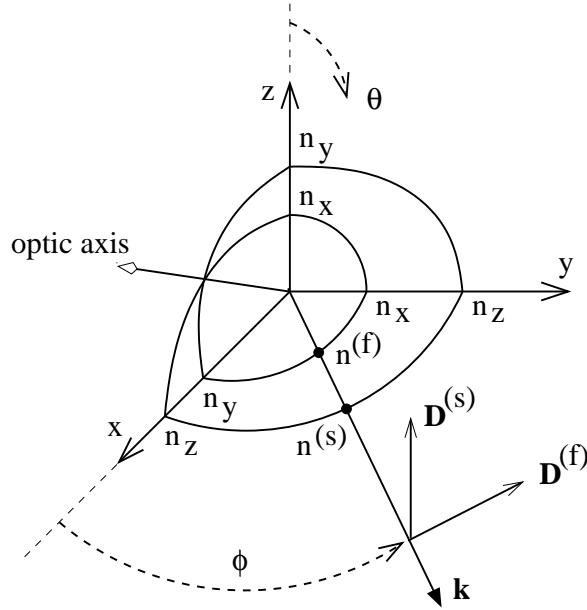


Figure 2.5: Dependence of the refractive index on light propagation direction and the directions of the electric flux density vectors of the two normal modes.

The dependence of the refractive index on light propagation results in a bilayer surface with four points of interlayer contact through which two optic axes pass [111, 112]. Such a surface is shown in Fig. 2.5 with the conventions that  $n_x < n_y < n_z$ , where  $n_x$ ,  $n_y$ , and  $n_z$  are the principle refractive indices at a particular frequency and temperature, angle  $\theta$  is measured from the  $z$  axis, and  $\phi$  is measured from the  $x$ - $z$  plane toward the  $y$ - $z$  plane. The propagation vector  $\mathbf{k}$  cuts this bilayer structure at two points yielding two refractive indices,  $n^{(f)}$  and  $n^{(s)}$ , corresponding to two normal modes. Here  $f$  and  $s$  stand for the *fast* and *slow* modes, respectively and  $n^{(f)} < n^{(s)}$ . Each normal mode has an electric flux density vector which is orthogonal to the same vector of the other mode and  $\mathbf{k}$ . After these electric flux density vectors denoted by  $\mathbf{D}^{(f)}$  and  $\mathbf{D}^{(s)}$  are determined, the corresponding directions of the electric fields, hence the polarization directions of the normal modes, can be found [112].

Assuming that the temperature is fixed,  $n_i^{(f)}$  and  $n_i^{(s)}$  at a frequency  $\omega_i$  are the roots of the following equation for  $n_i$  [112, 113]

$$\frac{\sin^2 \theta \cos^2 \phi}{n_i^{-2} - n_{x_i}^{-2}} + \frac{\sin^2 \theta \sin^2 \phi}{n_i^{-2} - n_{y_i}^{-2}} + \frac{\cos^2 \theta}{n_i^{-2} - n_{z_i}^{-2}} = 0 \quad (2.82)$$

where  $n_{x_i}$ ,  $n_{y_i}$ , and  $n_{z_i}$  are the principle refractive indices at  $\omega_i$ . The expressions for  $n_{x_i}$ ,  $n_{y_i}$ , and  $n_{z_i}$  in terms of frequency  $\omega_i$  (and temperature) are given by the Sellmeier equations [111].

With the assumption that all beams involved in the nonlinear process are collinear, hence the directions of  $\mathbf{k}_i$  are the same (a detailed discussion on non-collinear phase matching can be found elsewhere [114]), three types of phase-matching geometries are possible that are governed by three equations each of which satisfies the phase-matching condition ( $\Delta k = 0$ ) and these equations are given as

$$n_3^{(f)}\omega_3 - n_2^{(s)}\omega_2 - n_1^{(s)}\omega_1 = 0, \quad (2.83)$$

$$n_3^{(f)}\omega_3 - n_2^{(s)}\omega_2 - n_1^{(f)}\omega_1 = 0, \quad (2.84)$$

$$n_3^{(f)}\omega_3 - n_2^{(f)}\omega_2 - n_1^{(s)}\omega_1 = 0. \quad (2.85)$$

Equations (2.83), (2.84), and (2.85) are the phase-matching conditions for the type-I, type-IIa, and type-IIb polarization geometries, respectively. These phase-matching geometries are shown in Fig. 2.6. The highest frequency field at  $\omega_3$  is always polarized along the fast axis of the crystal. When both of the lower frequency fields at  $\omega_1$  and  $\omega_2$  are polarized along the slow axis of the crystal, this polarization geometry is referred to as type-I phase matching. In type-II phase matching, either one of the lower frequency fields is polarized along the fast axis of the crystal, hence there are two possibilities, type-IIa and type-IIb. In the literature, both type-IIa and type-IIb are usually classified as only type-II, however type-IIb is sometimes referred to as type-III [59].

When the frequency of one of the fields involved in a three-wave mixing interaction and the propagation direction of the beams is given for a particular crystal, phase-matching curves provide the frequencies (or wavelengths) of the other two fields. For instance, for the process of optical parametric amplification, if the pump frequency  $\omega_3$  is given and the phase-matching geometry is set to be either type-I, type-IIa or type-IIb, the corresponding signal and idler frequencies can be exactly obtained by numerical calculations provided that this process is phase-matchable in the particular crystal. For a given direction of the propagation in

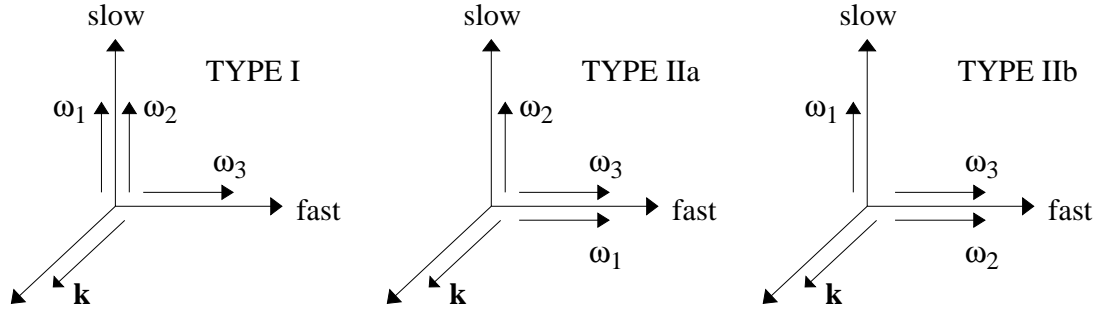


Figure 2.6: Phase-matching geometries for the three-wave mixing process with  $\omega_3 = \omega_1 + \omega_2$ .

the crystal, the angles  $\theta$  and  $\phi$  are known. First the roots of Equation (2.82) at the pump frequency, and at the trial values of the signal and idler frequencies, satisfying  $\omega_3 = \omega_1 + \omega_2$ , are found. These roots and one of the expressions given in Equations (2.83), (2.84), and (2.85) are chosen depending on the given phase-matching geometry and the expression evaluated to see if the phase-matching condition is satisfied. If the phase-matching condition is not satisfied, two new trial values for the signal and idler frequencies are chosen and the procedure is repeated until the phase-matching condition is satisfied. When the frequencies of the interacting waves are known, a similar procedure is applied for finding the corresponding phase-matching angle. Approximate expressions for determining the phase-matching angles for the collinear propagation of interacting waves in the principle planes ( $x$ - $y$ ,  $x$ - $z$ , and  $y$ - $z$  planes) of a biaxial crystal are also given in Ref. [111].

## 2.9.2 Quasi-Phase Matching

An alternative technique for phase matching is QPM that uses a periodic modulation of the sign of the nonlinear coefficient to periodically reset the optical phase.

In QPM, electric-field poling of the crystal in lithographically selected regions creates domain inversions, resulting in a modulation of the sign of the nonlinear

coefficient in the direction of propagation [14, 16]. The resulting nonlinear coefficient  $d(z) = g(z)d_{\text{eff}}$  is a function of distance  $z$  in the propagation direction, where  $g(z)$  is the grating modulation function that can only take values of  $+1$  or  $-1$ . A periodic grating function with period  $\Lambda$  can be expressed as a Fourier series

$$g(z) = \sum_{p=-\infty}^{\infty} G_p e^{jk_p z}, \quad (2.86)$$

where  $G_p$  are the Fourier coefficients,  $k_p$  are the magnitude of the grating vector of the  $p$ th Fourier component and

$$k_p = \frac{2\pi p}{\Lambda}. \quad (2.87)$$

The natural phase mismatch of the material  $\Delta k$  is cancelled by one of the Fourier components of the grating function [see Equations (2.31)–(2.33) with  $d_{\text{eff}} = d_{e1} = d_{e2} = d_{e3}$ ] through the adjustment of  $\Lambda$ , hence

$$\Delta k = k_p \quad (2.88)$$

for the  $p$ th order QPM. The modified effective nonlinear coefficient of the interaction is  $d_e = |G_p|d_{\text{eff}}$ . The maximum value for  $G_p$  (and  $d_e$ ) is obtained when first-order QPM is used with  $p = 1$  and duty cycle of the grating is set to be 50%, yielding  $|G_1| = 2/\pi$  with an accompanying reduction in the effective value of the nonlinear coefficient. Despite this reduction, in QPM, it is possible to use a polarization geometry which will result in the highest effective nonlinear coefficient possible. For instance, for lithium niobate the largest element of the nonlinear coefficient tensor is a diagonal element  $\mathbf{d}_{33}$  which is available if all waves are polarized along the  $z$  axis of the crystal. For such a polarization geometry, although QPM can easily be employed, it is not possible to obtain a phase-matched interaction using BPM. A detailed discussion on QPM can be found in Ref. [115].

### 2.9.3 Simultaneous Phase Matching with BPM

When two separate processes, processes  $a$  and  $b$ , are simultaneously phase-matched, the phase-mismatch terms of both processes,

$$\Delta k_a = k_3 - k_1 - k_2, \quad (2.89)$$

$$\Delta k_b = k_6 - k_4 - k_5, \quad (2.90)$$

have to vanish for the same direction of propagation and for the same temperature within the crystal. Here, we note that  $\omega_3 = \omega_1 + \omega_2$  for process *a* and  $\omega_6 = \omega_4 + \omega_5$  for process *b*.

In Section 2.8, we already summarized the phase matching geometries that are possible using BPM for the SD-OPOs and SF-OPOs. In Section 2.9.1 we also summarized the determination of the phase-matching curves in BPM. There is usually at least one common frequency between the simultaneously phase-matched processes. The simultaneous phase-matching angle is calculated using the intersection of the phase-matching curves corresponding to the wave that possess this common frequency.

For instance, in a class-D SF-OPO both the pump and signal frequencies are common. For this device, both OPO and SFG processes are phase-matched using a type-II (or type-IIb as introduced in Section 2.9.1) polarization geometry. For the parametric generation process, the pump and signal fields are polarized along the fast axis of the crystal, whereas the idler is polarized along the slow axis. For the SFG process, the pump and sum-frequency fields are polarized along the fast axis of the crystal, whereas the rotated signal is polarized along the slow axis. The polarization diagram of this simultaneous interaction is given in Fig. 2.7.

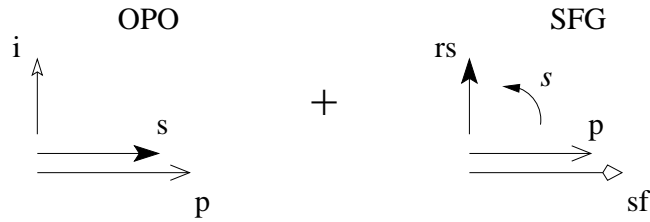


Figure 2.7: Polarization diagram for our SF-OPO. The fast axis is horizontal and the slow axis is vertical. Polarizations for the pump (p), signal (s), idler (i), polarization rotated signal (rs), and sum-frequency (sf) fields are shown. Intracavity polarization rotation of the signal field is indicated with an arc.

For a given pump frequency, the signal wavelengths of the parametric generation process as a function of a range of  $\theta$  and  $\phi$  values can be calculated, yielding the phase-matching curve for the signal. Next, for the same pump frequency

(taking into account the fact that the pump is a lower frequency field for this interaction), the rotated signal wavelengths of the SFG process as the function of the same range of  $\theta$  and  $\phi$  values are calculated. The intersection of these two curves occurs at the simultaneous phase-matching angle, from which all unknown wavelengths can be calculated. Such a calculation is shown in Fig. 4.11 of Section 4.3.6 for finding the simultaneous phase matching angle of a 1064-nm-pumped SF-OPO.

It should be noted that simultaneous phase matching using BPM is the result of the coincidental crossing of the phase-matching curves of the two processes. Hence, for common crystals, there is a limited number of processes and wavelengths that provide simultaneous phase matching.

#### 2.9.4 Simultaneous Phase Matching with QPM

Simultaneous phase matching in periodically poled crystals is only possible if the phase-mismatch term  $\Delta k_b$  given in Equation (2.90) happens to coincide with one of the nonzero harmonics of the grating modulation function given in Equation (2.86) or when both

$$\Delta k_a = \frac{2\pi p}{\Lambda} \quad (2.91)$$

$$\Delta k_b = \frac{2\pi q}{\Lambda} \quad (2.92)$$

are satisfied for some particular set of  $\Lambda$ , and integers  $p$  and  $q$ . Such circumstances can occur by coincidence, however it is not possible to achieve simultaneous phase matching with periodic gratings for arbitrary phase-mismatch terms  $\Delta k_a$  and  $\Delta k_b$ . Even if simultaneous phase matching is achieved for a set of  $\Lambda$ ,  $p$ , and  $q$ , the interaction will be weak unless  $p = 1$  or  $q = 1$ . Furthermore, the value of the coupling strength of the two processes  $\beta (= \kappa_b/\kappa_a)$  [Equation (2.79)] which is proportional to the ratio of the effective nonlinear coefficients (including the corresponding reductions due to the Fourier coefficients) cannot be adjusted freely.

An aperiodic grating design which enables simultaneous phase matching of two

processes with a pair of arbitrary  $\Delta k_a$  and  $\Delta k_b$  values, as well as, facilitates the adjustment of the coupling strength of these processes was recently proposed and successful operation of a SD-OPO based on an aperiodically-poled lithium niobate crystal whose grating structure was designed with this method was demonstrated [50, 51]. Briefly, the grating design is based on a continuous-valued function

$$f(z) = \cos(\Delta k_a z) + A \cos(\Delta k_b z) \quad (2.93)$$

where  $\Delta k_a$  and  $\Delta k_b$  are the phase-mismatch terms of the two processes to be simultaneously phase-matched and the parameter  $A$  facilitates the adjustment of the relative strength of the two processes to a desired value. Details of this design can be found in Ref. [51].

## Chapter 3

# Nanosecond Optical Parametric Oscillator Experiments

In this chapter, we present our nanosecond optical parametric oscillator experiments. Three different KTA crystals are used in these experiments. These are labelled as crystal-1, crystal-2, and crystal-3 throughout the text. The cut-angles of these crystals and corresponding signal wavelengths generated by the OPOs based on them when pumped by a  $Q$ -switched 1064-nm Nd:YAG laser at  $0^\circ$  incidence to the crystal surface under collinear phase matching conditions are given in Table 3.1. All crystals are  $5 \times 5 \times 20$  mm in size and their surfaces are anti-reflection coated for the pump and signal wavelengths. Crystal-1 was provided by Crystal Associates Inc., U.S., whereas crystal-2 and crystal-3 were purchased from Cristal Laser, France.

Crystal	1	2	3
Cut-angle	$\theta = 90^\circ, \phi = 24^\circ$	$\theta = 90^\circ, \phi = 33^\circ$	$\theta = 90^\circ, \phi = 32.6^\circ$
Wavelength	1530 nm	1523 nm	1524 nm

Table 3.1: Cut-angles of the crystals and corresponding signal wavelengths generated using these crystals.

We first present the nonlinear properties and phase matching characteristics of

the KTA crystal for the wavelengths of interest. Subsequently, we present the experimental configuration for the 1064-nm-pumped nanosecond optical parametric oscillators based on these crystals and the results of the characterization of these devices in terms of their energy outputs, input-output time profiles, and spectra.

### 3.1 Potassium Titanly Arsenate (KTA) Crystal

The first demonstration of the growth of single crystal potassium titanly arsenate (KTA) was reported by Bierlein *et al.* [116] and the first efficient nanosecond 1064-nm pumped KTA OPO was demonstrated by Bosenberg *et al.* [34]. KTA is a  $mm2$  point group positive biaxial crystal [111] and has phase-matching characteristics similar to those of its widely-used isomorph KTP, but a wider transparency range (0.35–5.3  $\mu\text{m}$ ) [117]. Due to its greatly reduced idler absorption, this crystal proved to be useful in OPOs providing high output powers and generating wavelengths in the mid-infrared range of the spectrum [118–121]. High damage threshold, large nonlinearity and broad acceptance bandwidths (angular and temperature) are other features of KTA which make it attractive in various wavelength conversion applications.

The nonlinear tensor elements of KTA reported in the literature show large variations [122–127]. The most recently reported nonlinear tensor of KTA is given in units of pm/V as [127]

$$\mathbf{d} = \begin{bmatrix} 0 & 0 & 0 & 0 & 2.3 & 0 \\ 0 & 0 & 0 & 3.64 & 0 & 0 \\ 2.3 & 3.66 & 15.5 & 0 & 0 & 0 \end{bmatrix} \quad (3.1)$$

in a coordinate system where  $x$ ,  $y$  and  $z$  refer to the principal axes with refractive-index ordering  $n_x < n_y < n_z$ .<sup>1</sup> The values of the elements of the tensor  $\mathbf{d}$  given above are for frequency-doubling of 1064-nm light in KTA, and the nonlinear coefficients for a particular nonlinear interaction at a given set of wavelengths are approximately determined using Miller's scaling [128]. For the experiments in this

---

<sup>1</sup>In this thesis, we use the same axis convention. Also, angle  $\theta$  is measured from the  $z$  axis, and  $\phi$  is measured from the  $x$ - $z$  plane toward the  $y$ - $z$  plane.

thesis, the propagation direction of the interacting waves is in the  $x$ - $y$  plane of the crystal ( $\theta = 90^\circ$ ) and hence the effective nonlinear coefficient is given as [111]

$$d_{\text{eff}} = \mathbf{d}_{31} \sin^2 \phi + \mathbf{d}_{32} \cos^2 \phi. \quad (3.2)$$

Similar to the case for the nonlinear tensor, there are several sets of quite different Sellmeier coefficients reported for KTA in the literature [122, 123, 129–131]. As a result of our experiments described in this chapter on KTA OPOs and the next chapter on KTA SF-OPOs, we have found that at a propagation direction of  $\theta = 90^\circ$  and some angle  $\phi$  within  $29 \pm 5^\circ$ , the Sellmeier coefficients given in Ref. [129] are the most accurate for calculating the wavelengths of type-II parametric generation of a  $p$ -polarized (horizontal, fast axis) signal beam at a wavelength within  $1523 \text{ nm} \leq \lambda_s \leq 1528 \text{ nm}$  from a  $p$ -polarized pump beam at 1064 nm, whereas the Sellmeier coefficients given in Ref. [131] are the most accurate for calculating the wavelengths of type-II sum-frequency mixing of a  $p$ -polarized pump beam at 1064 nm with an  $s$ -polarized (vertical, slow axis) beam at a wavelength within  $1470 \text{ nm} \leq \lambda_s \leq 1628 \text{ nm}$  to produce a red wavelength.

The Sellmeier equations for KTA which we use for the calculation of the wavelengths of parametric generation [129] and SFG [131] are given as

$$n_x^2 = 1.90713 + \frac{1.23522\lambda^2}{\lambda^2 - 0.0387774864} - 0.01025\lambda^2, \quad (3.3)$$

$$n_y^2 = 2.15912 + \frac{1.00099\lambda^2}{\lambda^2 - 0.0477160336} - 0.01096\lambda^2, \quad (3.4)$$

$$n_z^2 = 2.14786 + \frac{1.29559\lambda^2}{\lambda^2 - 0.0516152961} - 0.01436\lambda^2, \quad (3.5)$$

and

$$n_x^2 = 2.1495 + \frac{1.0203\lambda^{1.9951}}{\lambda^{1.9951} - 0.042378} + \frac{0.5531\lambda^{1.9567}}{\lambda^{1.9567} - 72.3045}, \quad (3.6)$$

$$n_y^2 = 2.1308 + \frac{1.0564\lambda^{2.0017}}{\lambda^{2.0017} - 0.042523} + \frac{0.6927\lambda^{1.7261}}{\lambda^{1.7261} - 54.8505}, \quad (3.7)$$

$$n_z^2 = 2.1931 + \frac{1.2382\lambda^{1.8920}}{\lambda^{1.8920} - 0.059171} + \frac{0.5088\lambda^{2.0000}}{\lambda^{2.0000} - 53.2898}, \quad (3.8)$$

respectively, where  $n_x$ ,  $n_y$ , and  $n_z$  are the principle refractive indices of the crystal and  $\lambda$  is in  $\mu\text{m}$ .

### 3.2 Experimental Configuration

The experimental setup for the nanosecond KTA OPO is shown in Fig. 3.1. The pump source is a 20 Hz flashlamp-pumped  $Q$ -switched Nd:YAG laser (Powerlite 6020, Continuum) operating at 1064 nm, generating pulses of 12.2 ns duration (FWHM). The telescope lenses reduce the diameter of the pump beam that has a slightly elliptic Gaussian-like spatial profile almost 2.5-fold resulting in a 2.2-mm-diameter beam ( $1/e^2$  intensity point) with a divergence of 0.9 mrad (full angle).

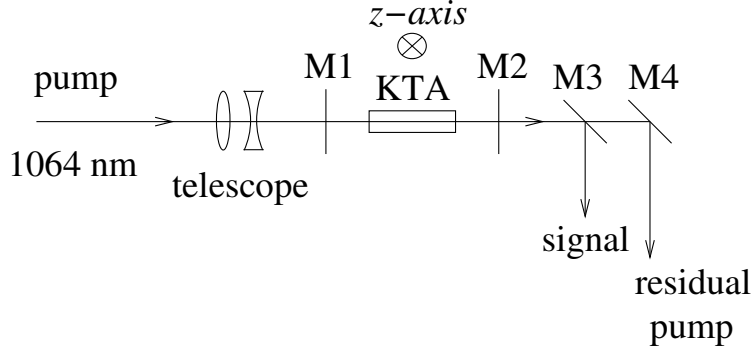


Figure 3.1: Experimental setup for the OPO.

Type-II birefringent phase matching facilitates optical parametric generation of a  $p$ -polarized (horizontal, fast axis) signal beam and an  $s$ -polarized (vertical, slow axis) idler beam from the  $p$ -polarized pump beam. Crystal-1, 2 and 3 generate signal wavelengths of 1530 nm, 1523 nm, and 1524 nm with the corresponding idler wavelengths of 3493 nm, 3530 nm, and 3525 nm, respectively, when the pump beam is incident to the crystal surface at  $0^\circ$  and collinear phase matching is used.

The 2.2-cm-long standing-wave cavity is made up of two flat mirrors, M1 and M2. M1 is a high reflector and M2 is an output coupler (OC), where two different OCs with reflectivities of  $R = 85\%$  and  $R = 74\%$  at the signal wavelength are used for characterization. The pump beam enters the cavity through M1, passes through the 20-mm-long KTA crystal and exits the cavity through M2, making a single pass. Both mirrors are also high transmitters at 1064 nm. The residual pump and signal output beams are separated from each other using dichroic

mirrors M3 and M4. The idler beam is totally absorbed in M2 (for both OCs) which is made from BK7 glass.

The maximum energy that can be obtained from our  $Q$ -switched 1064-nm pump source is 300 mJ for 7-ns-long pulses. Since the threshold intensity of the nanosecond OPOs can be reduced by increasing the duration of the pump pulse [132], we increased the pulse-width of the laser to 12.2 ns by increasing the  $Q$ -switch delay time (with respect to the flashlamp firing time). However, this is accompanied with a reduction in the energy output of the laser and results in a maximum available energy output of 64 mJ. Without changing the pulse-width, the output energy of the laser is further adjustable by a pair of optics composed of a  $\lambda/2$  wave-plate and a thin film polarizer (not shown in Fig. 3.1) placed at the exit of the laser.

The spatial profile of the pump beam measured at 6 cm away from the input face of the crystal is shown in Fig. 3.2. The maximum input energy used for pumping the KTA OPOs is 40 mJ and the corresponding peak intensity of the pump beam at the crystal input is calculated to be 160 MW/cm<sup>2</sup>.

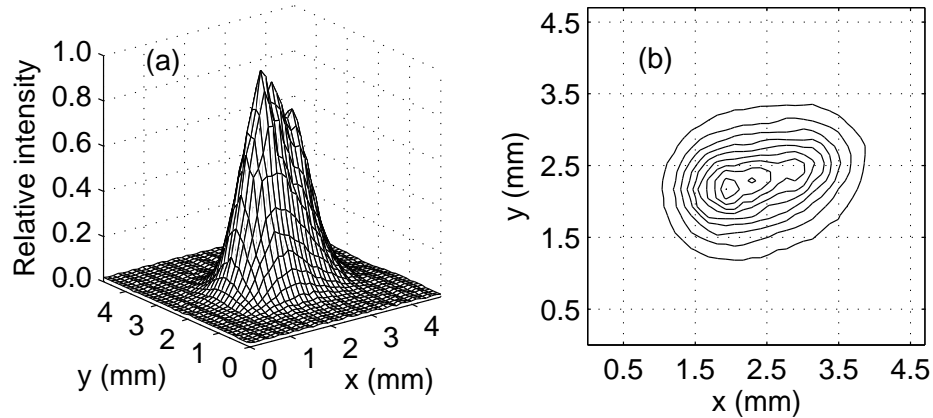


Figure 3.2: Spatial profile of the pump beam at 6 cm away from the input face of the crystal. (a) 3-D plot, (b) contour plot.

### 3.3 Characterization

For each crystal, we measured pump-to-signal energy conversion efficiencies, pump threshold energies, pump depletion ratios, temporal profiles and signal spectra.

The energy conversion efficiency is the ratio of the output signal energy per pulse to the input energy per pulse. The pump depletion is the ratio of the pump energy used in the nonlinear interaction to the input pump energy. The threshold energy for the OPO is determined by extrapolating a line fitted to the five points of the signal energy versus pump energy curve which are measured close to the threshold. Results are given as net values, that is, reflection and transmission losses incurred by the optical components are taken into account.

The energies of the signal, pump and depleted pump pulses are measured by an energy meter (Coherent Labmaster Ultima) with a pyroelectric energy sensor (Coherent LMP5). The sensor has a wavelength-calibrated alumina diffuser plate with approximately 25% transmission at 1064 nm in front.

The energy value of either the pump or signal is the average of the energies of at least 100 consecutive pulses. Averaging is especially necessary for an accurate measurement of the signal energies. Although pulse-to-pulse variation of pump energy is within  $\pm 1\%$  of its mean value, this variation in the signal energy is typically  $\pm 5\%$  for operation away from threshold. For operation near threshold, the variation is much larger, typically in the order of  $\pm 30\%$ . The pulse to pulse energy fluctuations have contributions from the phase changes because of vibration and temperature change, from fluctuations in the pump pulses, and from the quantum noise initiating the parametric oscillation [133, 134]. Phase changes can become the dominant factor when the imperfect mirror coatings slightly reflect the idler back into the OPO cavity, hence making the OPO sensitive to the phases of the reflected waves [3, 134, 135].

Temporal profiles of the pump and signal pulses are captured by a 400-MHz oscilloscope (HP-54502A). The pump (and depleted pump) and signal pulses are

detected by silicon and germanium *p-i-n* photodiodes, respectively. The oscilloscope is optically triggered with a second Si diode placed at the exit of the laser. Si and Ge photodiodes are specified to have rise-times less than 1 ns and 3.5 ns, respectively, for a 50-ohm load.

Spectral measurements are performed using a 1/4-meter monochromator (CVI Digikröm 240). The monochromator has three diffraction gratings with 300 grooves/mm, 600 grooves/mm and 1200 grooves/mm, which have upper wavelength scan limits of 6000 nm, 3000 nm and 1500 nm, respectively. Signal spectral measurements are performed using the diffraction grating with 600 grooves/mm and the minimum slit width of 10  $\mu\text{m}$  which provide a measurement resolution of approximately 0.12 nm.

Pump beam profile is obtained using a CCD camera (COHU 6400 series) and a beam analyzer (Spiricon LBA-100A). The upper limit of the spectral operation range of the CCD camera is 1100 nm, hence the signal beam profiles were not measured.

### 3.4 OPOs Based on Crystal-1

The experimental configuration for the OPO based on crystal-1 is as described in Section 3.2. Crystal-1 is  $5 \times 5 \times 20$  mm in size and cut along the  $\theta = 90^\circ$  and  $\phi = 24^\circ$  direction. A signal beam at 1530 nm and idler beam at 3493 nm are generated from the pump at 1064 nm using the polarization geometry described in Section 3.2. At the propagation direction of  $\theta = 90^\circ$  and  $\phi = 24^\circ$ , the signal wavelength is calculated to be 1528 nm using the Sellmeier equations in Ref. [129] and the effective nonlinear coefficient  $d_{\text{eff}}$  is calculated to be 3 pm/V using the nonlinear tensor data given in Ref. [127] with the correction due to walk-off included and dispersion in the nonlinear coefficients taken into account by employing Miller's rule [128]. The pump and signal beams have relatively small walk-off angles of  $0.12^\circ$  and  $0.11^\circ$ , respectively, which are calculated using the expressions in Ref. [136], whereas the idler beam has no walk-off. The crystal has antireflection

coatings for both the pump and signal wavelengths on both surfaces.

### 3.4.1 Output Energy versus Input Energy

Figure 3.3 shows the output signal energy, energy conversion efficiency and pump depletion as functions of the pump energy for the crystal-1 OPO with the OC reflectivities of  $R = 85\%$  and  $R = 74\%$ .

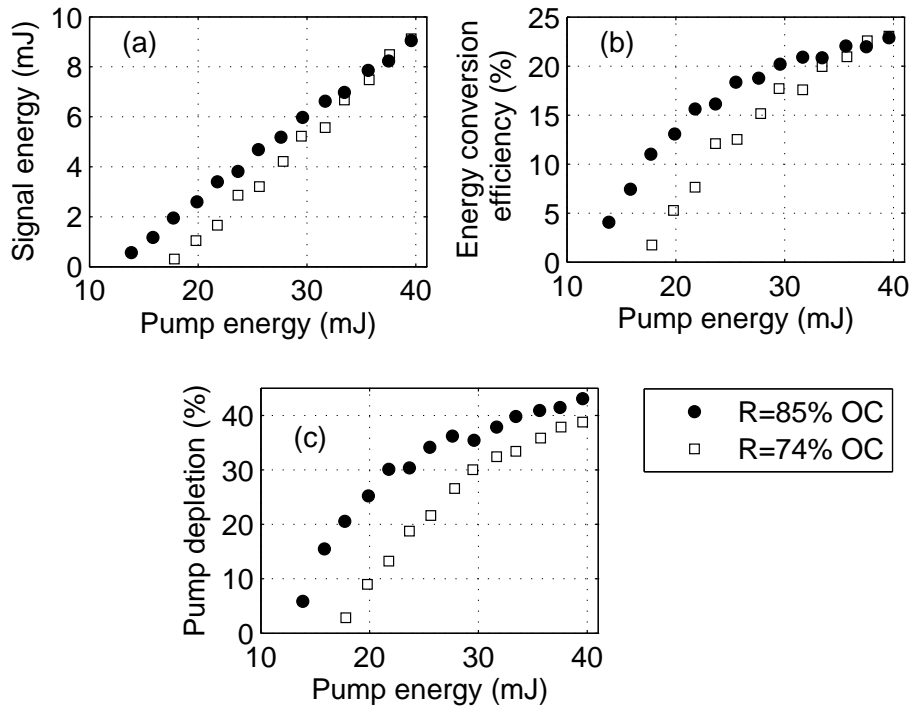


Figure 3.3: (a) Signal energy, (b) energy conversion efficiency, and (c) pump depletion as functions of input pump energy of the crystal-1 OPO with the OC reflectivities of  $R = 85\%$  and  $R = 74\%$ .

For the OPO with the  $R = 85\%$  OC, a maximum of 9.1 mJ signal energy is obtained at a pump energy of 39.6 mJ (3.2 times threshold), corresponding to 22.9% energy conversion efficiency and 43.1% pump depletion. The threshold energy of the OPO is 12.4 mJ. Using the pump depletion and signal energy data, the residual cavity loss at the signal wavelength is calculated to be 4.5%. At full input energy, the intracavity signal energy is 61.9 mJ.

For the OPO with the  $R = 74\%$  OC, again a maximum of 9.1 mJ signal energy is obtained at a pump energy of 39.6 mJ (2.3 times threshold), corresponding to 23% energy conversion efficiency and 38.8% pump depletion. The threshold energy of the OPO is 17.1 mJ, which is higher than that of the OPO with the  $R = 85\%$  OC due to an increase in the total cavity loss experienced by the signal. However, the residual cavity loss at the signal wavelength is calculated to be 4.5% which is the same with the value for the OPO with the  $R = 85\%$  OC. This is as expected since only the useful loss experienced by the intracavity signal field increases for a decrease in the reflectivity of the OC. Again due to the larger total cavity loss compared to that of the OPO with the  $R = 85\%$  OC, the intracavity signal energy is lower, which is 34.4 mJ at full input energy.

Energy conversion efficiencies provided by the OPOs with the  $R = 85\%$  and  $R = 74\%$  OCs are approximately the same. This suggests that the optimum output coupler reflectivity to be used for achieving the maximum energy conversion efficiency is between 74% and 85%.

### 3.4.2 Time Profiles

During the build-up time for the signal and idler, the depleted pump profile follows the pump profile. Just above threshold, the pump starts to be depleted, parametric generation into signal and idler beams occurs and after a short period the depleted pump profile exhibits a decline. For a larger input pump energy per pulse, the decline is more rapid. The sharp decline of the depleted pump ends at a time point where the depleted pump power is close to the threshold power of the pump and provided that there is no backconversion of the signal energy into the pump energy, the depleted pump decreases rather slowly after this point for a period of time until the pump power falls below threshold [137, 138]. The build-up time required to achieve parametric oscillation causes a temporal compression of the output signal pulse with respect to the pump pulse. For larger pump energies per pulse, this time is shorter, hence the signal pulse is broader.

Time profiles of the pump and depleted pump pulses of the crystal-1 OPO

with the  $R = 85\%$  OC for varying pump energies are shown in Fig. 3.4. For the same input pump levels, time profiles of the output signal pulses are shown in Fig. 3.5. The pulse-widths (FWHM) of the corresponding pulses at each pump level are given in Table 3.2. The pump pulse-width (FWHM) is kept fixed at  $12.4 \pm 2\%$  ns for these measurements.

It is clearly seen in Fig. 3.4 that as the pump energy increases, the pump depletion starts earlier and hence the build-up time for the signal is less, which is as expected. Sharp features of the depleted pump profiles for input energies greater than 24.7 mJ are not resolved due to the bandwidth limitation imposed by the fall-time of the detector. For increasing input pump energies, the pulse-width of the depleted pump pulse decreases down to 9.3 ns at a pump energy of 24.7 mJ, however then increases up to 11.9 ns at a pump energy of 39.5 mJ (Table 3.2).

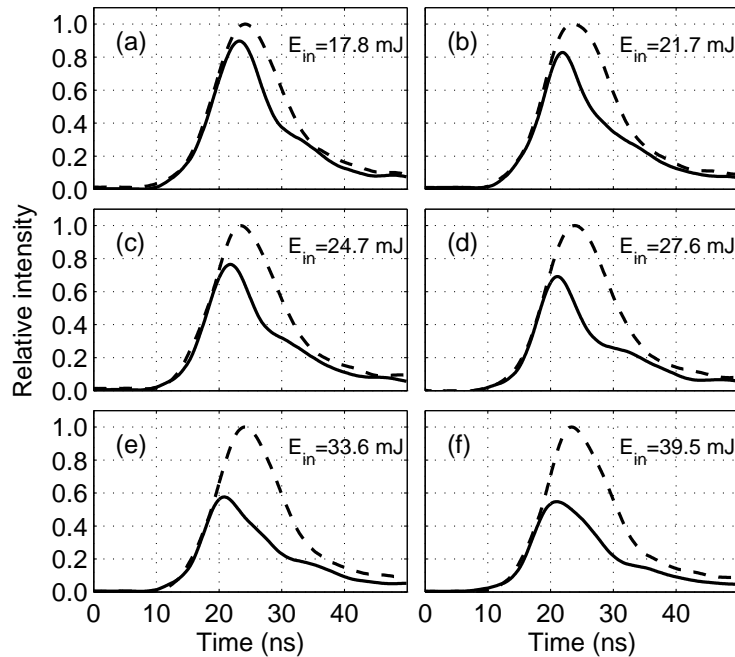


Figure 3.4: Time profiles of the pump pulse (dashed curves) and depleted pump pulse (solid curves) of the crystal-1 OPO with the  $R = 85\%$  OC for various input pump energies  $E_{in}$ .

As shown in Fig. 3.5, as a result of an increase in pump energy, the signal generation starts earlier due to the reduced build-up time. Furthermore, the

signal pulse broadens with increasing pump energies resulting in pulse-widths ranging from 7.9 ns at a pump energy of 17.8 mJ to 11.3 ns at a pump energy of 39.5 mJ.

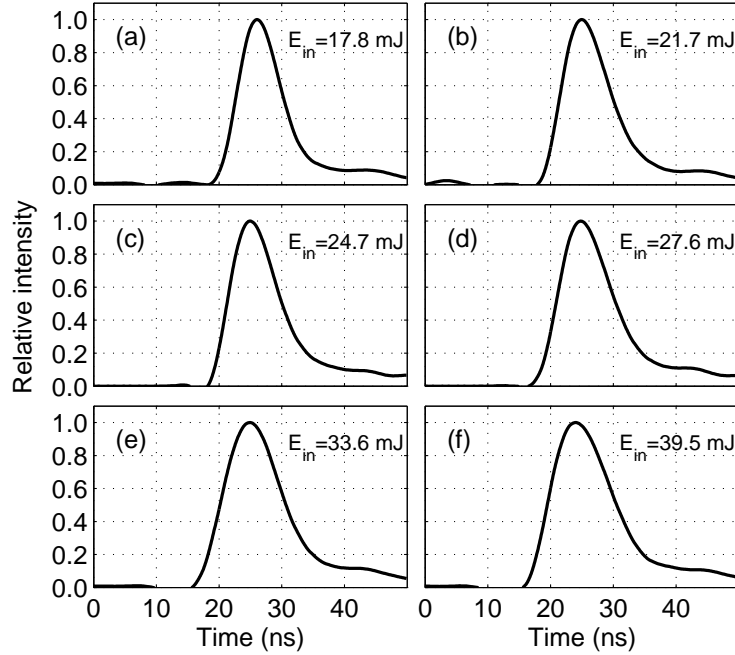


Figure 3.5: Time profiles of the signal pulse of the crystal-1 OPO with  $R = 85\%$  OC for various input pump energies  $E_{in}$ .

Pump energy (mJ)	Pump (ns)	Depleted pump (ns)	Signal (ns)
17.8	12.7	9.7	7.9
21.7	12.7	9.5	8.7
24.7	12.4	9.3	9.0
27.6	12.3	9.8	10.0
33.6	12.2	11.8	10.4
39.5	12.2	11.9	11.3

Table 3.2: Pulse-widths (FWHM) for various pump energies.

For the OPO with the  $R = 74\%$  OC, time profiles of the pump, depleted pump, and signal with corresponding pulse-widths (FWHM) of 12.9 ns, 11.0 ns, and 9.5 ns, respectively, are shown in Fig. 3.6. These profiles are measured at the pump energy of 39.5 mJ. The signal pulse-width (9.5 ns) is less than the

11.3 ns value measured for the OPO with the  $R = 85\%$  OC pumped at the same input energy. The reason for the reduced pulse-width is the larger cavity loss experienced by the signal as a result of larger output coupling, the resultant increase in pulse build-up time and decrease in the photon lifetime.

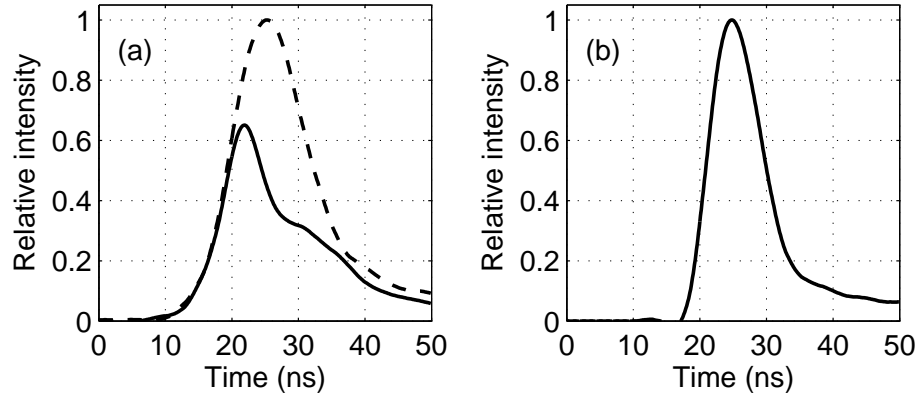


Figure 3.6: (a) Time profiles of the pump (dashed curve) and depleted pump (solid curve) pulses, (b) time profile of the signal pulse of the crystal-1 OPO with the  $R = 74\%$  OC. The pump energy is 39.5 mJ.

### 3.4.3 Signal Spectra

Our OPO exhibits broadband operation since the pump source is not an injection seeded laser but exhibits multi-mode operation, the OPO is not injection seeded or we do not use intracavity spectral filtering. The spectra of the signal beam which have spectral bandwidths of 1.1 nm and 0.5 nm are shown in Fig. 3.7 for the crystal-1 OPO with the  $R = 85\%$  OC pumped at two different pump energies of 17.6 mJ and 39.6 mJ with the corresponding signal energies of 1.9 mJ and 9.1 mJ, respectively. An increase in the input energy results in spectral narrowing due to smaller number of cavity modes that are favored during the build-up time of the parametric oscillation. Both spectra peak at 1529.7 nm, which is reasonably close to the signal wavelength of 1528.3 nm calculated using Equations (3.3)–(3.5).

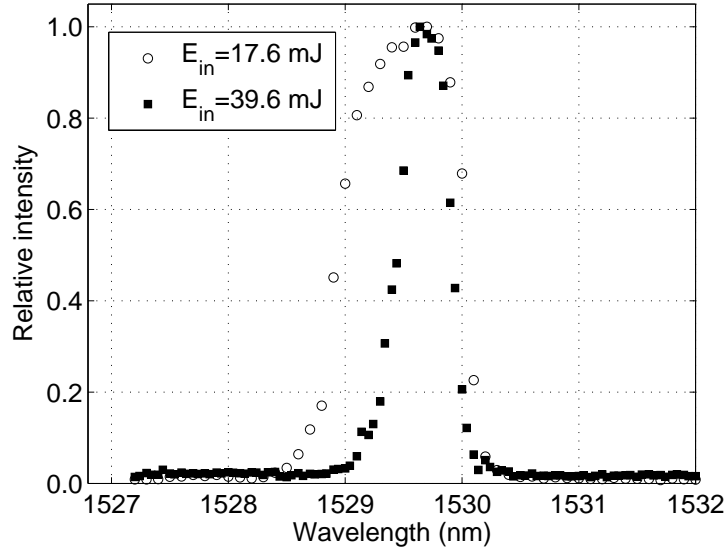


Figure 3.7: Spectra of the signal beam of the crystal-1 OPO with the  $R = 85\%$  OC at the pump energies of 17.6 mJ and 39.6 mJ.

### 3.5 OPOs Based on Crystal-2

The experimental configuration for the OPO based on crystal-2 is as described in Section 3.2. Crystal-2 is  $5 \times 5 \times 20$  mm in size and cut along the  $\theta = 90^\circ$  and  $\phi = 33^\circ$  direction. A signal beam at 1523 nm and idler beam at 3530 nm are generated from the pump at 1064 nm using the polarization geometry described in Section 3.2. At the propagation direction of  $\theta = 90^\circ$  and  $\phi = 33^\circ$ , the signal wavelength is calculated to be 1524 nm using the Sellmeier equations in Ref. [129] and the effective nonlinear coefficient  $d_{\text{eff}}$  is calculated to be 2.8 pm/V using the nonlinear tensor data given in Ref. [127] with the correction due to walk-off included and dispersion in the nonlinear coefficients taken into account by employing Miller's rule [128]. The pump and signal beams have relatively small walk-off angles of  $0.14^\circ$  and  $0.13^\circ$ , respectively, which are calculated using the expressions in Ref. [136], whereas the idler beam has no walk-off. The crystal has antireflection coatings for both the pump and signal wavelengths on both surfaces.

### 3.5.1 Output Energy versus Input Energy

We have observed a structural inhomogeneity in crystal-2 depending on the lateral position of the pump beam on the surface of the crystal which results in a variation of the effective nonlinear coefficient. The crystal is displaced laterally in the cavity and at several positions of the crystal with respect to the pump beam, the performance of the OPO is investigated. The propagation direction of the pump beam is kept fixed at  $\theta = 90^\circ$  and  $\phi = 33^\circ$  at all positions of the crystal. The highest energy output is achieved at a certain position of the crystal, and labelled as the first position. The OPO is characterized in terms of the output signal energy, energy conversion efficiency and pump depletion at this position and a second position for comparison.

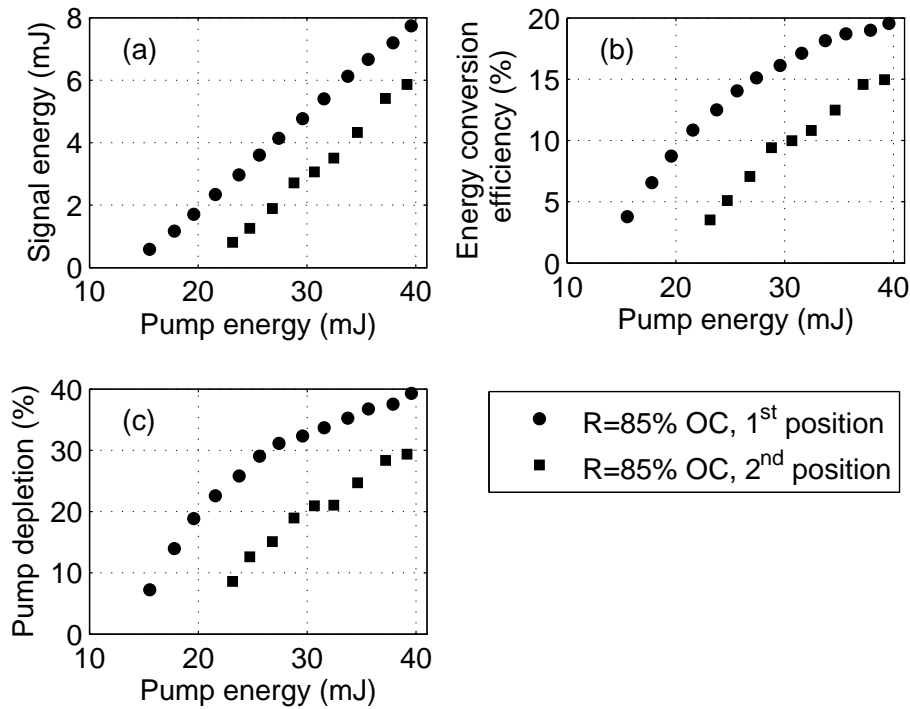


Figure 3.8: (a) Signal energy, (b) energy conversion efficiency, and (c) pump depletion as functions of input pump energy of the crystal-2 OPO with the  $R = 85\%$  OC for the first and second crystal positions.

Figure 3.8 shows the output signal energy, energy conversion efficiency and pump depletion as functions of the pump energy for the OPO using the  $R = 85\%$

OC with the crystal located at the first and second positions.

When the crystal is located at the first position, a maximum of 7.7 mJ signal energy is obtained at a pump energy of 39.6 mJ (2.9 times threshold), corresponding to 19.5% energy conversion efficiency and 39.3% pump depletion. The threshold energy of the OPO is 13.7 mJ. Using the pump depletion and signal energy data, the residual cavity loss at the signal wavelength is calculated to be 5.9%, which is slightly larger than the 4.5% value measured for the OPO described in Section 3.4 due to the reduced reflectivity of the input mirror M1 at the signal wavelength (measured to be  $\sim 1.5\%$  less at the current wavelength compared to the one for the crystal-1 OPO). At full input energy, the intracavity signal energy is 52.3 mJ.

When the crystal is located at the second position, a maximum of 5.9 mJ signal energy is obtained at a pump energy of 39.2 mJ (1.9 times threshold), corresponding to an energy conversion efficiency of only 14.9% and a pump depletion of 29.4%. The threshold energy of the OPO is as high as 20.6 mJ. Using the pump depletion and signal energy data, the residual cavity loss at the signal wavelength is calculated to be 5.6%, which is similar to the value calculated for the first position of the crystal. This suggests that no new residual cavity losses are added for the second position of the crystal and hence the reduction in conversion efficiencies and the increase in the threshold energy compared to those for the first crystal position can only be due to a reduction in the  $d_{\text{eff}}$  value of the crystal as a result of the crystal inhomogeneity. Furthermore, at full input energy, the intracavity signal energy is only 39.6 mJ.

For the first crystal position, the output signal energy of the crystal-2 OPO (7.7 mJ) is about 15% less than that of the crystal-1 OPO (9.1 mJ) described in Section 3.4 when the same OC ( $R = 85\%$ ) and pump energy (39.6 mJ) are used for both cases. We attribute this discrepancy to possible differences in the manufacturing processes of the crystals, the reduced reflectivity of M1 at the signal wavelength of the crystal-2 OPO, and the reduced  $d_{\text{eff}}$  of the crystal-2 OPO (2.8 pm/V and 3.0 pm/V for crystal-2 and crystal-1, respectively) due to the larger propagation angle  $\phi$  as dictated by Equation (3.2).

### 3.5.2 Time Profiles

For the OPO with the  $R = 85\%$  OC and the crystal located at the first position, time profiles of the pump, depleted pump, and signal with corresponding pulse-widths (FWHM) of 12.7 ns, 14.2 ns, and 10.4 ns, respectively, are shown in Fig. 3.9. These profiles are measured at the highest pump energy of 39.6 mJ.

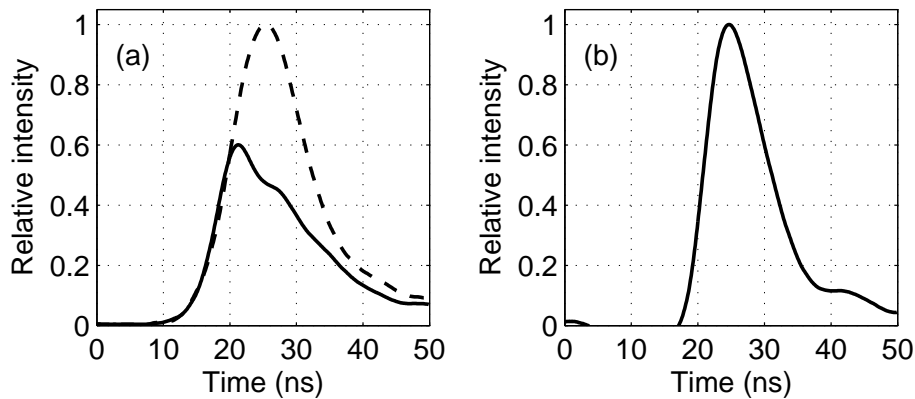


Figure 3.9: (a) Time profiles of the pump (dashed curve) and depleted pump (solid curve) and (b) the signal of the crystal-2 OPO with the  $R = 85\%$  OC. The pump energy is 39.6 mJ.

### 3.5.3 Signal Spectrum

For the OPO with the  $R = 85\%$  OC and the crystal located at the first position, the signal spectrum measured at full energy is shown in Fig. 3.10. The spectrum peaks at 1523.4 nm, which is quite close to the signal wavelength of 1524 nm calculated using Equations (3.3)–(3.5). The bandwidth of the spectrum is approximately 0.9 nm.

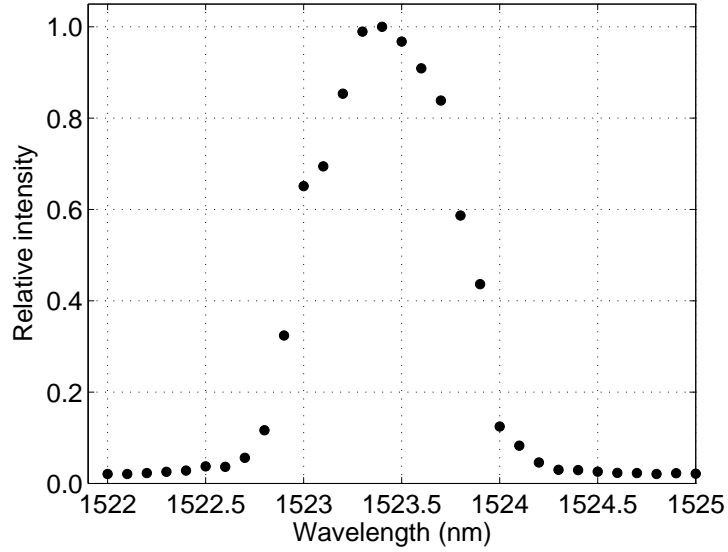


Figure 3.10: Spectrum of the signal beam of the crystal-2 OPO with the  $R = 85\%$  OC at a pump energy of 39.6 mJ. The crystal is located at the first position.

### 3.6 OPOs Based on Crystal-3

The experimental configuration for the OPO based on crystal-3 is as described in Section 3.2. Crystal-3 is  $5 \times 5 \times 20$  mm in size and cut along the  $\theta = 90^\circ$  and  $\phi = 32.6^\circ$  direction. A signal beam at 1524 nm and idler beam at 3525 nm are generated from the pump at 1064 nm using the polarization geometry described in Section 3.2. At the propagation direction of  $\theta = 90^\circ$  and  $\phi = 32.6^\circ$ , the signal wavelength is calculated to be 1524 nm using the Sellmeier equations in Ref. [129] and the effective nonlinear coefficient  $d_{\text{eff}}$  is calculated to be 2.8 pm/V using the nonlinear tensor data given in Ref. [127] with the correction due to walk-off included and dispersion in the nonlinear coefficients taken into account by employing Miller's rule [128]. The pump and signal beams have relatively small walk-off angles of  $0.14^\circ$  and  $0.13^\circ$ , respectively, which are calculated using the expressions in Ref. [136], whereas the idler beam has no walk-off. The crystal has antireflection coatings for both the pump and signal wavelengths on both surfaces.

### 3.6.1 Output Energy versus Input Energy

Figure 3.11 shows the output signal energy, energy conversion efficiency and pump depletion as functions of the pump energy for the crystal-3 OPO with the OC reflectivity of  $R = 74\%$ . A maximum of 7.2 mJ signal energy is obtained at a pump energy of 39.8 mJ (1.8 times threshold), corresponding to 18.2% energy conversion efficiency and 30.3% pump depletion. The threshold energy of the OPO is 21.7 mJ. Using the pump depletion and signal energy data, the residual cavity loss at the signal wavelength is calculated to be 4.3%. At full input energy, the intracavity signal energy is 27.3 mJ.

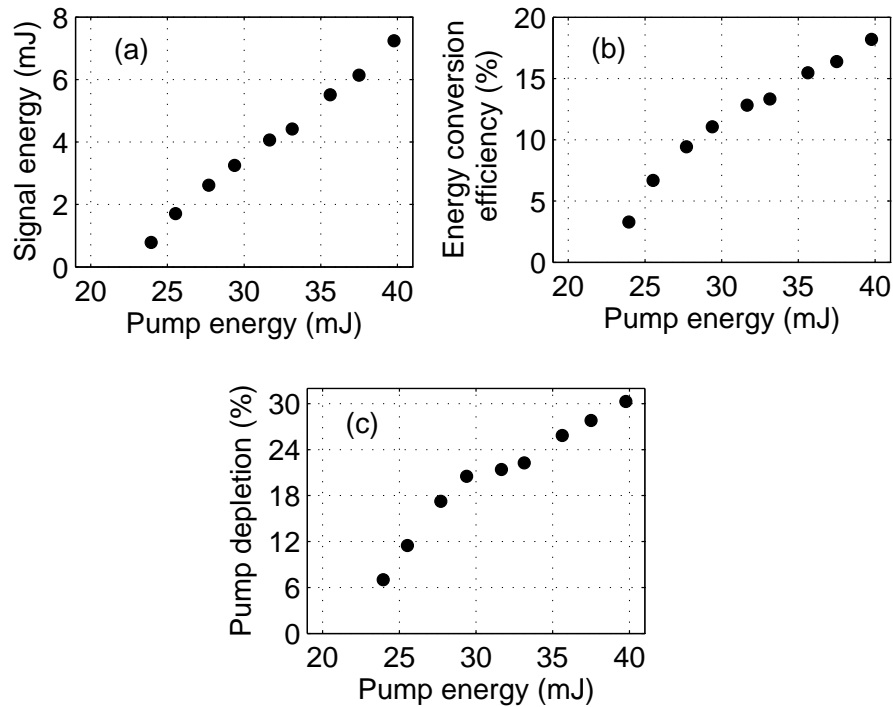


Figure 3.11: (a) Signal energy, (b) energy conversion efficiency, and (c) pump depletion as functions of input pump energy of the crystal-3 OPO with the  $R = 74\%$  OC.

The output signal energy of the crystal-3 OPO (7.2 mJ) is about 21% less than that of the crystal-1 OPO (9.1 mJ) described in Section 3.4 when the same OC ( $R = 74\%$ ) and similar pump energies (39.8 mJ and 39.6 mJ for the crystal-3 and crystal-1 OPOs, respectively) are used for both cases. Similar to the

case for the crystal-2 OPO described in Section 3.5, this discrepancy is due to possible differences in the manufacturing processes of the crystals and the reduced  $d_{\text{eff}}$  of the crystal-3 OPO (2.8 pm/V and 3.0 pm/V for crystal-3 and crystal-1, respectively).

### 3.6.2 Time Profiles

For the crystal-3 OPO with the  $R = 74\%$  OC, time profiles of the pump, depleted pump, and signal with corresponding pulse-widths (FWHM) of 12 ns, 9.8 ns, and 7.9 ns, respectively, are shown in Fig. 3.12. These profiles are measured at the highest pump energy of 39.8 mJ.

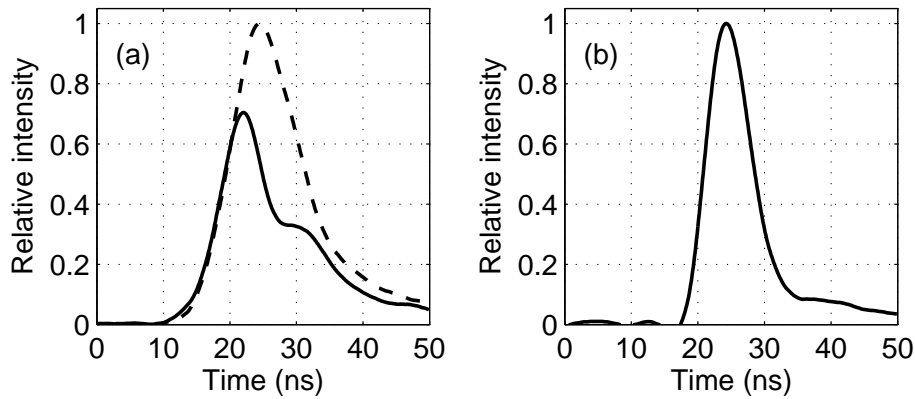


Figure 3.12: (a) Time profiles of the pump (dashed curve) and depleted pump (solid curve) pulses, (b) time profile of the signal pulse of the crystal-3 OPO with the  $R = 74\%$  OC.

### 3.6.3 Signal Spectrum

For the crystal-3 OPO with the  $R = 74\%$  OC, the signal spectrum measured at full energy is shown in Fig. 3.13. The spectrum peaks at 1524.0 nm, which is quite close to the signal wavelength of 1524.2 nm calculated using Equations (3.3)–(3.5). The bandwidth of the spectrum is approximately 0.7 nm.

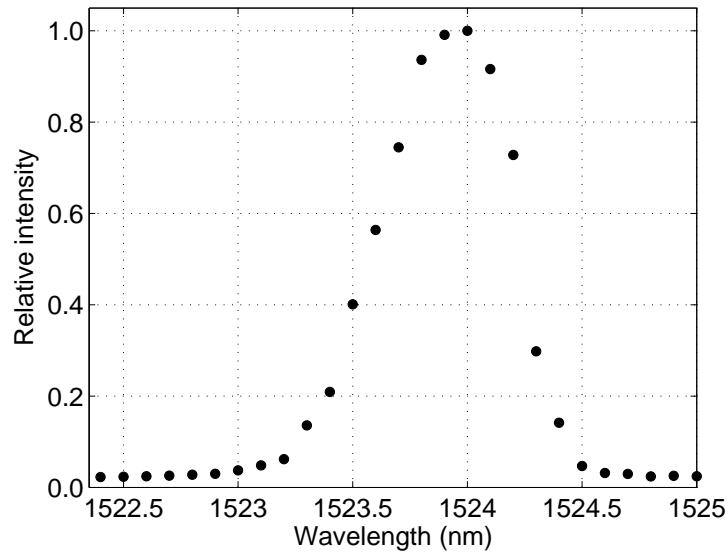


Figure 3.13: Spectrum of the signal beam of the crystal-3 OPO with the  $R = 74\%$  OC at a pump energy of 39.8 mJ.

### 3.7 Summary

In summary, we have demonstrated nanosecond optical parametric oscillators based on three different KTA crystals. These OPOs are pumped at  $0^\circ$  of incidence to the crystal surface by a Q-switched 1064 nm Nd:YAG laser producing 12.2-ns-long pulses with a maximum energy of 40 mJ per pulse. The OPOs based on crystal-1, 2, and 3 generate emission at the signal wavelengths of 1530 nm, 1523 nm and 1524 nm, respectively. These OPOs have been characterized in terms of their output energies, time profiles and spectra. The highest pump-to-signal energy conversion efficiency obtained in these experiments is 22.9%, corresponding to a pump depletion of 43.1%, which is achieved with the OPO based on crystal-1 using an output coupler with a reflectivity of  $R = 85\%$ . This crystal is cut along a direction with an angle  $\phi$  which is about  $9^\circ$  less than those of the other crystals. Crystal-2 and 3 are employed in the sum-frequency generating OPO devices described in the next chapter.

## Chapter 4

# Nanosecond Sum-Frequency Generating Optical Parametric Oscillator Experiments

In this chapter, we present our nanosecond sum-frequency generating optical parametric oscillator experiments. These experiments were performed using two KTA crystals with labels crystal-2 and crystal-3, which were also employed in the nanosecond OPO experiments described in the previous chapter. The cut-angles of these crystals are given in Table 3.1 in Chapter 3. Both crystals are  $5 \times 5 \times 20$  mm in size and their surfaces are anti-reflection coated for 1064 nm and 1525 nm.

The sum-frequency generating OPO (SF-OPO) in which crystal-2 is used for both parametric generation and SFG is the first demonstration of an optical parametric oscillator employing simultaneous phase matching and operating in the nanosecond regime [52, 53]. Pumped by a nanosecond  $Q$ -switched Nd:YAG laser at 1064 nm in a single-pass configuration, this compact device generates red output pulses at 627 nm with more than 20% 1064-nm-to-627-nm energy conversion efficiency.

A similar SF-OPO based on crystal-3 in which the pump at 1064 nm makes a

double-pass through the KTA crystal generates red output pulses at 627 nm with up to 29% 1064-nm-to-627-nm energy conversion efficiency. When this device is pumped in a single-pass configuration, a energy conversion efficiency of more than 19% is achieved.

We first describe the experimental configurations for the single-pass and double-pass 1064-nm-pumped nanosecond SF-OPOs and explain how these devices are characterized. Subsequently, we present the results of the characterization of single-pass SF-OPOs based on crystal-2 in terms of their energy outputs, input-output time profiles, spatial profiles, and spectra. We also present the results of a similar characterization for both double-pass and single-pass SF-OPOs based on crystal-3. Finally, the previous work done for modelling nanosecond OPOs is briefly explained and a model for nanosecond SF-OPOs is described along with a comparison of its predictions with the experimental results.

## 4.1 Experimental Configurations

In this section, we first describe the experimental configuration for the single-pass SF-OPO. This configuration is used for the SF-OPOs based on both crystal-2 and crystal-3. First, the details are given for the device based on crystal-2. Next, the experimental configuration for the double-pass SF-OPO is described. This configuration is only used for the crystal-3 SF-OPO. Within the same section, the details related to the single-pass SF-OPO based on crystal-3 are also presented.

### 4.1.1 Single-pass SF-OPO Based on Crystal-2

Crystal-2 was designed so that when pumped at 1064 nm, it is simultaneously phase matched for optical parametric generation and SFG at the signal and pump wavelengths. The polarization diagram for the simultaneously phase-matched interaction is already shown in Fig. 2.7 (Section 2.9.3). Type-II birefringent phase matching facilitates optical parametric generation of a  $p$ -polarized (horizontal,

fast axis) signal beam at 1525 nm and an  $s$ -polarized (vertical, slow axis) idler beam at 3520 nm from the  $p$ -polarized pump beam at 1064 nm. SFG with an  $s$ -polarized beam at the signal wavelength and a  $p$ -polarized beam at the pump wavelength as its inputs is simultaneously phase-matched for the same direction of propagation in the KTA crystal, again in a type-II polarization geometry. Coupling a portion of the  $p$ -polarized intracavity signal beam to  $s$ -polarization with a retarder plate facilitates the generation of a  $p$ -polarized sum-frequency output beam at 627 nm. This simultaneous phase matching polarization geometry belongs to class-D SF-OPOs, as defined in Ref. [59].

We experimentally determined that simultaneous phase matching for crystal-2 at our wavelengths occurs at  $\theta = 90^\circ$  and  $\phi = 30.1^\circ$ , requiring a corresponding tilt (the cut-angle of the crystal is  $\theta = 90^\circ$  and  $\phi = 33^\circ$ ). This propagation angle is approximately the same with the value calculated using the Sellmeier coefficients given in Ref. [129] for parametric generation and those given in Ref. [131] for SFG. While the beams polarized along the slow axis ( $z$ -axis) experience no walk-off, the calculated walk-off angles associated with the beams polarized along the fast axis are relatively small, with the maximum value being  $0.15^\circ$  for the sum-frequency beam.

The experimental setup for the single-pass SF-OPO based on crystal-2 is shown in Fig. 4.1. The pump source is a 4 Hz flash-lamp-pumped  $Q$ -switched Nd:YAG laser operating at 1064 nm, generating 40 mJ pulses of 14.7 ns duration (FWHM). The pump laser is the same one used for the experiments described in the previous chapter. The telescope lenses reduce the diameter of the pump beam that has a slightly elliptic Gaussian-like spatial profile almost 2.5-fold resulting in a 1.6-mm-diameter beam ( $1/e^2$  intensity point) with a divergence of 0.8 mrad (full angle).

The 4.8-cm-long L-shaped cavity is made up of three flat mirrors, M1, M2, and M3, which are all high reflectors at the signal wavelength. The pump beam enters the cavity through M1 and exits the cavity through M2, making a single pass. Both mirrors are also high transmitters at 1064 nm. When pumped above threshold, a  $p$ -polarized intracavity signal beam is generated. An intracavity  $\lambda/4$

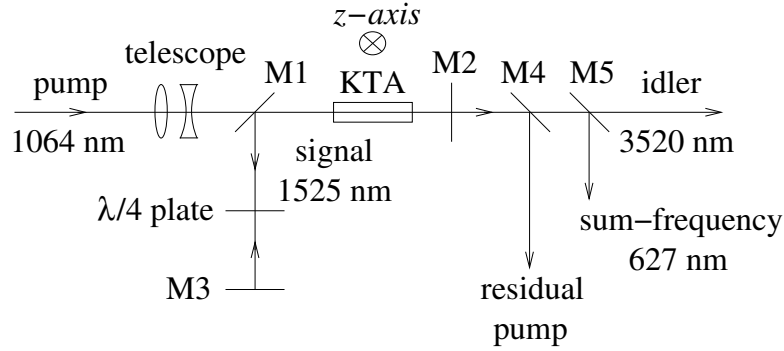


Figure 4.1: Experimental setup for the single-pass SF-OPO.

plate whose surfaces are antireflection coated at 1525 nm acts as a polarization rotator to couple a portion of the signal beam to  $s$ -polarization. Simultaneously phase-matched SFG results in the  $s$ -polarized component of the signal to be summed with the pump beam to produce a sum-frequency beam at 627 nm. This red beam exits the cavity through M2. The residual pump and red output beams are separated from each other using dichroic mirrors M4 and M5. The idler beam at 3520 nm is mostly absorbed in M2, M4, and M5, which are made from BK7 glass. Only a small amount of idler, 0.4 mJ at the highest input pulse energy, is measured after these mirrors.

Replacing the high reflector M2 with an output coupling mirror for the signal results in a dual-wavelength output at 1525 nm and 627 nm. We used this device configuration for characterization purposes including the determination of the simultaneous phase-matching angle and the signal wavelengths generated by the device when the crystal is angle-tuned and estimation of the intracavity signal energy of the SF-OPO. If the polarization rotation angle provided by the intracavity retarder plate is set to be  $0^\circ$ , there will be no SFG and the device will merely operate as an OPO where the resonant signal field is coupled out of the cavity through M2. When M2 is an  $R = 85\%$  OC at 1525 nm, the idler is totally absorbed in this mirror, hence, instead of the idler beam, only the signal beam is available after M4 and M5 in Fig. 4.1.

The pump beam of the SF-OPO based on crystal-2 is slightly smaller in diameter than the one used for the OPO experiments (1.6 mm versus 2.2 mm)

described in the previous chapter due to the larger supply voltage used for the Nd:YAG laser and the resultant increase in thermal lensing in the Nd:YAG rod. The spatial profile of the pump beam measured at 13 cm away from the input face of the crystal is shown in Fig. 4.2. The peak pump intensity at the crystal input for a maximum pulse energy of 40 mJ used in the experiments is calculated to be  $260 \text{ MW/cm}^2$ . We chose not to increase our pump intensity any further than this, since the damage threshold of the surface coatings on the KTA crystal are specified to be  $500 \text{ MW/cm}^2$  for a 20-ns pulse at 1064 nm.

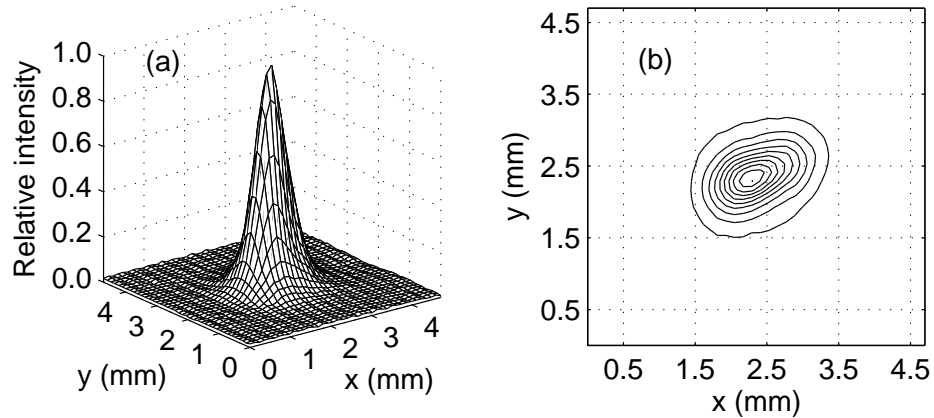


Figure 4.2: Spatial profile of the pump beam of the single-pass SF-OPO based on crystal-2 at 13 cm away from the input face of the crystal. (a) 3-D plot, (b) contour plot.

#### 4.1.2 Double-pass and Single-pass SF-OPOs Based on Crystal-3

The simultaneous phase-matching polarization geometry for crystal-3 and wavelengths of the beams involved in both parametric generation and SFG processes are the same with those given in the previous section. We experimentally determined that simultaneous phase matching for crystal-3 at these wavelengths occurs at  $\theta = 90^\circ$  and  $\phi = 30.8^\circ$ , requiring a corresponding tilt (the cut-angle of the crystal is  $\theta = 90^\circ$  and  $\phi = 32.6^\circ$ ). This propagation angle is still quite close to the value calculated using the Sellmeier coefficients given in Ref. [129]

for parametric generation and those given in Ref. [131] for SFG, which is  $\theta = 90^\circ$  and  $\phi = 30.1^\circ$ .

The experimental setup for the double-pass SF-OPO based on crystal-3 is shown in Fig. 4.3. The pump source is the same with the one used for the crystal-2 SF-OPO which generates 32 mJ pulses of 17.8 ns duration (FWHM) with a 4 Hz repetition rate. The telescope lenses reduce the diameter of the pump beam that has a slightly elliptic Gaussian-like spatial profile down to 1.3 mm at the input face of the crystal and the resulting beam has a divergence of 3 mrad (full angle). Smaller beam size and larger divergence angle are due to the larger thermal lensing induced in the Nd:YAG rod by a new flash-lamp installed in place of the old one. The spatial profile of the pump is similar to the one shown in Fig. 4.2. The peak pump intensity at the crystal input for a maximum pulse energy of 20 mJ used in the double-pass SF-OPO experiments is calculated to be  $140 \text{ MW/cm}^2$ .

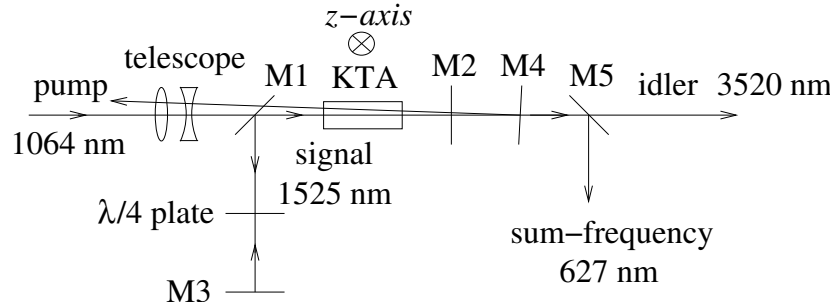


Figure 4.3: Experimental setup for the double-pass SF-OPO.

The 4.8-cm-long L-shaped cavity is made up of three flat mirrors, M1, M2, and M3, which are all high reflectors at the signal wavelength. The pump beam makes a double-pass through the KTA crystal as it enters the cavity through M1, exits through M2, and returns into the cavity upon a reflection from the high reflector mirror M4 placed about 3 mm away from M2. M4 is slightly tilted to prevent the back-reflection from coupling into the pump laser cavity by providing an angle of  $0.2^\circ$  between the directions of the incident and return pump beams in the crystal. Both M1 and M2 are high transmitters at 1064 nm. When pumped above threshold, a  $p$ -polarized intracavity signal beam is generated. An intracavity  $\lambda/4$  plate whose surfaces are antireflection coated at 1525 nm acts as

a polarization rotator to couple a portion of the signal beam to *s*-polarization. Simultaneously phase-matched SFG results in the *s*-polarized component of the signal to be summed with the pump beam to produce a sum-frequency beam at 627 nm. This red beam exits the cavity through M2, passes through M4 and is reflected by M5, which is a high reflector at 627 nm. The idler beam at 3520 nm is totally absorbed in M2, M4, and M5, which are made from BK7 glass.

For the single-pass SF-OPO based on crystal-3, the experimental setup is already described in the previous section. The pump beam characteristics are the same as those given for the double-pass configuration. The peak pump intensity at the crystal input for a maximum pulse energy of 30 mJ used in the single-pass SF-OPO experiments is calculated to be 210 MW/cm<sup>2</sup>. Only a small amount of idler, 0.3 mJ at the highest input pulse energy, is measured after the mirrors external to the cavity.

## 4.2 Characterization

For each SF-OPO, we measured 1064-nm-to-627-nm energy conversion efficiencies, pump threshold energies, pump depletion ratios, temporal profiles, spatial profiles and spectra of the beams.

The energy conversion efficiency is the ratio of the output sum-frequency energy per pulse to the input energy per pulse. The pump depletion is the ratio of the pump energy used in the simultaneous parametric generation and SFG processes to the input pump energy. The threshold energy for the SF-OPO is determined by extrapolating a line fitted to five points of the sum-frequency energy versus pump energy curve which are measured close to the threshold. Results are given as net values, that is, reflection and transmission losses incurred by the optical components are taken into account.

The energy value of either the pump, signal, or sum-frequency is the average of the energies of at least 100 consecutive pulses. Averaging is especially necessary for an accurate measurement of the signal and sum-frequency energies. Although

pulse-to-pulse variation of pump energy is within  $\pm 1\%$  of its mean value, this variation in the sum-frequency energies is typically  $\pm 5\%$  for operation away from threshold. Reasons for a similar variation in the signal pulse energies of OPOs which are given in Section 3.3 are also valid for the variation in the sum-frequency pulse energies of SF-OPOs.

The equipment used in the SF-OPO experiments is the same as the equipment outlined in Section 3.3. The sum-frequency pulses are detected by the Si photodiode. Sum-frequency spectral measurements are performed using the monochromator with the diffraction grating that has 1200 grooves/mm and with the minimum slit width of  $10 \mu\text{m}$ . The resultant measurement resolution is approximately 0.06 nm. For measuring the time profile and relative energy of the intracavity signal, the signal energy leaking through M3 (Figs. 4.1 and 4.3) is detected by the Ge photodiode.

## 4.3 Results for the Single-Pass SF-OPO Based on Crystal-2

In this section, we present the experimental results for the single-pass SF-OPO based on crystal-3. The device is characterized in terms of its output energy as functions of both the polarization rotation angle and the input pump energy, the time profiles, spatial profiles, spectra of the beams and the experimental simultaneous phase matching angle. We mainly focus on the single-pass SF-OPO based on crystal-2 with a high reflector output mirror (M2 in Fig. 4.1), however at the end of this section, we also present similar results for the SF-OPO with a  $R = 85\%$  OC at the signal wavelength.

### 4.3.1 Output Energy versus Polarization Rotation Angle

In the SF-OPO, there is an optimum polarization rotation angle that maximizes the output pulse energy. When the fast axis of the intracavity retarder plate

is aligned with either the  $p$ - or  $s$ -polarization direction, there is no polarization rotation. In this case, the intracavity signal beam does not have an  $s$ -polarized component and hence there is no SFG. The residual cavity losses experienced by the signal beam is relatively small (approximately 3%), resulting in a low OPO threshold and high intracavity signal intensity. As the polarization rotation angle is increased by rotating the retarder plate, a portion of the  $p$ -polarized intracavity signal is coupled into  $s$ -polarization and SFG begins to take place. However, rotating the signal polarization effectively increases the total linear cavity loss experienced by the resonating  $p$ -polarized signal, increasing the OPO threshold. Consequently, at some polarization rotation angle above the optimum value, SF-OPO falls below threshold.

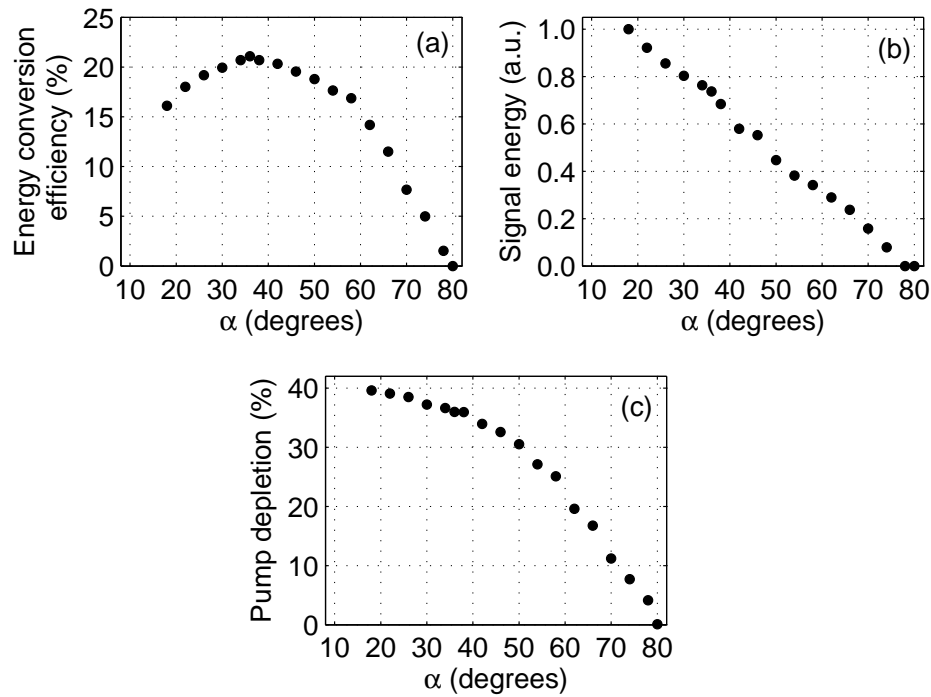


Figure 4.4: (a) Energy conversion efficiency, (b) relative intracavity signal energy, and (c) pump depletion as functions of polarization rotation angle  $\alpha$  of the single-pass SF-OPO based on crystal-2. Pump energy is held fixed at 39.2 mJ.

Figure 4.4 shows the 1064-nm-to-627-nm energy conversion efficiency, relative intracavity signal energy, and pump depletion as functions of the polarization rotation angle  $\alpha$  at a fixed pump energy of 39.2 mJ. A peak conversion efficiency

of 21.1% is obtained at an optimum polarization rotation angle of  $36^\circ$ . At this rotation angle, the pump depletion and intracavity signal energy are 36% and 44 mJ, respectively. The smallest  $\alpha$  is chosen to be  $18^\circ$  to avoid damage to the KTA crystal. At  $\alpha = 18^\circ$ , the energy conversion efficiency is 16.1%, the pump depletion is 39.6%, and the intracavity signal energy is estimated to be 60 mJ. Both the pump depletion and intracavity signal energy decrease monotonically as  $\alpha$  increases, due to the increasing total linear cavity loss experienced by the resonating  $p$ -polarized signal. The SF-OPO falls below threshold at  $\alpha = 80^\circ$ .

### 4.3.2 Output Energy versus Input Energy

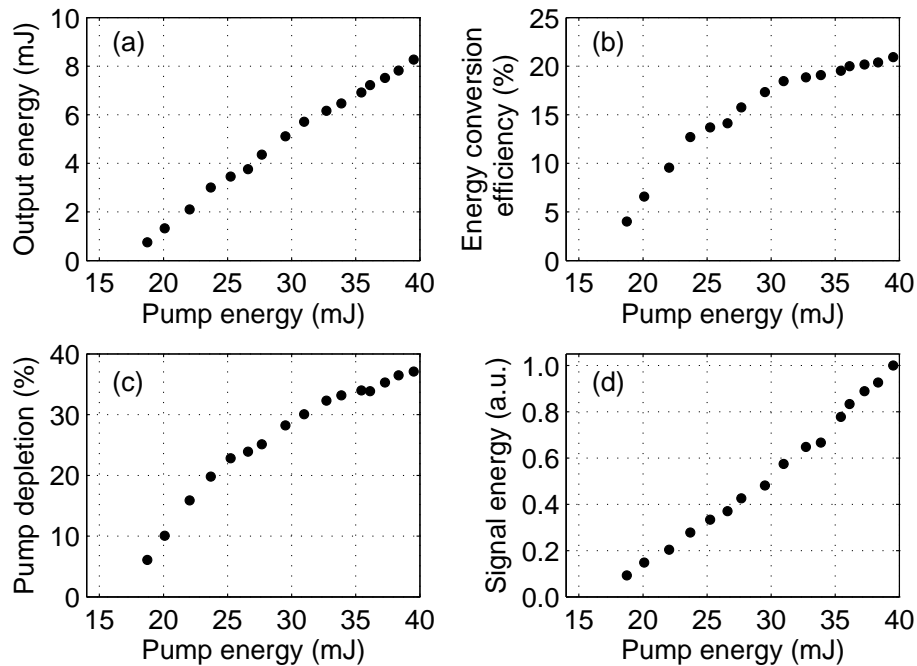


Figure 4.5: (a) Output energy, (b) energy conversion efficiency, (c) pump depletion, and (d) relative intracavity signal energy as functions of input pump energy of the single-pass SF-OPO based on crystal-2. Polarization rotation angle is held fixed at  $36^\circ$ .

Figure 4.5 shows the output sum-frequency energy, energy conversion efficiency, pump depletion, and relative intracavity signal energy as functions of the

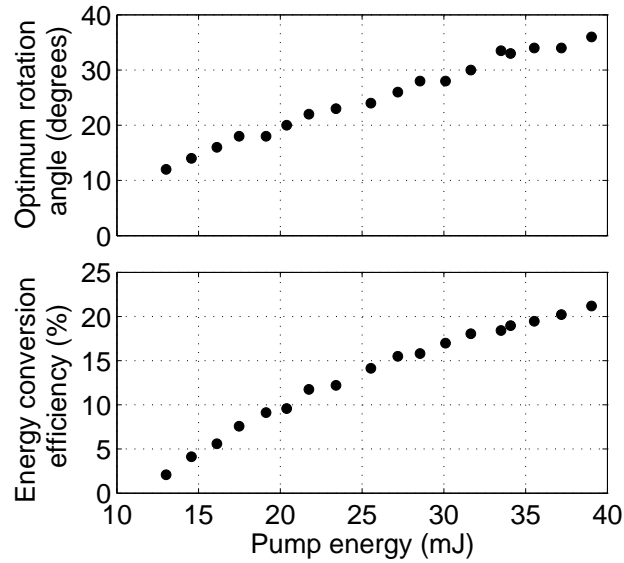


Figure 4.6: Optimum polarization rotation angle and maximum energy conversion efficiency as functions of pump energy of the crystal-2 SF-OPO.

pump energy while the polarization rotation angle is held fixed at  $36^\circ$ . A maximum of 8.3 mJ sum-frequency energy is obtained at a pump energy of 39.5 mJ, corresponding to 20.9% conversion efficiency and 37.1% pump depletion. At this pump level, the intracavity signal energy is 44 mJ. The threshold energy of the SF-OPO is 16.7 mJ at this polarization rotation angle.

For any input pump level, the output sum-frequency energy can easily be maximized by adjusting the polarization rotation angle. Figure 4.6 shows the maximum energy conversion efficiency and the optimum polarization rotation angle as functions of the input pump energy. The optimum polarization rotation angle decreases monotonically with decreasing pump energy.

### 4.3.3 Time Profiles

Figure 4.7 shows the time profiles of the pump, depleted pump, intracavity signal, and sum-frequency pulses of the single-pass SF-OPO based on crystal-2. These measurements were performed at the full input energy and optimum polarization

rotation angle. The pulse durations (FWHM) are 14.7 ns, 12.5 ns, 13.2 ns, and 10.4 ns for the pump, depleted pump, intracavity signal, and sum-frequency beams, respectively.

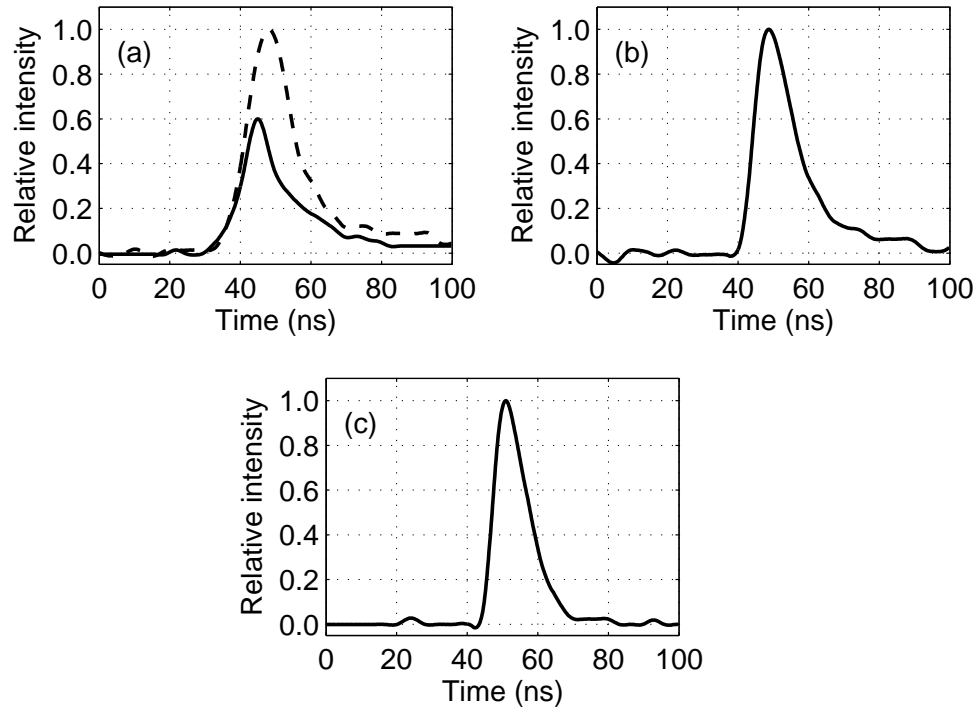


Figure 4.7: (a) Time profiles of the pump (dashed curve) and depleted pump (solid curve), (b) intracavity signal, and (c) sum-frequency pulses of the crystal-2 SF-OPO.

#### 4.3.4 Spectra of the Pump and Sum-Frequency

Figure 4.8 shows the spectra of the pump and sum-frequency beams obtained at the full input energy and optimum polarization rotation angle. Both spectra have a bandwidth of approximately 0.2 nm and the corresponding peaks are located at 1064.2 nm and 626.7 nm.

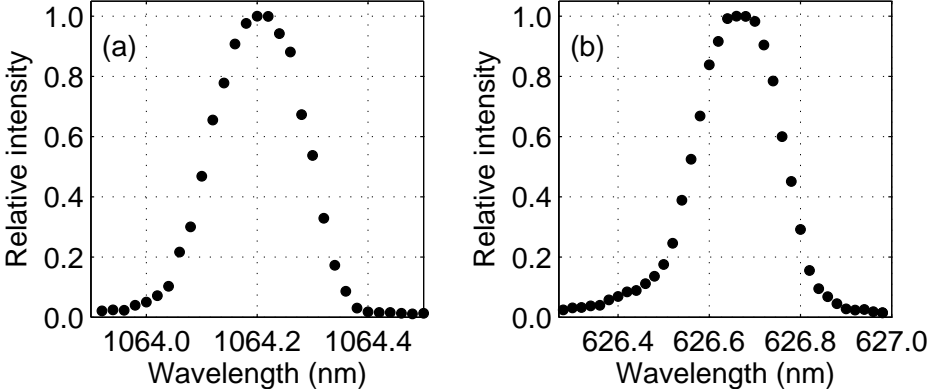


Figure 4.8: Spectra of (a) the pump and (b) sum-frequency beams of the single-pass SF-OPO based on crystal-2.

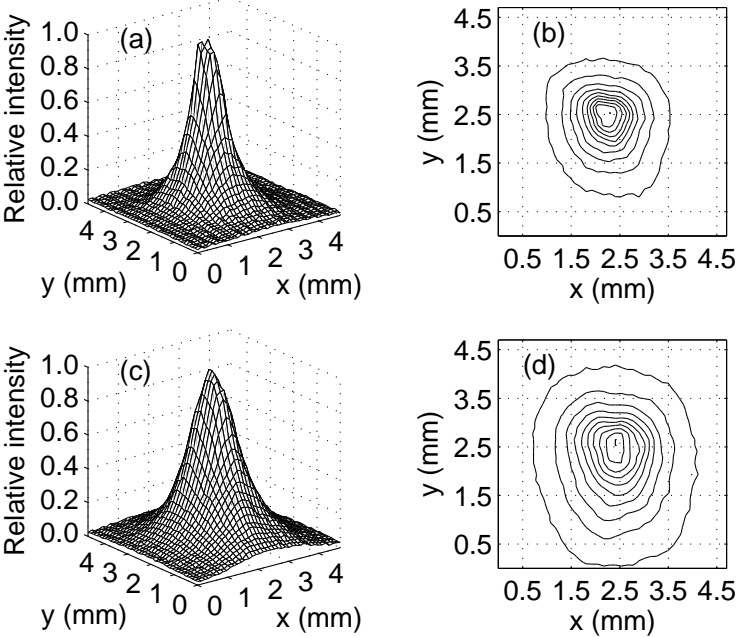


Figure 4.9: 3-D plots for the spatial profiles of the sum-frequency beam at (a) 56 cm and (c) 96 cm away from the input face of the crystal. The corresponding contour plots are shown in (b) and (d).

### 4.3.5 Spatial Profiles of the Sum-Frequency Beam

Figure 4.9 shows the spatial profiles of the sum-frequency beam obtained at 56 cm and 96 cm away from the input face of the crystal. These profiles are measured at the full input energy and optimum polarization rotation angle. The divergence of the beam is 1.8 mrad (full-angle), which is approximately 2.3 times of that of the input pump beam. The beam diameter ( $1/e^2$  intensity point) at the exit face of the crystal is about 2 mm and the beam has a peak intensity of 80 MW/cm<sup>2</sup> at this point.

### 4.3.6 Simultaneous Phase-Matching Angle and Signal Wavelengths with Angle-Tuning

The simultaneous phase-matching angle of parametric generation and SFG was experimentally determined to be  $\theta = 90^\circ$  and  $\phi = 30.1^\circ$  for the SF-OPO based on crystal-2. Figure 4.10 shows the sum-frequency energy at a fixed polarization rotation angle of  $28^\circ$  and signal energy at a polarization rotation angle of  $0^\circ$  (no SFG) as functions of the internal propagation angle  $\phi$  ( $\theta = 90^\circ$ ). An output coupler with a reflectivity of  $R = 85\%$  at the signal wavelength was used for mirror M2 in Fig. 4.1 for this measurement. The input pump energy was fixed at  $40 \pm 0.6$  mJ and the pump beam had a diameter of 2.2 mm ( $1/e^2$  intensity point), a divergence of 0.9 mrad, and pulse duration of 15.6 ns. The spatial profile of the pump beam was similar to the one shown in Fig. 3.2. It was possible to rotate the crystal a maximum of  $3.3^\circ$  (internal) from the point of normal incidence ( $\phi = 33^\circ$ ). The largest signal energy is obtained at the point of normal incidence, however, the sum-frequency energy peaks at the simultaneous phase-matching angle of  $\phi = 30.1^\circ$ .

Even with a  $R = 85\%$  output coupler for the signal where the 1064-nm-to-627-nm energy conversion efficiency is 8.6%, approximately 70% of the *s*-polarized signal component becomes depleted. Consequently, a stronger depletion for the *s*-polarized signal component can be expected for the case when M2 is a high

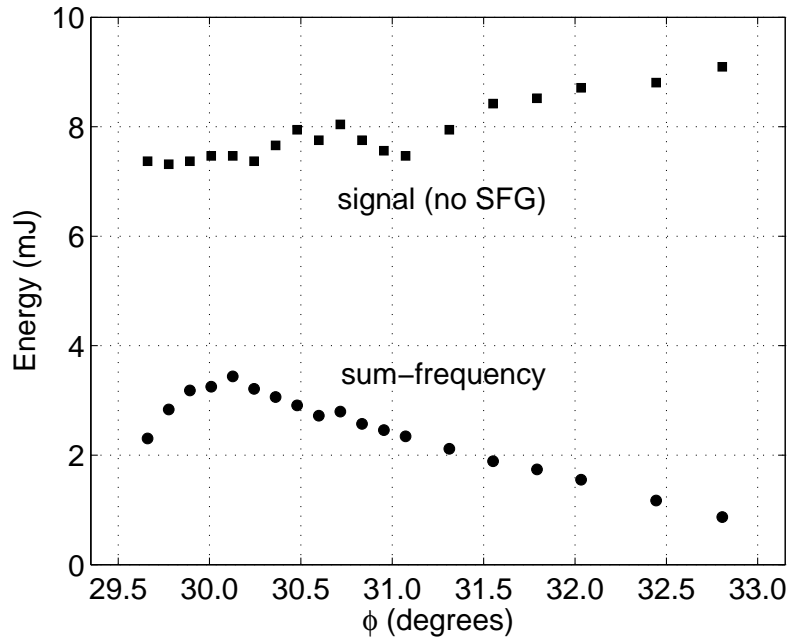


Figure 4.10: Signal energy at a polarization rotation angle of  $0^\circ$  (no SFG) and sum-frequency energy at a polarization rotation angle of  $28^\circ$  as functions of the propagation direction in  $x$ - $y$  plane of crystal-2 ( $\theta = 90^\circ$ ).

reflector at 1525 nm.

Inherently, it is not possible to angle-tune SF-OPOs when pumped by fixed wavelength lasers, since the simultaneous phase matching condition occurs at a single direction of propagation for a fixed pump wavelength. In our case, Fig. 4.10 shows that deviating from the simultaneous phase matching angle results in a rapid decrease of sum-frequency energy.

It is difficult to find a single set of Sellmeier coefficients that is accurate throughout the transparency range of a nonlinear crystal and valid for different  $\chi^{(2)}$  processes. This is even more so for KTA, for which there are several sets of quite different Sellmeier coefficients reported in the literature [122, 123, 129–131]. We determined which set to use for which process in an *ad hoc* fashion.

The simultaneous phase-matching angle determined experimentally is in excellent agreement with the value calculated using the Sellmeier coefficients given in Ref. [129] for parametric generation and those given in Ref. [131] for SFG.

Figure 4.11 shows the tuning curves of the signal wavelength calculated using the refractive index data given in Ref. [129] for parametric generation of the  $p$ -polarized signal from the  $p$ -polarized pump and refractive index data given in Ref. [131] for the sum-frequency generation process between the  $s$ -polarized signal and  $p$ -polarized pump. The intersection of the two curves occurs at  $\phi = 30.1^\circ$ , which is the simultaneous phase matching angle for these processes.

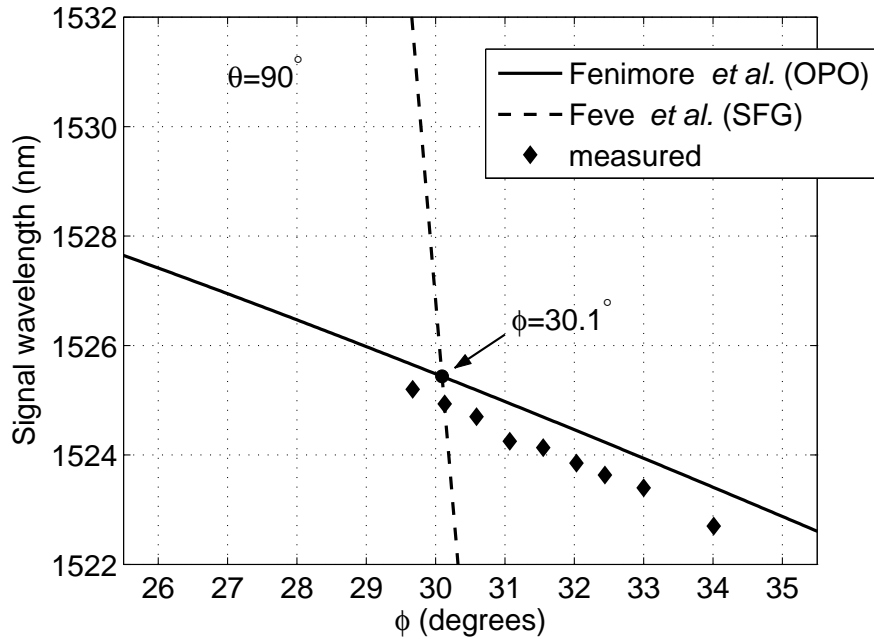


Figure 4.11: Tuning curves of the signal wavelength calculated using the refractive index data reported by Fenimore *et al.* [129] for parametric generation (signal is  $p$ -polarized) and refractive index data reported by Feve *et al.* [131] for SFG (signal is  $s$ -polarized). Measured signal wavelengths are also shown in the figure.

The Sellmeier coefficients given in Ref. [129] are more accurate than those given in Ref. [131] for calculating the wavelengths for parametric generation. Signal wavelengths measured for various values of  $\phi$  are also shown in Fig. 4.11. They are within  $\pm 0.7$  nm of those calculated using the Sellmeier coefficients given in Ref. [129]. However, using the Sellmeier coefficients given in Ref. [131] for parametric generation results in more than 6 nm difference between the calculated (not shown) and measured signal wavelengths.

We also conclude that the Sellmeier coefficients given in Ref. [131] are more

accurate than those given in Ref. [129] for calculating the wavelengths of SFG. If the Sellmeier coefficients given in Ref. [129] were used for both parametric generation and SFG, the simultaneous phase matching angle would be calculated to be  $\phi = 24^\circ$ , which is inconsistent with the experimental result.

### 4.3.7 Single-Pass Crystal-2 SF-OPO with Output Coupler

We also characterized the SF-OPO based on crystal-2 in terms of the sum-frequency energy as a function of the polarization rotation angle  $\alpha$  and input pump energy when an  $R = 85\%$  OC for the signal is used instead of the high reflector mirror M2 (Fig. 4.1).

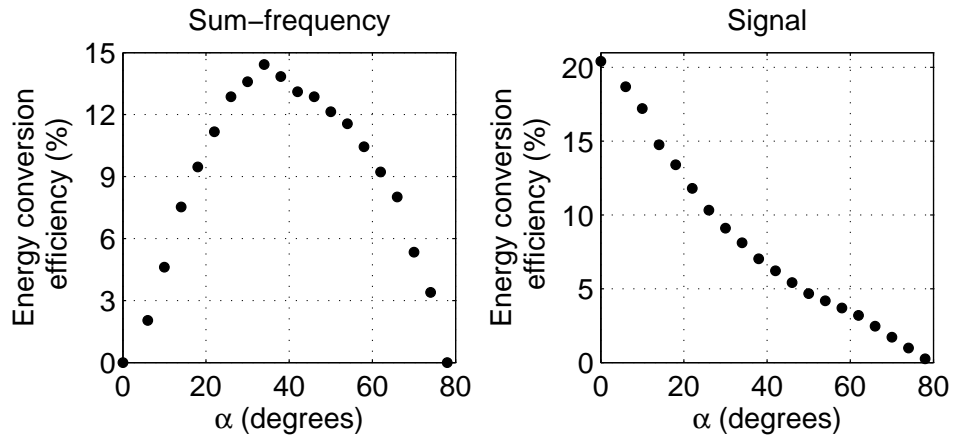


Figure 4.12: 1064-nm-to-627-nm and 1064-nm-to-1525-nm energy conversion efficiencies as functions of polarization rotation angle  $\alpha$  of the single-pass SF-OPO based on crystal-2 with the  $R = 85\%$  OC for the signal. Pump energy is held fixed at 38.9 mJ.

Figure 4.12 shows the 1064-nm-to-627-nm and 1064-nm-to-1525-nm energy conversion efficiencies as functions of the polarization rotation angle  $\alpha$  at a fixed pump energy of 38.9 mJ. A peak 1064-nm-to-627-nm conversion efficiency of 14.4% is obtained at an optimum polarization rotation angle of  $34^\circ$ . At  $\alpha = 34^\circ$  where the pump depletion is 33.9%, there is also a signal output and the 1064-nm-to-1525-nm energy conversion efficiency is 8.1%. At this point, the intracavity signal energy is estimated to be 21 mJ.

At  $\alpha = 0^\circ$ , there is no SFG, hence the largest output signal energy of 7.9 mJ is obtained at this point, corresponding to a 1064-nm-to-1525-nm energy conversion efficiency of 20.4%. Both the intracavity signal energy and pump depletion also attain their largest values of 53 mJ and 38.7%, respectively at this point. The output signal energy, intracavity signal energy and pump depletion all decrease monotonically as  $\alpha$  increases, due to the increasing total linear cavity loss experienced by the resonating  $p$ -polarized signal and the SF-OPO falls below threshold at  $\alpha = 78^\circ$ .

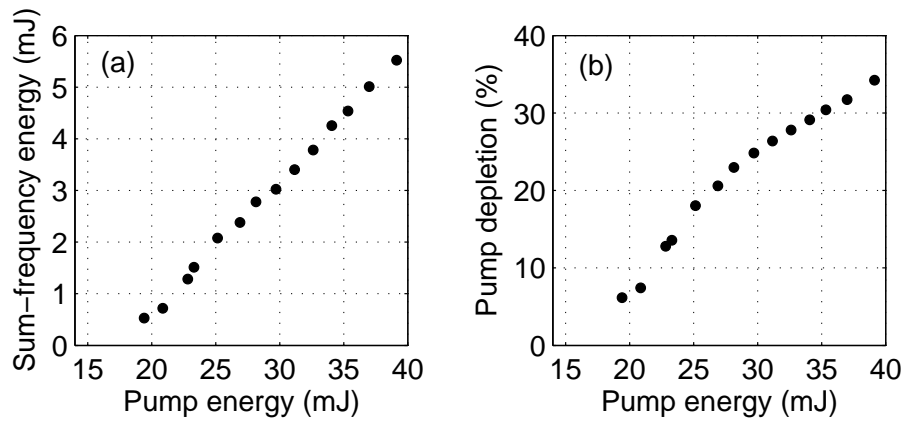


Figure 4.13: (a) Sum-frequency energy and (b) pump depletion as functions of input pump energy of the single-pass SF-OPO based on crystal-2 with the  $R = 85\%$  OC for the signal.  $\alpha$  is held fixed at  $34^\circ$ .

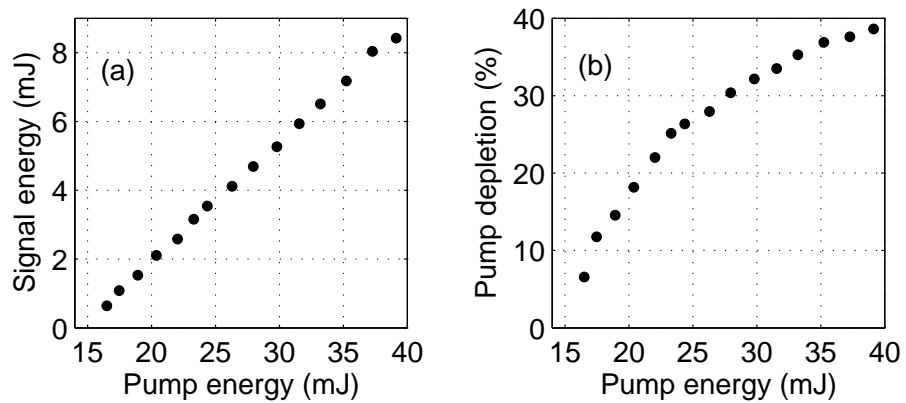


Figure 4.14: (a) Signal energy and (b) pump depletion as functions of input pump energy of the single-pass SF-OPO based on crystal-2 with the  $R = 85\%$  OC for the signal. There is no SFG, since  $\alpha$  is held fixed at  $0^\circ$ .

Figure 4.13 shows the output sum-frequency energy and pump depletion as functions of the pump energy while  $\alpha$  is held fixed at  $34^\circ$ . A maximum of 5.5 mJ sum-frequency energy is obtained at a pump energy of 39.1 mJ, corresponding to 14.1% conversion efficiency and 34.2% pump depletion. At this pump level, there is also a signal output of 3.3 mJ, corresponding to a 1064-nm-to-1525-nm energy conversion efficiency of 8.4%. The threshold energy of the SF-OPO is 17.7 mJ at this polarization rotation angle.

Figure 4.14 shows the output signal energy and pump depletion as functions of the pump energy while  $\alpha$  is held fixed at  $0^\circ$ . In this case, there is no SFG and the device merely operates as an OPO. The threshold energy is determined to be 14.6 mJ.

Figure 4.15 shows the spectra of the signal and sum-frequency beams obtained at the full input energy and optimum polarization rotation angle ( $\alpha = 34^\circ$ ). The signal and sum-frequency spectra peak at 1525.0 nm and 626.7 nm, respectively, and the corresponding bandwidths are approximately 0.5 nm and 0.2 nm. The pump spectrum is similar to the one shown in Fig. 4.8.

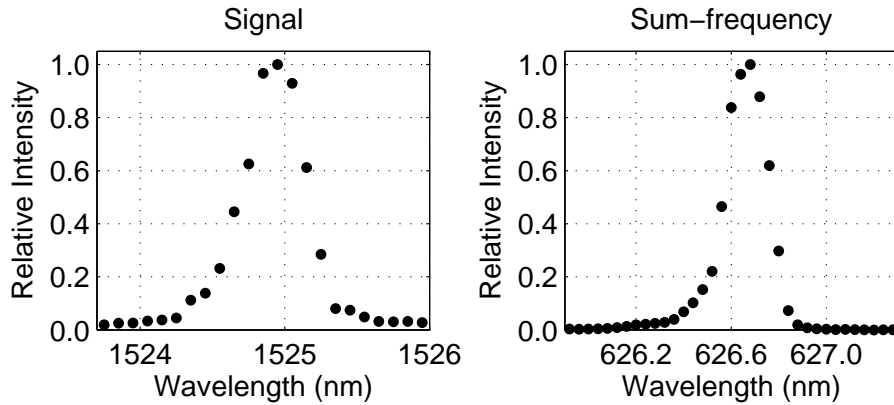


Figure 4.15: Spectra of the signal and sum-frequency beams of the single-pass SF-OPO based on crystal-2 with the  $R = 85\%$  OC for the signal.

At the full input energy and  $\alpha = 34^\circ$ , the sum-frequency and signal outputs have pulse durations (FWHM) of 9.4 ns and 11.0 ns, respectively. At the full input energy and  $\alpha = 0^\circ$ , the signal pulse duration is 14.0 ns which is longer than the previous case due to the reduced total cavity loss.

## 4.4 Results for the Double-Pass and Single-Pass SF-OPOs Based on Crystal-3

In this section, we present the experimental results for the double-pass and single-pass SF-OPOs based on crystal-3. We mainly focus on the double-pass configuration, however we also compare the experimental results for this configuration with the results that are available for the single-pass configuration. The double-pass device is characterized in terms of its output energy as functions of both the polarization rotation angle and the input pump energy, time profiles, spatial profiles, spectra of the beams, and the signal wavelengths generated by the device when the crystal is angle-tuned.

### 4.4.1 Output Energy versus Polarization Rotation Angle

We first determined the polarization rotation angle  $\alpha$  which maximizes the output sum-frequency energy at the maximum input pump energy of the double-pass crystal-3 SF-OPO. Figure 4.16 shows the 1064-nm-to-627-nm energy conversion efficiency and relative intracavity signal energy as functions of  $\alpha$  at a fixed pump energy of 20.4 mJ. A peak conversion efficiency of 28.7% is obtained at an optimum polarization rotation angle of  $36^\circ$ . At this rotation angle, the intracavity signal energy is 33 mJ. The smallest  $\alpha$  is chosen to be  $22^\circ$  to avoid damage to the KTA crystal. At this rotation angle, the energy conversion efficiency is 25.2% and the intracavity signal energy has a maximum value of 45 mJ. The intracavity signal energy decreases monotonically as  $\alpha$  increases, due to the increasing total linear cavity loss experienced by the resonating  $p$ -polarized signal. The SF-OPO falls below threshold at  $\alpha = 90^\circ$ . In the double-pass configuration, the pump depletion could not be measured since the incident and return pump beams almost overlap each other.

Similarly, for the single-pass crystal-3 SF-OPO, the optimum polarization rotation angle which maximizes the output sum-frequency energy at an input

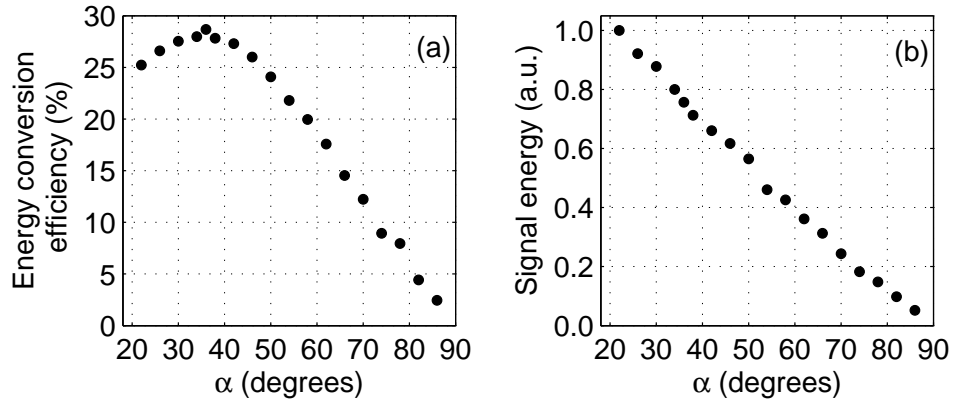


Figure 4.16: (a) Energy conversion efficiency and (b) relative intracavity signal energy as functions of  $\alpha$  of the double-pass SF-OPO based on crystal-3. Pump energy is held fixed at 20.4 mJ.

pump energy of 30.3 mJ is determined to be  $38^\circ$ . At  $\alpha = 38^\circ$ , the 1064-nm-to-627-nm energy conversion efficiency is 19% and the pump depletion is 30%. The residual cavity loss is calculated to be approximately 2.5%, which is also valid for the double-pass configuration.

#### 4.4.2 Output Energy versus Input Energy

Figure 4.17 shows the output sum-frequency energy as a function of the input pump energy for both double-pass and single-pass configurations. The pump depletion as a function of the pump energy is only shown for the single-pass configuration. The rotation angle  $\alpha$  is held fixed at the previously determined optimum values of  $36^\circ$  and  $38^\circ$  for the double-pass and single-pass configurations, respectively.

For the double-pass configuration, a maximum of 5.8 mJ sum-frequency energy is obtained at a pump energy of 20.3 mJ, corresponding to 28.4% conversion efficiency. The threshold energy of the double-pass SF-OPO is 7.7 mJ. For the single-pass configuration, again a maximum of 5.8 mJ sum-frequency energy is obtained at a pump energy of 30.3 mJ, corresponding to 19.1% conversion efficiency and 30% pump depletion. The threshold energy of the single-pass SF-OPO

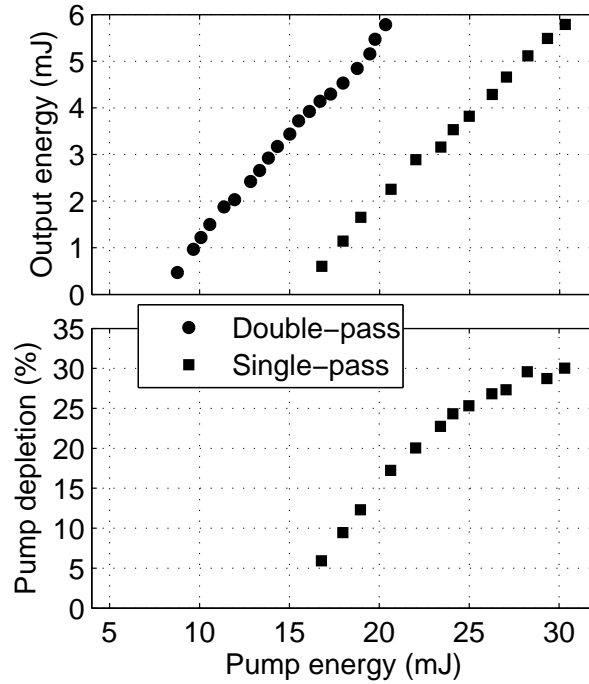


Figure 4.17: Output energies as functions of input pump energy of the double-pass and single-pass SF-OPOs based on crystal-3. Pump depletion as a function of pump energy of the single-pass SF-OPO is also shown.  $\alpha$  is held fixed at  $36^\circ$  and  $38^\circ$  for the double-pass and single-pass SF-OPOs, respectively.

is 15 mJ. We note that the threshold energy of the double-pass SF-OPO is almost half of that of the single-pass SF-OPO and a remarkably larger energy conversion efficiency is achieved using the double-pass configuration.

Similar to the single-pass crystal-2 SF-OPO, for any input pump level, the output sum-frequency energy of the double-pass crystal-3 SF-OPO can easily be maximized by adjusting the polarization rotation angle. Figure 4.18 shows the maximum energy conversion efficiency and the optimum polarization rotation angle as functions of the input pump energy for the double-pass configuration. The optimum polarization rotation angle decreases monotonically with decreasing pump energy.

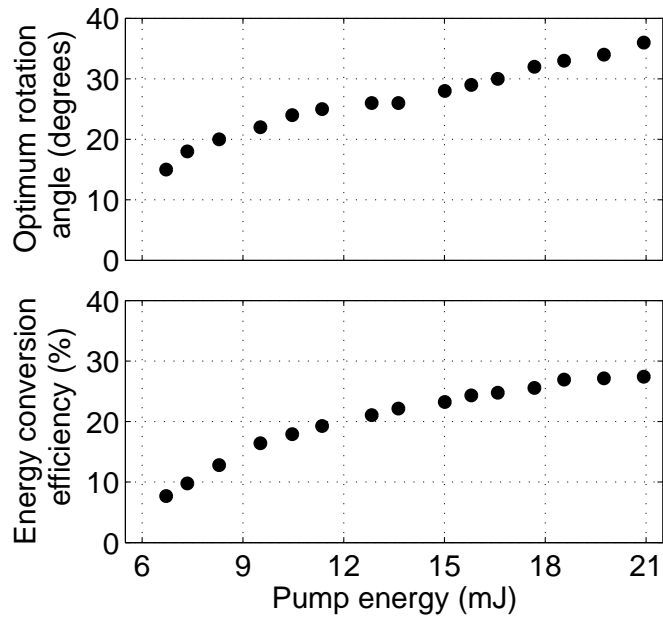


Figure 4.18: Optimum polarization rotation angle and maximum energy conversion efficiency as functions of pump energy of the double-pass crystal-3 SF-OPO.

### 4.4.3 Time Profiles

Figure 4.19 shows the time profiles of the pump and sum-frequency pulses of both double-pass and single-pass SF-OPOs based on crystal-3. The sum-frequency pulse profile for each configuration is obtained at the full input energy (20.4 mJ and 30.3 mJ, for double-pass and single-pass, respectively) and at the optimum polarization rotation angle for the particular configuration. The pump pulse duration (FWHM) for both cases is 17.8 ns. The pulse durations of the sum-frequency beam are 14.2 ns and 12.5 ns for the double-pass and single-pass configurations, respectively. For the double-pass configuration, higher energy conversion efficiency results in a broader sum-frequency pulse.

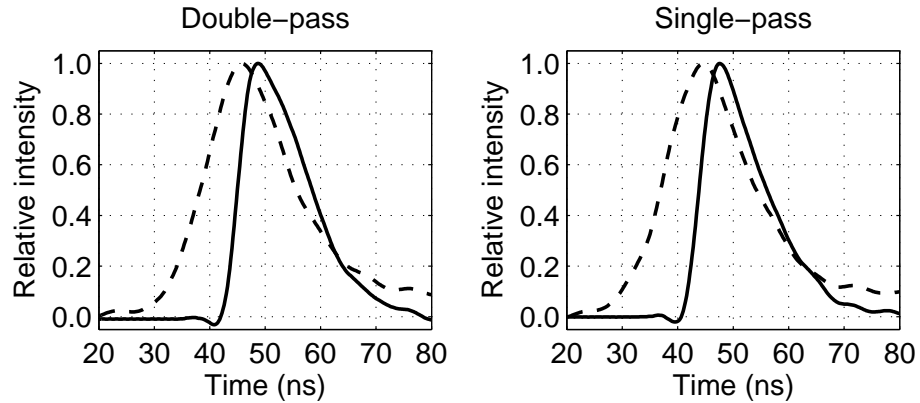


Figure 4.19: Time profiles of the pump (dashed curves) and sum-frequency (solid curves) pulses of the double-pass and single-pass SF-OPOs.

#### 4.4.4 Spectrum of the Sum-Frequency

The bandwidth of the pump beam is approximately 0.2 nm. Figure 4.20 shows the spectra of the sum-frequency output measured at full energy for the double-pass and single-pass configurations with the corresponding bandwidths of 0.16 nm and 0.2 nm, respectively. The spectral shift in the peak location observed for the double-pass configuration ( $\sim 0.04$  nm) is due to a shift in the signal wavelength resulting from the slight tilt between the propagation axes of the incident and return pump beams.

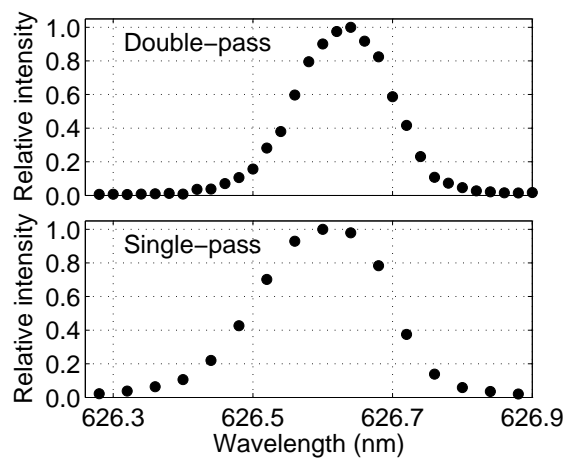


Figure 4.20: Spectra of the sum-frequency beam for the double-pass and single-pass configurations.

#### 4.4.5 Spatial Profiles of the Sum-Frequency Beam

Figure 4.21 shows the spatial profiles of the sum-frequency beam of the double-pass crystal-3 SF-OPO obtained at 56 cm and 96 cm away from the input face of the crystal. These profiles are measured at the full input energy and optimum polarization rotation angle. The divergence of the beam is 1.9 mrad (full-angle), which is similar to that of the single-pass SF-OPO based on crystal-2. The beam diameter ( $1/e^2$  intensity point) at the exit face of the crystal is about 1.9 mm and the beam has a peak intensity of  $40 \text{ MW/cm}^2$  at this point.

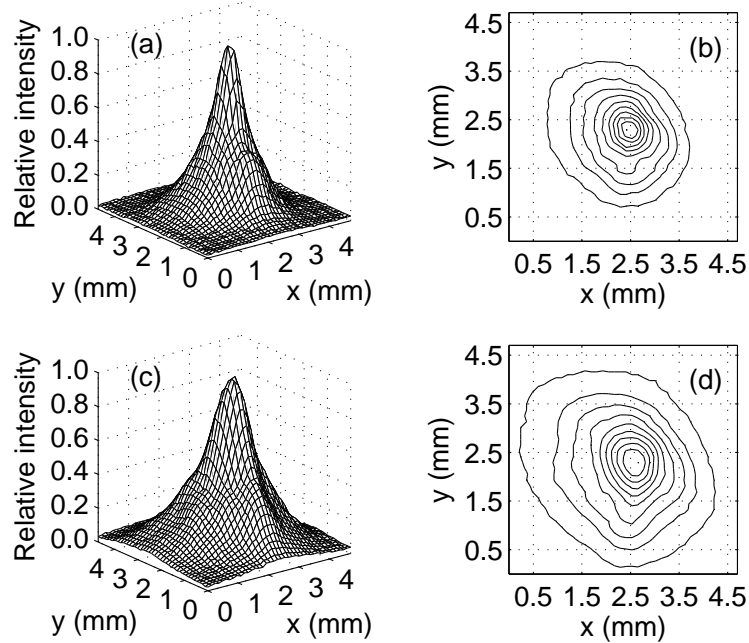


Figure 4.21: 3-D plots for the spatial profiles of the sum-frequency beam at (a) 56 cm and (c) 96 cm away from the input face of the crystal. The corresponding contour plots are shown in (b) and (d).

#### 4.4.6 Simultaneous Phase-Matching Angle and Signal Wavelengths with Angle-Tuning

For the SF-OPO based on crystal-3, the simultaneous phase matching angle for parametric generation and SFG was experimentally determined to be  $\theta = 90^\circ$

and  $\phi = 30.8^\circ$ , which is the angle that maximizes the 1064-nm-to-627-nm energy conversion efficiency. This angle is quite close to the predicted value of  $\theta = 90^\circ$  and  $\phi = 30.1^\circ$  using the Sellmeier coefficients given in Ref. [129] for parametric generation and those given in Ref. [131] for SFG.

Figure 4.22 shows the signal wavelengths measured for various values of angle  $\phi$  ( $\theta = 90^\circ$ ) for the single-pass SF-OPO based on crystal-3. An output coupler that has a reflectivity of 85% at the signal wavelength was used for this measurement. Tuning curves of the signal wavelength calculated using the refractive index data given in Ref. [129] for parametric generation and refractive index data given in Ref. [131] for SFG are also shown in Fig. 4.22. Measured signal wavelengths are within  $\pm 0.5$  nm of those calculated using the Sellmeier coefficients given in Ref. [129].

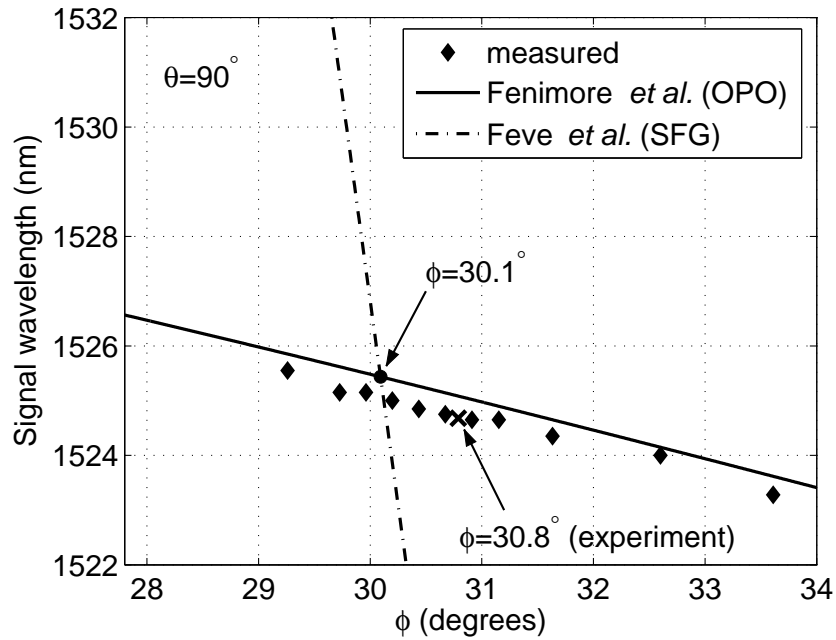


Figure 4.22: Signal wavelengths measured for various values of  $\phi$  for the single-pass crystal-3 SF-OPO with the  $R = 85\%$  OC. Tuning curves of the signal wavelength calculated using the refractive index data reported by Fenimore *et al.* [129] for parametric generation (signal is  $p$ -polarized) and refractive index data reported by Feve *et al.* [131] for SFG (signal is  $s$ -polarized) are also shown. Points corresponding to the predicted and experimentally determined simultaneous phase-matching angles are indicated in the figure.

## 4.5 Numerical Modelling

Our work on nanosecond OPOs is purely experimental. However, the description and results of a numerical model for a nanosecond SF-OPO which was reported in Ref. [104] are also presented here for the sake of completeness. We first review the previous work that was done for modelling nanosecond OPOs. Next, we briefly describe the numerical model reported in Ref. [104]. Finally, predictions of the model and experimental results are compared.

### 4.5.1 Models for Nanosecond OPOs

Because nanosecond OPOs operate in the transient regime, models developed for cw OPOs cannot accurately predict their behavior and a dynamic model is necessary [137]. Brosnan and Byer *et al.* [132] used analytical expressions for predicting the threshold intensity of a nanosecond OPO. Using the assumption of low pump depletion, two other models [139,140] added optical cavity modes and crystal birefringence to this analysis. However, the assumption of low pump depletion is not valid even for pump energy levels slightly higher than threshold energies, therefore these models are only accurate for predicting the threshold energies or intensities. A nanosecond OPO model based on numerical integration of the frequency-mixing equations for plane-waves was proposed [141]. This model was used for modelling a linear-cavity OPO based on KTP. Although good agreement with the experimental results was achieved by adjusting the nonlinear coefficient  $d_{\text{eff}}$ , the model is inaccurate since diffraction is neglected. Another numerical model proposed by Smith *et al.* [142] includes all the relevant physics such as diffraction, birefringent walk-off, and pump depletion for a seeded, nanosecond OPO pumped by a single-frequency pump laser. The predictions of the model were shown to agree quite well with the observed performance of a KTP ring OPO. The primary limitation of this model is its assumption of narrow-bandwidth operation, which is valid for injection-seeded, single-longitudinal-mode devices pumped by single-longitudinal-mode pulses. Urschel *et al.* [143] used the model described in Ref. [142] for the numerical simulation of the spatio-temporal dynamics of the pulse formation in

nanosecond OPOs. This method successfully predicted the temporal evolution of the beam quality factor  $M^2$  during the signal pulse formation of a nanosecond OPO based on BBO [144].

Most nanosecond OPOs reported in the literature use linear cavities due to their simple design and are pumped by multimode laser sources. These OPOs exhibit multimode or broad-bandwidth operation. Several theoretical treatments of multimode OPOs were published [133, 145–149]. The models in Refs. [145–147], which are based on an early theory of OPOs by Yariv *et al.* [150], provide a rate-equation-based approach. These models make use of the assumption of spatially uniform fields which is invalid for nanosecond OPOs, since even the resonated signal is nonuniform in these devices due to the relatively high output coupling. Furthermore, these models neglect the group-velocity terms in the coupled mode-equations, and hence they provide a poor description for multimode OPOs. Another model which allows for nonuniform fields but neglects group-velocity differences of the waves was reported [148]. More realistic models described in Refs. [133, 149] allow for different group velocities of the waves, however incorporating diffraction and birefringent walk-off into these models results in a prohibitively large computational cost.

### 4.5.2 Numerical Model for the SF-OPO

The steady-state plane-wave analysis of SF-OPOs was previously reported [59]. However, nanosecond SF-OPOs operate in the transient regime, hence the temporal evolution of the waves should be taken into account. A numerical model for nanosecond SF-OPOs was reported in Ref. [104]. This model follows the procedure outlined in [142] with the coupled-mode equations being modified to include the equations for the simultaneous SFG.

Similar to the model for OPOs described in [142], this numerical model for nanosecond SF-OPOs assumes narrow-bandwidth operation. However, our SF-OPO produces multimode or broad-bandwidth output due to the facts that our pump laser is not injection-seeded, we did not use spatial filtering or any other

methods to obtain a pure Gaussian pump beam, our SF-OPO is not injection-seeded and it uses a standing-wave cavity. Nevertheless, there is qualitative agreement between the predictions of the model for monochromatic waves and experimental results.

In this model, a Gaussian pulse fitted to the temporal profile of the pump laser is discretized with a series of time slices separated by the round-trip time for the SF-OPO cavity. The time integrated transverse profile of the pump beam measured at the input face of the crystal by a CCD camera is also discretized with a spatial grid. Since the divergence of the pump beam is relatively low, the phase-front of the input pump beam is assumed to be flat at the input face of the crystal. For each time slice, the spatial profile of the pump is propagated along the nonlinear crystal after proper scaling for calculating the input intensity of the pump beam at each spatial grid location is performed. Propagation of the pump and other waves in the nonlinear crystal and in free space are handled using the Fourier transforms of the fields in the transverse dimension. For each time slice, the phases and amplitudes of the depleted pump,  $p$ -polarized and  $s$ -polarized signal, idler and sum-frequency fields over their transverse profiles are calculated at discrete locations along the propagation direction. The  $p$ -polarized signal spatial profile is updated at the input face of the crystal after a propagation around the cavity with the residual (or useless) cavity loss and loss due to coupling into the  $s$ -polarized signal taken into account. This procedure is repeated for the duration of the pump pulse. It is assumed that the cavity is purely singly-resonant for the signal. The idler and sum-frequency beams at the crystal input surface are assumed to be nonexistent and residual reflections of all beams from optical surfaces are neglected. The  $s$ -polarized signal is assumed to be completely depleted by SFG following a pass through the nonlinear crystal in the forward-propagation direction.

For each time slice in the temporal profile of the pump, the coupled-mode equations that describe the simultaneously-phase-matched parametric generation and SFG processes in the nonlinear crystal of a class-D SF-OPO can be written

as [59, 142]

$$\frac{\partial A_1}{\partial z} = \frac{-j}{2k_1} \left( \frac{\partial^2}{\partial x^2} + \frac{\partial^2}{\partial y^2} \right) A_1 - j \frac{\omega_1 d_{ea}}{n_1 c} A_3 A_2^*, \quad (4.1)$$

$$\frac{\partial A_2}{\partial z} = \frac{-j}{2k_2} \left( \frac{\partial^2}{\partial x^2} + \frac{\partial^2}{\partial y^2} \right) A_2 - j \frac{\omega_2 d_{ea}}{n_2 c} A_3 A_1^*, \quad (4.2)$$

$$\frac{\partial A_3}{\partial z} = \frac{-j}{2k_3} \left( \frac{\partial^2}{\partial x^2} + \frac{\partial^2}{\partial y^2} \right) A_3 - j \frac{\omega_3 d_{ea}}{n_3 c} A_1 A_2 - j \frac{\omega_3 d_{eb}}{n_3 c} A_6 A_4^*, \quad (4.3)$$

$$\frac{\partial A_4}{\partial z} = \frac{-j}{2k_4} \left( \frac{\partial^2}{\partial x^2} + \frac{\partial^2}{\partial y^2} \right) A_4 - j \frac{\omega_4 d_{eb}}{n_4 c} A_6 A_3^*, \quad (4.4)$$

$$\frac{\partial A_6}{\partial z} = \frac{-j}{2k_6} \left( \frac{\partial^2}{\partial x^2} + \frac{\partial^2}{\partial y^2} \right) A_6 - j \frac{\omega_6 d_{eb}}{n_6 c} A_3 A_4, \quad (4.5)$$

where  $A_m$  represent the complex field amplitudes of the optical electric field

$$E_m(x, y, z, t) = \text{Re} \{ A_m(x, y, z, t) \exp[j(\omega_m t - k_m z)] \} \quad (4.6)$$

and  $m = 1, 2, 3, 4, 6$  index the fields idler, signal, pump, rotated signal and sum-frequency, respectively. In the equations above,  $d_{ea}$  and  $d_{eb}$  are the effective nonlinear coefficients for parametric generation and SFG, respectively. Diffraction terms are included, however beam walk-off terms are neglected since walk-off angles of the  $p$ -polarized beams are relatively small. Transmission losses experienced by the fields at the wavelengths of interest in KTA are negligible, hence not included.

Fourier transforming Equations (4.1)–(4.5) into the spatial-frequency domain results in

$$\frac{\partial \tilde{A}_1}{\partial z} = \frac{j2\pi^2}{k_1} (\nu_x^2 + \nu_y^2) \tilde{A}_1 - j \frac{\omega_1 d_{ea}}{n_1 c} \mathcal{F}(A_3 A_2^*), \quad (4.7)$$

$$\frac{\partial \tilde{A}_2}{\partial z} = \frac{j2\pi^2}{k_2} (\nu_x^2 + \nu_y^2) \tilde{A}_2 - j \frac{\omega_2 d_{ea}}{n_2 c} \mathcal{F}(A_3 A_1^*), \quad (4.8)$$

$$\frac{\partial \tilde{A}_3}{\partial z} = \frac{j2\pi^2}{k_3} (\nu_x^2 + \nu_y^2) \tilde{A}_3 - j \frac{\omega_3 d_{ea}}{n_3 c} \mathcal{F}(A_1 A_2) - j \frac{\omega_3 d_{eb}}{n_3 c} \mathcal{F}(A_6 A_4^*), \quad (4.9)$$

$$\frac{\partial \tilde{A}_4}{\partial z} = \frac{j2\pi^2}{k_4} (\nu_x^2 + \nu_y^2) \tilde{A}_4 - j \frac{\omega_4 d_{eb}}{n_4 c} \mathcal{F}(A_6 A_3^*), \quad (4.10)$$

$$\frac{\partial \tilde{A}_6}{\partial z} = \frac{j2\pi^2}{k_6} (\nu_x^2 + \nu_y^2) \tilde{A}_6 - j \frac{\omega_6 d_{eb}}{n_6 c} \mathcal{F}(A_3 A_4), \quad (4.11)$$

where  $\nu_x$  and  $\nu_y$  are the spatial frequencies in  $x$  and  $y$  directions, respectively,  $\tilde{A}_m(\nu_x, \nu_y, z, t)$  ( $m = 1, 2, 3, 4, 6$ ) are the Fourier transforms of the complex field

amplitudes, and  $\mathcal{F}$  Fourier-transforms a function  $f(x, y, z, t)$  in the transverse dimension by calculating

$$\iint_{-\infty}^{\infty} f(x, y, z, t) \exp[-j2\pi(\nu_x x + \nu_y y)] dx dy. \quad (4.12)$$

Equations (4.7)–(4.11) are integrated using the Runge-Kutta algorithm [151]. At the beginning of each  $z$  step,  $\tilde{A}_m(\nu_x, \nu_y, z, t)$  terms are inverse Fourier transformed to obtain  $A_m(x, y, z, t)$  and the arguments of the Fourier transform function  $\mathcal{F}$  in (4.7)–(4.11) are calculated.

In the double-pass configuration, the pump is reflected back into the cavity by M4. For the return pass, phase-matched parametric generation still occurs through the interaction of the reflected pump and resonating  $p$ -polarized signal, however there is no SFG under the assumption that  $s$ -polarized signal becomes completely depleted in the forward pass through the crystal. Equations (4.7)–(4.9) without the term due to SFG (the last term in Equation (4.9)) are integrated in the return pass to account for parametric generation. The idler is again assumed to be nonexistent at the starting location of the interaction (exit face of the crystal). For the return pass of the single-pass configuration, it is assumed that no nonlinear interaction occurs between the waves.

On the return pass, as the  $p$ -polarized signal makes a double-pass through the  $\lambda/4$  plate and its polarization is rotated by an angle of  $\alpha$ , hence the updated complex field amplitudes of the  $p$ - and  $s$ -polarized components after rotation are given by

$$A'_2 = A_2 \cos \alpha \quad \text{and} \quad A'_4 = A_2 \sin \alpha. \quad (4.13)$$

The Gaussian pulse fitted to the time profile of the pump laser which has a 17.8 ns pulse duration (FWHM) is discretized with 130 time slices each with a duration of the cavity round trip time of our SF-OPO which is 423 ps. The transverse spatial grid is typically  $32 \times 32$  or  $64 \times 64$  covering a computation area of  $4.7 \times 4.7$  mm, which is the active CCD array size. When the output energy values calculated using a  $128 \times 128$  grid are compared with those obtained using  $32 \times 32$  and  $64 \times 64$  grids, there are typically differences of 4% and 1%, respectively, between the results.

Even when there is no polarization rotation ( $\alpha = 0$ ),  $p$ -polarized signal intensity (or energy) experiences a residual cavity loss. In the model, this loss is chosen to be the same with the experimentally determined value of 2.5%. Values that are used for the effective nonlinear coefficients  $d_{ea}$  and  $d_{eb}$  are 2.9 pm/V and 3.2 pm/V, respectively. These values are calculated using the recently published data for the nonlinear tensor of KTA [127] with the correction due to walk-off included and the dispersion in the nonlinear coefficients taken into account by employing Miller's rule [128]. For this calculation, the Sellmeier coefficients given in Ref. [129] and Ref. [131] are used for parametric generation and SFG, respectively, at the simultaneous phase matching angle of  $\theta = 90^\circ$  and  $\phi = 30.1^\circ$ .

A seed power of 1 nW is used for the signal in the model calculations. This value represents the spontaneous parametric fluorescence for the value of the pump power at the first time slice of the time profile [152]. However, this value can be much larger than the true parametric fluorescence coupled into a cavity mode which initiates the oscillation. It was also observed that the model calculations are weakly dependent on the choice of the signal seed power. For instance, decreasing the seed power by 3 and 6 orders of magnitude resulted in calculated values of the 1064-nm-to-627-nm energy conversion efficiency that are lower than the value for 1 nW seed power by 1.2% and 2.4%, respectively. This comparison was done for the double-pass SF-OPO operated at full input energy and optimum  $\alpha$ .

### 4.5.3 Predictions of the Model and Discussion

Figure 4.23 shows the predictions of the model for the 1064-nm-to-627-nm energy conversion efficiency as a function of the polarization rotation angle  $\alpha$  at a fixed pump energy of 20.4 mJ for the double-pass configuration. The experimental results are also shown in the same figure. The model predicts a peak conversion efficiency of 37.2% calculated at the optimum rotation angle  $\alpha = 30.3^\circ$ , whereas the experimental results for the maximum conversion efficiency and optimum  $\alpha$  are 28.7% and  $36^\circ$ , respectively.

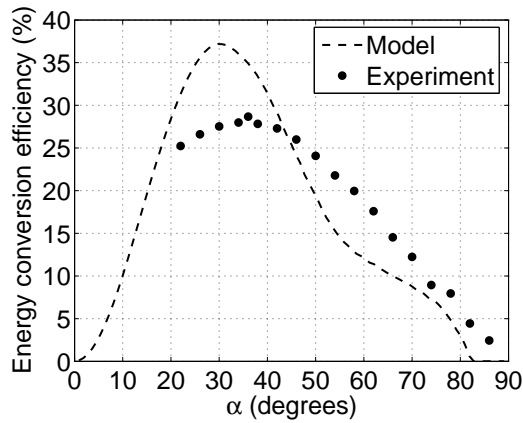


Figure 4.23: Calculated and measured energy conversion efficiency as a function of  $\alpha$  for the double-pass configuration. Pump energy is held fixed at 20.4 mJ.

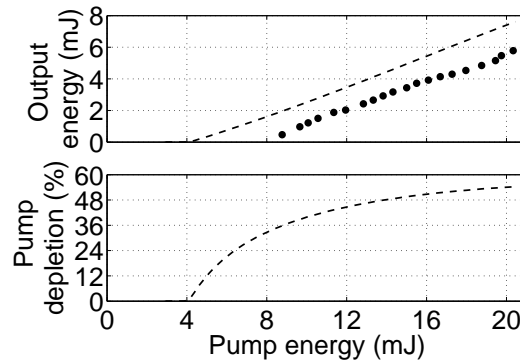


Figure 4.24: Calculated (dashed lines) and measured (filled circles) for the output sum-frequency energy as a function of pump energy for the double-pass configuration. Pump depletion predicted by the model is also shown.  $\alpha = 30.3^\circ$  and  $\alpha = 36^\circ$  for the model calculation and experiment, respectively.

Figure 4.24 shows the results of the model for the output energy as a function of the pump energy calculated at  $\alpha = 30.3^\circ$  along with the experimental results. The model predicts a maximum output energy of 7.6 mJ obtained at the maximum pump energy used in the experiment, which is 20.3 mJ, whereas in the experiment a maximum output energy of 5.8 mJ was obtained at this pump level. The model predicts a pump depletion of 54.2% at the same pump level. The predicted threshold energy is only 4.2 mJ.

Figure 4.25 shows the temporal profiles of the sum-frequency pulse predicted

by the model and obtained in the experiment. Both profiles are for the maximum input energy and the corresponding optimum  $\alpha$ . The model predicts a pulse duration (FWHM) of 15.8 ns, whereas 14.2 ns is the value measured in the experiment.

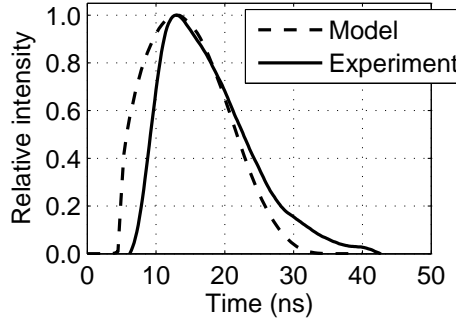


Figure 4.25: Calculated and measured time profile of the sum-frequency pulse for the double-pass configuration.

There are several factors that result in discrepancies between the model calculations and experimental results. Similar to the case for unseeded OPOs [142], this model predicts generally higher conversion efficiencies than the ones obtained in the experiment. This is to be expected since the model is for waves of monochromatic nature, hence for narrow-bandwidth operation. Also, an upper limit for the signal seed power was used in the model calculations. Furthermore, in the model, no attempt to fit the predictions of the model to the data was made by adjusting any one of the physical parameters. For instance, the results are strongly dependent on the value of the effective nonlinear coefficients of the nonlinear processes  $d_{ea}$  and  $d_{eb}$ . The values used in the model calculations were derived from those reported literature using Miller's scaling, which is only an approximation for taking the wavelength dependence of the effective nonlinear coefficient into account. It was observed that even a few percent change in one of these coefficients may result in up to 10% change in the energy of the resultant sum-frequency pulse. Nevertheless, the model is the first model reported for SF-OPOs operating in the nanosecond regime and is in qualitative agreement with the experimental results.

## 4.6 Summary

In this chapter, we experimentally characterized nanosecond SF-OPOs that employ a single KTA crystal for both parametric generation and SFG. Two KTA crystals with slightly different cut angles are used in these experiments. The SF-OPOs are pumped by a  $Q$ -switched Nd:YAG laser operating at 1064 nm.

The SF-OPO based on crystal-2 is the first demonstration of a nanosecond upconversion OPO using simultaneous phase matching. This device generates 627 nm pulses with a pulse-width of 10.4 ns and with a pulse energy of 8.3 mJ, corresponding to a 1064-nm-to-627-nm energy conversion efficiency of 21%, when pumped in a single-pass configuration. The device is characterized in terms of its energy output as functions of polarization rotation angle and input pump energy. Time profiles, spatial beam profiles and spectra of the output are also given. The simultaneous phase matching characteristics of the device is described. Similar characterization is also presented when the output mirror of the device is a partially transmitting mirror at the signal wavelength.

The SF-OPO based on crystal-3 is pumped in both single-pass and double-pass configurations. The double-pass SF-OPO based on crystal-3 generates 627 nm output pulses with a pulse-width of 14.2 ns and with a pulse energy of 5.8 mJ, corresponding to a 1064-nm-to-627-nm energy conversion efficiency of 29%. This device is characterized in terms of its energy output as functions of polarization rotation angle and input pump energy, time profiles, spatial beam profiles and spectra of the output. These results are compared with a similar characterization performed for the single-pass SF-OPO based on the same crystal. The double-pass pumping scheme proves to be useful for increasing the energy conversion efficiency. The simultaneous phase matching characteristics of the SF-OPO based on crystal-3 is shown to be similar to that of the SF-OPO based on crystal-2.

Finally, previous models developed for nanosecond OPOs are reviewed and a numerical model for nanosecond OPOs is described. The model calculations are compared with the experimental results for the double-pass SF-OPO. The model is in qualitative agreement with the experiment.

## Chapter 5

# Plane-Wave Modelling of Continuous-Wave Intracavity Optical Parametric Oscillators

An intracavity optical parametric oscillator (IOPO) is formed by constructing an OPO inside a laser cavity. Owing to high intracavity laser intensities, these oscillators have been extensively used for generating tunable near- to mid-infrared radiation with higher power conversion efficiencies compared to the externally pumped OPOs, especially in the continuous-wave regime. In recent years, several experimental demonstrations of such devices operating in cw [153–163] and pulsed [119, 137, 164–179] regimes have been made. In particular, cw operation of singly resonant IOPOs based on the birefringent nonlinear materials KTP [154] and KTA [156] and the quasi-phase-matched nonlinear materials periodically poled LiNbO<sub>3</sub> [155, 158, 159, 162, 163], RbTiOAsO<sub>4</sub> [157, 161, 163], and KTP [160], pumped internally by argon-ion-laser-pumped Ti:sapphire lasers [154–157, 160] or diode-pumped Nd:YVO<sub>4</sub> lasers [158, 159, 161–163] was demonstrated.

The first theoretical model for a cw doubly-resonant IOPO for which both the signal and idler fields are assumed to be resonant in the OPO cavity was developed back in early 1970's [180]. This model used a plane-wave analysis with a

constant resonant field approximation (no spatial variation along the propagation axis for the laser, signal and idler fields) and a small-signal model for the laser. Another model extended this theory to include the temporal variation of the laser population inversion in an attempt to explain the dynamics of doubly-resonant IOPOs operating in the pulsed regime [181]. A more recent model treated the dynamics of pulsed IOPOs for which only the signal field is resonant in the OPO cavity [182]. This model neglected both the time dependence of the idler field and the spatial variation of the resonant fields (laser and signal) along the propagation axis, however took the spatial variation of the nonresonant idler and time variation of the resonant fields into account. A later model extended this previous model to include a multi-frequency intracavity laser field and provided methods to optimize the signal and idler outputs for cw singly-resonant IOPOs [183]. Another approach for numerical calculation of the temporal profile of the laser and signal pulses inside a pulsed singly-resonant IOPO was recently proposed [171]. Unlike the previous models, this model accounted for the spatial variation of the resonant fields (laser and signal) in the propagation direction in the nonlinear crystal along with the spatial variation of the nonresonant idler. A similar model further included the temporal variation of the phase of the intracavity laser field [184].

Here, we present a model for end-pumped cw singly-resonant IOPOs. We employ plane-waves in our model and assume that there is perfect phase-matching and no walk-off in the nonlinear crystal. We account for the spatial variation of the intracavity laser field along the propagation axis in the laser crystal and the spatial variations of the intracavity laser (or the OPO pump), signal and idler fields along the same axis in the nonlinear crystal. When compared to the previous model [183] for the cw IOPOs, our model is expected to yield more accurate results at high pump levels and/or for long OPO crystals with high nonlinearities.

In our model, we use the pertinent laser and OPA equations describing the variation of the field amplitudes along the axis of propagation and iteratively solve them employing an approach similar to the one used by Aytür *et al.* [58] and Dikmelik *et al.* [59] to obtain a self-consistent solution for these amplitudes in

the laser and OPO cavities. We further determine the useful loss of the optimum output coupler (OC) of the OPO cavity for the generation of the highest photon conversion efficiency corresponding to the signal or the idler. We only consider the travelling-wave IOPOs in our model, however our method can readily be extended to a model for the standing-wave IOPOs.

Continuous-wave singly-resonant IOPOs based on Ti:sapphire as the laser crystal [154–157, 160] provide the advantage of tuning the intracavity laser field or the OPO pump over a wide range of frequencies. In this work, we chose to apply our method for singly-resonant IOPOs internal to the cavity of a Ti:sapphire laser end-pumped by an argon-ion laser.

We first present the device configuration of a travelling-wave IOPO and the assumptions of the model. Next, we present the laser model. The coupled-mode equations for the OPA and their solutions have been already given in Section 2.6 of Chapter 2, hence will not be repeated. Subsequently, we combine the equations for the laser and the OPA to obtain the single-pass description of the cw travelling-wave IOPO and describe the numerical procedure for solving these equations. Finally, we present the results of our model.

## 5.1 Device Configuration, Operation and Model Assumptions

Figure 5.1 shows the schematic arrangement of the travelling-wave IOPO. The device is comprised of a laser crystal of length  $l_l$ , a nonlinear crystal of length  $l_n$ , and a Faraday isolator. A cw external laser longitudinally pumps the laser crystal through mirror M1 and the resultant intracavity laser field, or OPO pump, pumps the nonlinear crystal. The Faraday oscillator ensures that both the laser and the parametric oscillations are unidirectional. The laser and OPO cavities are formed by mirrors M1 through M4 and M3 through M6, respectively. M1 and M2 are coated for high transmission at the external pump laser wavelength and for high reflection at the laser wavelength. M3 is coated for high reflection at both the

laser and the signal wavelengths. M4 is a high reflector at the laser wavelength, an OC at the signal wavelength, and it is transparent to the idler beam. M5 and M6 are dichroic beamsplitters coated for high transmission (reflection) at the laser (signal) wavelength. We assume that there is no residual reflection of the idler back into the OPO cavity and the idler is absent at the input of the nonlinear crystal ( $z_n = 0$ ), hence the OPO cavity is purely singly-resonant at the signal wavelength.

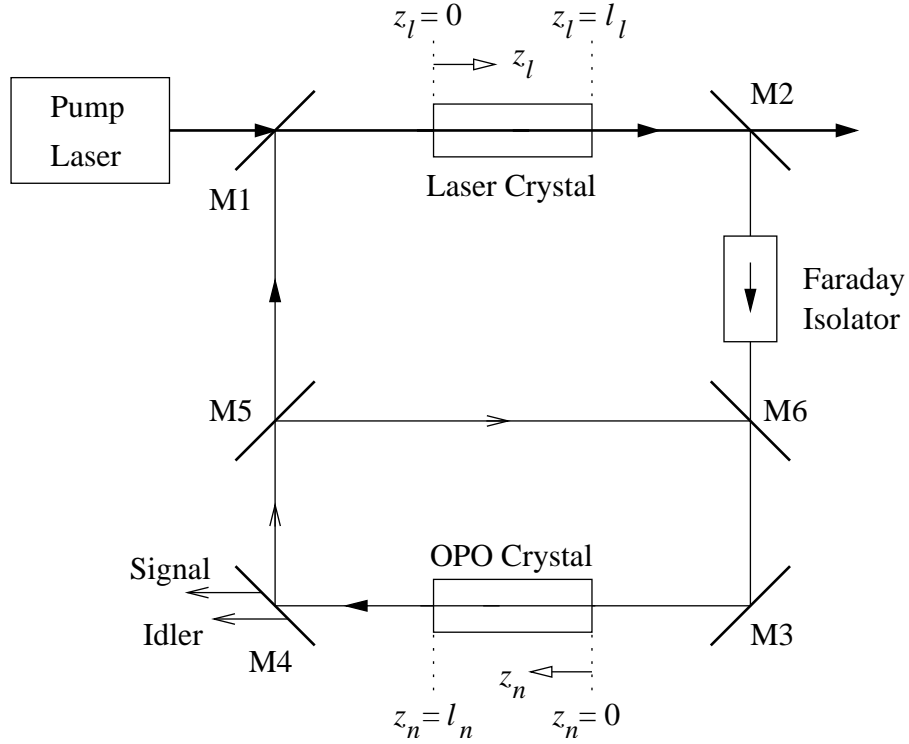


Figure 5.1: Schematic arrangement of the travelling-wave IOPO.

There are three distinct regions of operation associated with the singly-resonant IOPO depending on the input pump level [153]. In the first region where the input pump level is lower than the lasing threshold there is neither lasing nor parametric oscillation. In the second region where the pump level is higher than the lasing threshold but lower than the OPO threshold the intracavity laser field builds up from noise and in steady state the laser gain provided by the laser crystal saturates to value that compensates for the laser cavity losses exactly. In this region, the intracavity laser power increases linearly with the input power. Since the laser cavity is high-finesse, the values of the intracavity

laser power at the input and the exit of the laser crystal are approximately equal to each other.

In the third region where the input pump level is higher than the OPO threshold, both lasing and parametric oscillation occur. In this region, the intracavity laser field builds up from noise, and in steady state, the laser gain saturates to a value that exactly compensates for laser cavity losses including the nonlinear loss presented by the OPO. Similarly, the signal gain provided by the OPO crystal saturates at a point where all OPO cavity losses are exactly compensated for. With increasing input pump power, the intracavity laser power at the exit of the laser crystal increases linearly with a much lower slope from its value at the OPO threshold, when compared to its slope in the second region. On the other hand, the intracavity laser power at the input of the laser crystal decreases with a similar slope. In fact, in experiments where moderate input pump levels are used, the intracavity laser power levels at the input and the exit of the laser crystal seem to be clamped to a common value, which is the value at the OPO threshold [153]. Supporting this observation, the authors of the previous model for the cw IOPO [183] claim that there is perfect clamping of the intracavity laser power in this region. However, our model calculations show that this is not the case, especially at high input pump levels where the laser cavity is not high-finesse anymore due to the nonlinear loss presented by the OPO. In fact, increasing input pump level can result in appreciably large differences between the values of the intracavity laser power at the input and exit of the laser crystal.

Our model is based on the steady-state plane-wave equations which characterize the cw singly-resonant IOPO. We assume that all fields involved are of single-frequency nature and there is perfect phase-matching and no walk-off in the nonlinear crystal. We combine the steady-state forms of the ideal four-level-laser rate equations with the coupled-mode equations of the OPA [106] to obtain the single-pass description of the system. We, then, iteratively solve these equations to obtain a self-consistent solution for the field amplitudes in the laser and OPO cavities [58, 59].

We account for the spatial variation of the resonant signal (laser) field along

the propagation direction in the nonlinear crystal (in the laser and nonlinear crystals). At high pump levels and/or for IOPOs with long nonlinear crystals and high nonlinearities, inclusion of the longitudinal variation of the resonant fields in the model becomes a necessity for accuracy. Furthermore, unlike the previous model [183], we do not assume that the OPO cavity has a high finesse, but it has an OC (M4 in Fig. 5.1) for the signal and we try to optimize the useful loss of this mirror for optimum photon conversion efficiency for the signal or the idler. We find that at high pump levels and/or with long nonlinear crystals having high nonlinearities, the optimum useful loss of the output coupling mirror may turn out to be too high for the high-finesse OPO cavity assumption to be valid.

We employ the plane-wave approximation in our model. However, in cw IOPO experiments [153–163], the input pump beam usually has a Gaussian spatial profile and is focused at the center of the laser crystal to maximize the pump intensity. The Gaussian resonator mode that determines the spatial profile of the intracavity laser beam also has a focus at the laser crystal to match the pump focus. The intracavity laser beam, which is also the pump beam for the OPO, has a secondary focus at the center of the nonlinear crystal. The spot sizes of this beam at the laser and nonlinear crystals may be quite different from each other. We include the re-sizing of the beam in our equations with a parameter which is denoted by  $\eta_c$  and  $\eta_c = w_l/w_n$ , where  $w_l$  and  $w_n$  are the waist radii of the intracavity laser beam at the laser crystal and at the nonlinear crystal, respectively.

Furthermore, in a typical experiment, the laser cavity has some residual linear loss ( $L_l$ ) at the laser wavelength due to less than unity reflectivities of the cavity mirrors, imperfect antireflection coatings on the cavity components, such as the laser and nonlinear crystals and the Faraday isolator (see Fig. 5.1), and due to the absorption and scattering introduced by these components. We separate this loss into three parts:  $L_l^{(1)}$  denotes the linear loss that the intracavity laser power experiences in the optical path starting at the exit face of the laser crystal ( $z_l = l_l$ ) and ending at the input face of the nonlinear crystal ( $z_n = 0$ ) while travelling in the direction set by the Faraday isolator. Another component, which

is denoted by  $L_l^{(2)}$ , represents the linear loss in the optical path starting at the input face of the nonlinear crystal and ending at the input face of the laser crystal ( $z_l = 0$ ), again with a direction of propagation set by the Faraday isolator. Apart from  $L_l^{(1)}$  and  $L_l^{(2)}$ , for Ti:sapphire laser crystals, significant loss might be introduced to the intracavity laser power as a result of absorption at the laser wavelength [185, 186]. We account for this loss in our model with an absorption coefficient  $\alpha_l$ , whose value depends on the crystal growth technique used and the titanium ion concentration in the Ti:sapphire crystal [187, 188].

Similarly, the OPO cavity has some residual loss, which is denoted by  $L_s$ , at the signal wavelength. Also, the intracavity signal experiences a useful loss  $L_{oc}$  due to the partial reflectivity of M4. Furthermore, the nonresonant idler may experience reflection and absorption losses as it propagates through the nonlinear crystal and exits the OPO cavity through M4. Here, we assume that the losses experienced by the idler are negligibly small.

## 5.2 Laser Equations

The laser is assumed to be an ideal four-level system with the energy-level scheme shown in Fig. 5.2.  $N_0$ ,  $N_1$ ,  $N_2$  and  $N_3$  are the population densities at the corresponding energy levels. An external laser populates the top energy level (level 3), the population produced in this level relaxes dominantly to the upper laser level (level 2) with a decay rate of  $\tau_{32}^{-1}$  and to levels 1 and 0 with relaxation rates  $\tau_{31}^{-1}$  and  $\tau_{30}^{-1}$ , respectively. The lifetimes of levels 1 and 3, which are denoted by  $\tau_1$  and  $\tau_3$ , respectively, are much shorter than the fluorescent lifetime of the upper laser level which is denoted by  $\tau_2$ . Under these assumptions levels 1 and 3 are nearly empty.

The rate equation for the population density of the upper laser level, which is also the population-inversion density, can be written as [138, 189, 190]

$$\frac{dN_2}{dt} = \eta_p \frac{\sigma_p I_p(z)}{\hbar\omega_p} N_0(z) - \frac{N_2(z)}{\tau_2} - \frac{\sigma_l I_l(z)}{\hbar\omega_l} N_2(z), \quad (5.1)$$

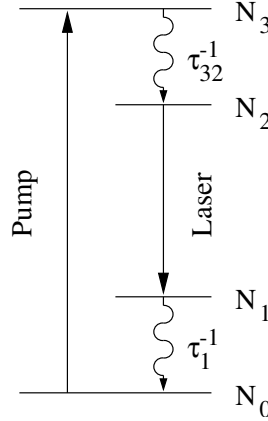


Figure 5.2: Energy-level diagram of the four-level system.

where  $\omega_p$  and  $\omega_l$  represent the frequencies of the pump and laser fields, respectively,  $z$  represents the axis of propagation,  $\sigma_p$  is the transition cross-section at the pump wavelength  $\lambda_p$ ,  $\sigma_l$  is the transition cross-section at the laser wavelength  $\lambda_l$ ,  $\eta_p$  denotes the quantum efficiency of the pump excitation into the upper laser level, which is the ratio of the relaxation rate of level 3 to level 2 and the overall relaxation rate of level 3 (i.e.,  $\tau_{32}^{-1}/\tau_3^{-1}$ ),  $I_p(z)$  and  $I_l(z)$  are the pump laser and circulating intracavity laser intensities as functions of  $z$ , respectively.

Also conservation of atoms requires

$$N = N_0 + N_2, \quad (5.2)$$

where  $N$  is total active center concentration.

Using Equations (5.1) and (5.2), the steady-state solution for  $N_2(z)$  can be written as [190]

$$N_2(z) = \frac{NI_p(z)/I_{ps}}{1 + I_l(z)/I_{ls} + I_p(z)/I_{ps}}, \quad (5.3)$$

where intracavity laser and pump laser saturation intensities are, respectively, defined as

$$I_{ls} = \frac{\hbar\omega_l}{\sigma_l\tau_2} \quad \text{and} \quad I_{ps} = \frac{\hbar\omega_p}{\eta_p\sigma_p\tau_2}. \quad (5.4)$$

Using Equation (5.3), the  $z$  variation of the intracavity laser intensity in the

laser crystal can be written as

$$\frac{dI_l}{dz} = N_2(z)\sigma_l I_l(z) - \alpha_l I_l(z) = \frac{NI_p(z)/I_{ps}}{1 + I_l(z)/I_{ls} + I_p(z)/I_{ps}}\sigma_l I_l(z) - \alpha_l I_l(z), \quad (5.5)$$

where  $\alpha_l$  is the loss coefficient (linear absorption) of the laser crystal at the laser wavelength.

A similar equation describes the  $z$  variation of the longitudinal pump intensity, which is given as

$$\frac{dI_p}{dz} = -N_0(z)\sigma_p I_p(z) = -\frac{N[1 + I_l(z)/I_{ls}]}{1 + I_l(z)/I_{ls} + I_p(z)/I_{ps}}\sigma_p I_p(z). \quad (5.6)$$

Equations (5.5) and (5.6) can also be written in terms of normalized field amplitudes  $a_l(z)$  and  $a_p(z)$  such that  $\phi_l = a_l^2(z) = I_l/\hbar\omega_l$  and  $\phi_p = a_p^2(z) = I_p/\hbar\omega_p$  represent the photon flux densities of the intracavity laser field and the pump field, respectively. Thus,

$$\frac{da_l}{dz} = \frac{1}{2} \left[ \frac{N\sigma_l(a_p(z)/a_{ps})^2}{1 + (a_l(z)/a_{ls})^2 + (a_p(z)/a_{ps})^2} \right] a_l(z) - \frac{1}{2}\alpha_l a_l(z), \quad (5.7)$$

$$\frac{da_p}{dz} = -\frac{1}{2} \left[ \frac{N\sigma_p[1 + (a_l(z)/a_{ls})^2]}{1 + (a_l(z)/a_{ls})^2 + (a_p(z)/a_{ps})^2} \right] a_p(z), \quad (5.8)$$

where  $a_{ls}^2$  and  $a_{ps}^2$  are the intracavity laser and pump laser saturation photon flux densities, respectively, which are given by

$$a_{ls}^2 = \frac{1}{\sigma_l\tau_2} \quad \text{and} \quad a_{ps}^2 = \frac{1}{\eta_p\sigma_p\tau_2}. \quad (5.9)$$

### 5.3 Travelling-Wave IOPO Equations

For the IOPO, the pump for the OPO is the intracavity laser field. Equations (5.7)–(5.8) and Equations (2.53)–(2.55) for the OPA (see Section 2.6 of Chapter 2) can be rewritten to form the set of single-pass equations for the travelling-wave IOPO, which is given as

$$\frac{da_l}{dz_l} = \frac{1}{2} \left[ \frac{N\sigma_l(a_p(z_l)/a_{ps})^2}{1 + (a_l(z_l)/a_{ls})^2 + (a_p(z_l)/a_{ps})^2} \right] a_l(z_l) - \frac{1}{2}\alpha_l a_l(z_l), \quad (5.10)$$

$$\frac{da_p}{dz_l} = -\frac{1}{2} \left[ \frac{N\sigma_p [1 + (a_l(z_l)/a_{ls})^2]}{1 + (a_l(z_l)/a_{ls})^2 + (a_p(z_l)/a_{ps})^2} \right] a_p(z_l), \quad (5.11)$$

$$\frac{da_1}{dz_n} = \kappa a_3(z_n) a_2(z_n), \quad (5.12)$$

$$\frac{da_2}{dz_n} = \kappa a_3(z_n) a_1(z_n), \quad (5.13)$$

$$\frac{da_3}{dz_n} = -\kappa a_1(z_n) a_2(z_n), \quad (5.14)$$

with

$$a_3(z_n = 0) = \eta_c \left(1 - L_l^{(1)}\right)^{1/2} a_l(z_l = l_l), \quad (5.15)$$

where indices 1, 2, and 3 represent the idler, signal, and OPO pump, respectively,  $\phi_i = a_i^2$  ( $i = 1, 2, 3$ ) are the corresponding photon flux densities,  $z_l$  is the distance along the laser crystal of length  $l_l$ ,  $z_n$  is the distance along the nonlinear crystal of length  $l_n$  (see Fig. 5.1), and  $L_l^{(1)}$  and  $\eta_c$  are the loss term and beam re-sizing parameter, respectively, as defined in Section 5.1. Expressions for  $a_{ls}^2$  and  $a_{ps}^2$  are as given in Equation (5.9) and  $\kappa$  is the coupling constant as defined in Equation (2.46) with  $\omega_3$  being the frequency of the intracavity laser field, that is,  $\omega_3 = \omega_l$ .

By scaling the normalized field amplitudes,  $a_l$ ,  $a_p$ ,  $a_1$ ,  $a_2$ , and  $a_3$  with  $\kappa l_n$  to obtain  $A_l$ ,  $A_p$ ,  $A_1$ ,  $A_2$ , and  $A_3$ , respectively, Equations (5.10)–(5.15) can be written in terms of unitless quantities in the following form

$$\frac{dA_l}{d\xi_l} = \frac{1}{2} \left[ \frac{\Gamma_1 (A_p(\xi_l)/A_{ps})^2}{1 + (A_l(\xi_l)/A_{ls})^2 + (A_p(\xi_l)/A_{ps})^2} \right] A_l(\xi_l) - \frac{1}{2} L A_l(\xi_l), \quad (5.16)$$

$$\frac{dA_p}{d\xi_l} = -\frac{1}{2} \left[ \frac{\Gamma_2 [1 + (A_l(\xi_l)/A_{ls})^2]}{1 + (A_l(\xi_l)/A_{ls})^2 + (A_p(\xi_l)/A_{ps})^2} \right] A_p(\xi_l), \quad (5.17)$$

$$\frac{dA_1}{d\xi_n} = A_3(\xi_n) A_2(\xi_n), \quad (5.18)$$

$$\frac{dA_2}{d\xi_n} = A_3(\xi_n) A_1(\xi_n), \quad (5.19)$$

$$\frac{dA_3}{d\xi_n} = -A_1(\xi_n) A_2(\xi_n), \quad (5.20)$$

with

$$A_3(\xi_n = 0) = \eta_c \left(1 - L_l^{(1)}\right)^{1/2} A_l(\xi_l = 1), \quad (5.21)$$

where  $\xi_l = z_l/l_l$ ,  $\xi_n = z_n/l_n$ , and the following definitions are used:

$$A_l(\xi_l) = \kappa l_n a_l(z_l), \quad A_p(\xi_l) = \kappa l_n a_p(z_l), \quad A_i(\xi_n) = \kappa l_n a_i(z_n) \quad i = 1, 2, 3, \quad (5.22)$$

$$\Gamma_1 = N\sigma_l l, \quad \Gamma_2 = N\sigma_p l, \quad \text{and } L = \alpha_l l, \quad (5.23)$$

$$A_{ls} = \kappa l_n a_{ls} \quad \text{and} \quad A_{ps} = \kappa l_n a_{ps}. \quad (5.24)$$

The input parameter for the travelling-wave IOPO is the normalized field amplitude of the pump laser at the input facet of the laser crystal,  $a_p(z_l = 0)$ , which is given in the following unitless form

$$A_p(\xi_l = 0) = \kappa l_n a_p(z_l = 0). \quad (5.25)$$

Equations (5.16)–(5.17) (laser equations) are numerically solved by employing the adaptive-stepsize Runge-Kutta finite-differencing method [151]. Furthermore, using Equations (2.56)–(2.63) (see Section 2.6), exact solutions to Equations (5.18)–(5.20) (unitless OPA equations) are obtained in terms of Jacobi elliptic functions in the following unitless form

$$A_1(\xi_n) = \sqrt{C'_1} \text{cn}(Z'_a | m'_a), \quad (5.26)$$

$$A_2(\xi_n) = \sqrt{C'_2} \text{dn}(Z'_a | m'_a), \quad (5.27)$$

$$A_3(\xi_n) = \sqrt{C'_1} \text{sn}(Z'_a | m'_a), \quad (5.28)$$

where  $C'_1$  and  $C'_2$  are the unitless Manley-Rowe conserved quantities given as

$$C'_1 = A_1^2(\xi_n) + A_3^2(\xi_n) = A_3^2(\xi_n = 0), \quad (5.29)$$

$$C'_2 = A_2^2(\xi_n) + A_3^2(\xi_n) = A_2^2(\xi_n = 0) + A_3^2(\xi_n = 0), \quad (5.30)$$

and

$$m'_a = C'_1/C'_2, \quad (5.31)$$

$$Z'_a = K(m'_a) - \sqrt{C'_2} \xi_n, \quad (5.32)$$

where  $K(m)$  is the definition of the quarter-period of the Jacobi elliptic functions given in Equation (2.63).

Having obtained the single-pass numerical and exact solutions of the laser and OPA equations, respectively, we use numerical iteration to determine the field amplitudes for the travelling-wave IOPO for a given input pump level  $A_p(\xi_l = 0)$ . We start out with initial intracavity laser and OPO signal photon flux densities

to represent the spontaneous emission of the laser crystal and the parametric fluorescence of the nonlinear crystal, respectively. We then iterate these through the system several times by using these single-pass solutions until the self-consistency condition in the laser and OPO cavities is satisfied, that is, until the saturated laser and OPO gains exactly compensate for the laser and OPO cavity losses, respectively [58, 59].

For each iteration the input parameter,  $A_p(\xi_l = 0)$ , is kept fixed and the initial conditions for  $A_l(\xi_l = 0)$  at the input facet of the laser crystal and  $A_2(\xi_n = 0)$  at the input facet of the nonlinear crystal are updated as follows

$$A_l^{(i)}(\xi_l = 0) = (1/\eta_c) \left(1 - L_l^{(2)}\right)^{1/2} A_3^{(i-1)}(\xi_n = 1), \quad (5.33)$$

$$A_2^{(i)}(\xi_n = 0) = [(1 - L_s)(1 - L_{oc})]^{1/2} A_2^{(i-1)}(\xi_n = 1), \quad (5.34)$$

where  $i$  is the iteration number and  $L_l^{(2)}$ ,  $L_s$  and  $L_{oc}$  are the loss terms introduced in Section 5.1.

Upon specification of the input parameter:  $A_p(\xi_l = 0)$ , and the system parameters:  $\Gamma_1$ ,  $\Gamma_2$ ,  $L$ ,  $A_{ls}$ ,  $A_{ps}$ ,  $\eta_c$ ,  $L_l^{(1)}$ ,  $L_l^{(2)}$ ,  $L_s$ , and  $L_{oc}$ , the signal and idler outputs of the travelling-wave IOPO, which are given by

$$A_2^{\text{out}} = \sqrt{L_{oc}} A_2(\xi_n = 1) \quad \text{and} \quad A_1^{\text{out}} = A_1(\xi_n = 1), \quad (5.35)$$

respectively, where the losses experienced by the idler are assumed to be negligibly small, can uniquely be determined when the iterative process converges or the self-consistency condition in both the laser and OPO cavities is satisfied. The pump-to-signal and pump-to-idler photon conversion efficiencies are  $(A_2^{\text{out}})^2/A_p^2(\xi_l = 0)$  [or  $\phi_2^{\text{out}}/\phi_p(z_l = 0)$ ] and  $(A_1^{\text{out}})^2/A_p^2(\xi_l = 0)$  [or  $\phi_1^{\text{out}}/\phi_p(z_l = 0)$ ], respectively. For modelling an experiment with  $\eta_c \neq 1$ , the beam sizes of the input pump, signal and idler beams should be taken into account and the pump-to-signal or pump-to-idler photon conversion efficiencies are not simply the ratios of the corresponding photon flux densities, but they are the ratios of the corresponding photon fluxes in units of photons/s, which can be approximately calculated by multiplying the photon flux densities with their corresponding beam areas.

## 5.4 Results and Conclusions

In this section, we present sample results of our model for the cw IOPOs. The parameters of the laser system based on a Ti:sapphire crystal are shown in Table 5.1. These parameters are held fixed for the examples presented.

The residual absorption coefficient  $\alpha_l$  for the laser wavelength depends on the  $\text{Ti}^{3+}$  concentration and the crystal production technique. In general, for a fixed production method, this coefficient tends to increase with increasing  $\text{Ti}^{3+}$  concentration. For instance, Ti:sapphire crystals having  $0.01 \leq \alpha_l \leq 0.27 \text{ cm}^{-1}$  for  $2.3 \times 10^{19} \leq N \leq 13.5 \times 10^{19} \text{ cm}^{-3}$  were reported [188]. However, it is also possible to encounter two Ti:sapphire crystals with similar  $\text{Ti}^{3+}$  concentrations but quite different  $\alpha_l$  values due to different production techniques employed in crystal growth [186, 188]. In the examples presented in this section, the  $\text{Ti}^{3+}$  concentration is held fixed at the value shown in Table 5.1 and in the first two examples  $\alpha_l = 0.01 \text{ cm}^{-1}$  [188] is used, whereas in the last example both  $\alpha_l = 0.01 \text{ cm}^{-1}$  and  $\alpha_l = 0.07 \text{ cm}^{-1}$  [186]<sup>1</sup> are used for comparison.

$\lambda_p$	514 nm
$\lambda_l$	800 nm
$\sigma_p$ at $\lambda_p$ ( $p$ -polarization)	$6 \times 10^{-20} \text{ cm}^2$ [185]
$\sigma_l$ at $\lambda_l$ ( $p$ -polarization)	$3 \times 10^{-19} \text{ cm}^2$ [185, 191]
$\eta_p$	$\approx 1$ [138, 186]
$\tau_2$	$3.2 \mu\text{s}$ [185]
$N$ ( $\text{Ti}^{3+}$ )	$3.3 \times 10^{19} \text{ cm}^{-3}$ (typical) [188]
$l_l$	2 cm (typical)
$L_l^{(1)}, L_l^{(2)}$	1%, 1% (typical)

Table 5.1: Parameters of the laser system based on a Ti:sapphire crystal.

We first present the results for an IOPO based on KTA as the nonlinear crystal with different output coupling losses  $L_{oc}$ . Next we present an example where the beam re-sizing parameter  $\eta_c$  is varied for this KTA IOPO. Lastly, we present the

<sup>1</sup>In Ref. [186], this value was reported to be the loss coefficient of the Ti:sapphire crystals used in the commercial lasers, Tsunami (Spectra-Physics) and Mira (Coherent).

results of the optimization of  $L_{oc}$  for maximum signal and idler output for a range of input photon flux densities and OPO crystal nonlinearities. In these examples, the maximum input photon flux density is chosen to be  $3.2 \times 10^{24}$  photons/cm<sup>2</sup>-s. This photon flux density is equivalent to the flux density of the 35-W output beam of an argon-ion laser operating at 514-nm which is focused to a spot with a diameter of 60  $\mu$ m.

### 5.4.1 Example-1

We first consider a KTA OPO placed internal to the cavity of a Ti:sapphire laser with the specifications given in Table 5.1 and  $\alpha_l = 0.01$  cm<sup>-1</sup>. The KTA crystal is cut along  $\theta = 90^\circ$  and  $\phi = 0^\circ$  for noncritical phase matching the type-II parametric interaction where a  $p$ -polarized (horizontal, fast axis) signal beam at 1145 nm and an  $s$ -polarized (vertical, slow axis) idler beam at 2655 nm are generated from the  $p$ -polarized pump beam at 800 nm. For this interaction,  $d_{eff} = 3.33$  pm/V yielding  $\kappa l_n = 1.35 \times 10^{-13}$  cm-s<sup>1/2</sup> for  $l_n = 2$  cm. The residual loss for the OPO cavity is  $L_s = 2\%$  and the beam re-sizing parameter is chosen to be  $\eta_c = 1$ .

Figure 5.3 shows the intracavity laser photon flux densities at the input and exit of the Ti:sapphire laser crystal and signal and idler photon flux densities at the output of the OPO cavity as functions of the input photon flux density for  $L_{oc} = 1\%$ , 10%, and 20%. The input pump photon flux density [ $\phi_p(z_l = 0)$ ] at the laser threshold is as low as  $3.3 \times 10^{22}$  photons/cm<sup>2</sup>-s and  $\phi_p(z_l = 0)$  values at the OPO threshold are  $1.1 \times 10^{23}$ ,  $3.3 \times 10^{23}$ , and  $6.1 \times 10^{23}$  photons/cm<sup>2</sup>-s for  $L_{oc} = 1\%$ , 10%, and 20%, respectively.

As it is evident from Fig. 5.3-(a) and (b), at large input power levels, it is not possible to state that the intracavity laser power is clamped to its threshold value and the assumption of high-finesse laser cavity of the previous model [183] is not valid. In Figure 5.3-(a) and (b), starting at the laser threshold and with increasing  $\phi_p(z_l = 0)$ , the intracavity laser photon flux densities at the input and exit of the laser crystal,  $\phi_l(z_l = 0)$  and  $\phi_l(z_l = 2$  cm), rise linearly and their values

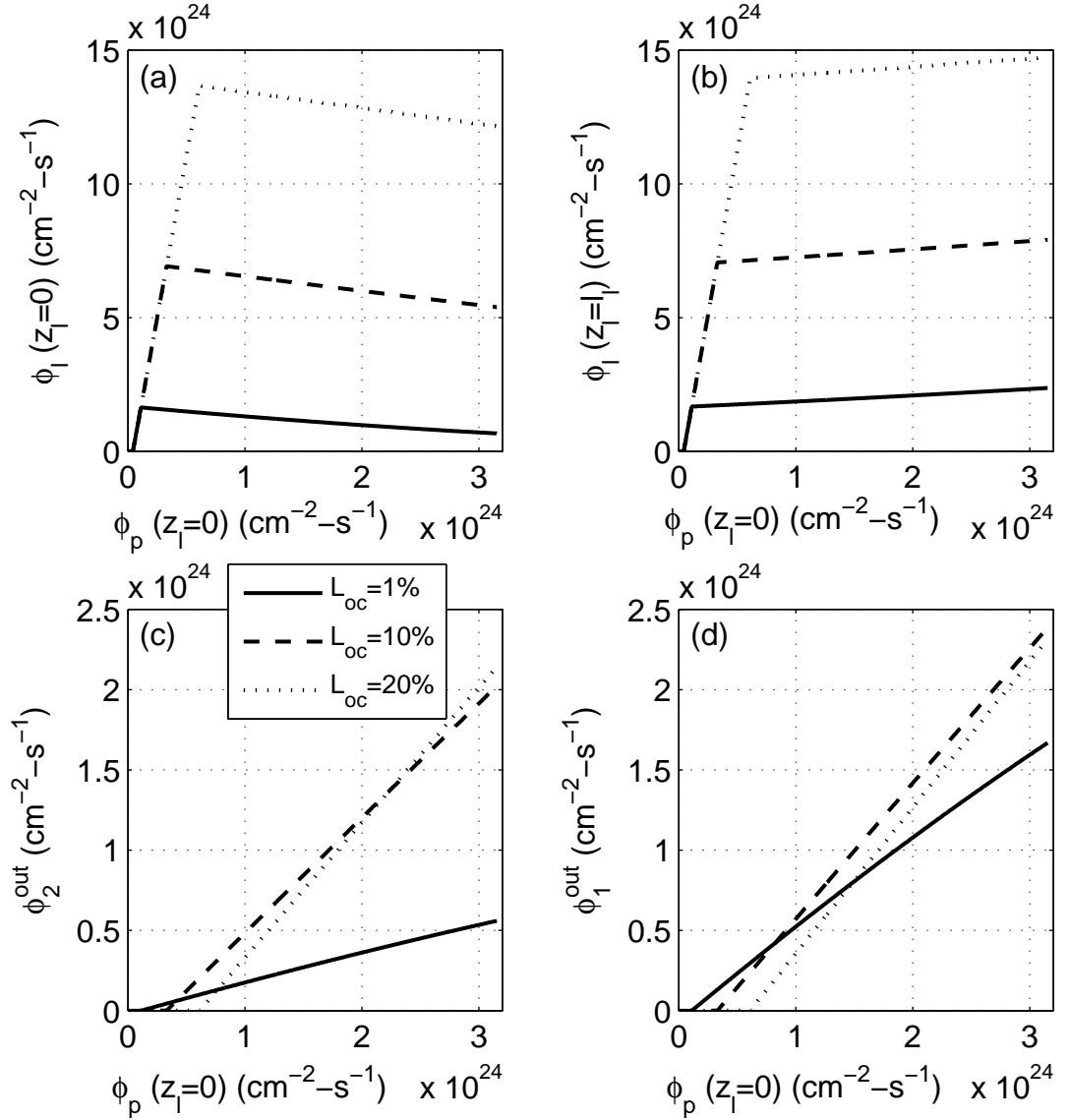


Figure 5.3: Intracavity laser photon flux densities at the (a) input and (b) exit of the Ti:sapphire laser crystal and (c) signal and (d) idler photon flux densities at the output of the OPO cavity as functions of the input photon flux density for  $L_{oc} = 1\%$ ,  $10\%$ , and  $20\%$ . For these calculations, in addition to the laser parameters given in Table 5.1,  $\alpha_l = 0.01 \text{ cm}^{-1}$ ,  $\eta_c = 1$ ,  $\kappa l_n = 1.35 \times 10^{-13} \text{ cm-s}^{1/2}$ , and  $L_s = 2\%$ .

are approximately equal to each other due to the high-finesse nature of the laser cavity, which is only valid when the OPO is below threshold. As  $\phi_p(z_l = 0)$  is further increased, the OPO threshold is surpassed and  $\phi_l(z_l = 0)$  [ $\phi_l(z_l = 2 \text{ cm})$ ] decreases [increases] but with a much smaller rate compared to the one before the OPO threshold. However, at large values of  $\phi_p(z_l = 0)$ , the values of  $\phi_l(z_l = 0)$  and  $\phi_l(z_l = 2 \text{ cm})$  can be appreciably different from their values at the OPO threshold. For instance, for the IOPO with  $L_{oc} = 1\%$ ,  $\phi_l(z_l = 0)$  [ $\phi_l(z_l = 2 \text{ cm})$ ] at the maximum input photon flux density is about 60% [40%] smaller [larger] than its value at the OPO threshold, hence the saturated gain provided by the laser crystal [ $\phi_l(z_l = 2 \text{ cm})/\phi_l(z_l = 0)$ ] is as high as 3.5. As  $L_{oc}$  increases, the gain is less, but still quite large. For the IOPOs with  $L_{oc} = 10\%$  and  $L_{oc} = 20\%$ , the gains are about 1.5 and 1.2, respectively. A large saturated gain indicates that the nonlinear loss presented by the OPO is large, hence the laser cavity cannot be described as high-finesse.

Further conclusions can be drawn by considering Fig. 5.3-(c) and (d). When  $\phi_p(z_l = 0) > 6.1 \times 10^{23}$  photons/cm<sup>2</sup>-s, hence the OPO is above threshold for all three  $L_{oc}$ 's, at input pump photon flux densities within the range of  $6.1 \times 10^{23} < \phi_p(z_l = 0) < 2.2 \times 10^{24}$  photons/cm<sup>2</sup>-s and  $2.2 \times 10^{24} < \phi_p(z_l = 0) < 3.2 \times 10^{24}$  photons/cm<sup>2</sup>-s, one would choose the OC with  $L_{oc} = 10\%$  and the OC with  $L_{oc} = 20\%$ , respectively, among these three OCs for achieving the largest signal output possible. Similarly, at input pump photon flux densities within the range of  $6.1 \times 10^{23} < \phi_p(z_l = 0) < 8.4 \times 10^{23}$  photons/cm<sup>2</sup>-s and  $8.4 \times 10^{23} < \phi_p(z_l = 0) < 3.2 \times 10^{24}$  photons/cm<sup>2</sup>-s, one would prefer to use the OC with  $L_{oc} = 1\%$  and the OC with  $L_{oc} = 10\%$ , respectively, for achieving the largest idler output possible. This is an indication of the fact that the optimization of the signal and idler outputs may require the use of different OCs depending on the input pump level. Such an optimization for the signal and idler outputs also depends on the value of  $\kappa l_n$ , as it will be explained in the last example of this section.

### 5.4.2 Example-2

In this example, we use the same KTA IOPO of the previous example with the laser system specifications given in Table 5.1. We also use the following parameters:  $\alpha_l = 0.01 \text{ cm}^{-1}$ ,  $\kappa l_n = 1.35 \times 10^{-13} \text{ cm-s}^{1/2}$  ( $l_n = 2 \text{ cm}$ ),  $L_s = 2\%$ , and  $L_{oc} = 20\%$ .

Figure 5.4 shows the intracavity laser photon flux densities at the input and exit of the Ti:sapphire laser crystal and signal and idler photon flux densities at the output of the OPO cavity as functions of the input photon flux density for different values of the beam re-sizing parameter,  $\eta_c = 0.5, 1.0,$  and  $1.5$ . The input pump photon flux density [ $\phi_p(z_l = 0)$ ] at the laser threshold is as low as  $3.3 \times 10^{22}$  photons/cm<sup>2</sup>-s, which is the same as the one obtained in the first example and  $\phi_p(z_l = 0)$  values at the OPO threshold are  $2.3 \times 10^{24}$ ,  $6.1 \times 10^{23}$ , and  $2.9 \times 10^{23}$  photons/cm<sup>2</sup>-s for  $\eta_c = 0.5, 1.0,$  and  $1.5$ , respectively. Hence, a 3-fold increase in  $\eta_c$  results in an almost 8-fold reduction in the threshold value of the IOPO. This is as expected, since  $\eta_c$  is the ratio of the radius of the intracavity laser beam at the laser crystal to the radius of the same beam, or OPO pump, at the nonlinear crystal and the intensity is inversely proportional to the square of the beam radius.

Considering Fig. 5.4-(c), it is possible to obtain more than 2-fold and 26-fold larger signal photon flux densities with  $\eta_c = 1.5$  compared to those with  $\eta_c = 1.0$  and  $\eta_c = 0.5$ , respectively, at the maximum input pump photon flux density. However, it should be noted that when  $\eta_c$  is included in the model, the pump-to-signal photon conversion efficiency is no longer simply the ratio of the photon flux density of the signal to that of the input pump. Instead, in an experimental situation, the beam sizes of the input pump and the signal should be taken into account to determine the ratio of the photon fluxes (not flux densities) of the signal and input pump beams which will yield the true photon conversion efficiency. Furthermore, in cw IOPO experiments [153], the confocal parameters of the intracavity laser beam at the laser and nonlinear crystals are usually chosen to be similar to the lengths of the corresponding crystals to keep the intensity of the beam large enough along the whole length of the laser/nonlinear crystal,

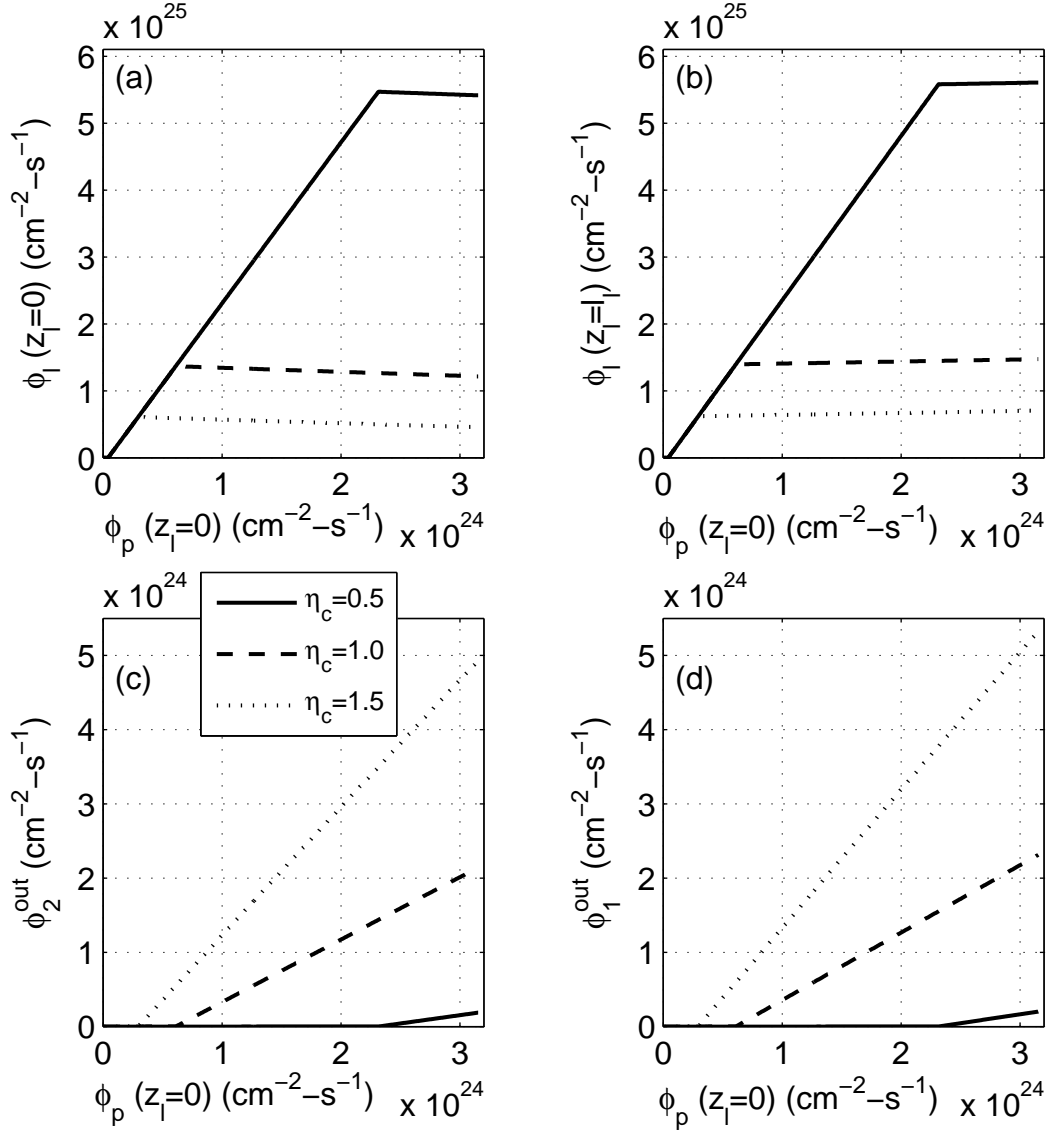


Figure 5.4: Intracavity laser photon flux densities at the (a) input and (b) exit of the Ti:sapphire laser crystal and (c) signal and (d) idler photon flux densities at the output of the OPO cavity as functions of the input photon flux density for  $\eta_c = 0.5, 1.0,$  and  $1.5$ . For these calculations, in addition to the laser parameters given in Table 5.1,  $\alpha_l = 0.01 \text{ cm}^{-1}$ ,  $\kappa l_n = 1.35 \times 10^{-13} \text{ cm-s}^{1/2}$ ,  $L_s = 2\%$ , and  $L_{oc} = 20\%$ .

hence, to minimize the reduction in intensity due to the diffraction of the beam. Also, the laser crystal usually has the same length as the nonlinear crystal or shorter, which is usually the case, since the laser crystal should only be long enough to absorb almost all the input pump power, whereas the nonlinear crystal length should be as long as possible for high conversion efficiencies with the assumption that the limit for backconversion is not reached. With these two arguments,  $\eta_c \lesssim 1.0$  in cw IOPO experiments.

### 5.4.3 Example-3

In this example, we assume that the the laser system specifications given in Table 5.1 are fixed. Also,  $\eta_c = 1.0$  and  $L_s = 2\%$ . We determine the optimum values of  $L_{oc}$  for maximum signal and idler photon conversion efficiencies for given values of  $\phi_p(z_l = 0)$  and  $\kappa l_n$ . We do these calculations for two cases:  $\alpha_l = 0.01 \text{ cm}^{-1}$  and  $\alpha_l = 0.07 \text{ cm}^{-1}$ .

The range for input pump flux density is chosen as  $7.9 \times 10^{21} \leq \phi_p(z_l = 0) \leq 3.2 \times 10^{24}$  photons/cm<sup>2</sup>-s. As mentioned before, the maximum input photon flux density is equivalent to the flux density of the 35-W output beam of an argon-ion laser operating at 514-nm which is focused to a spot with a diameter of 60  $\mu\text{m}$ . From Equation (5.25) for the unitless input parameter,  $A_p^2(\xi_l = 0) = \kappa^2 l_n^2 a_p^2(z_l = 0) = \kappa^2 l_n^2 \phi_p(z_l = 0)$ , hence in presenting our results, we use  $\kappa^2 l_n^2$  rather than  $\kappa l_n$ . We consider three nonlinear crystals with relatively low, high and quite high  $d_{\text{eff}}$  values, which are LBO, KTA, and PPLN, respectively. For parametric generation of 1145 nm (signal) and 2655 nm (idler) from 800 nm (pump) in a type-I configuration, an LBO crystal (cut along  $\theta = 90^\circ$  and  $\phi = 22.8^\circ$ ) has  $d_{\text{eff}} = 0.74 \text{ pm/V}$ , hence a 2-cm-long crystal would have  $\kappa^2 l_n^2 = 1.3 \times 10^{-27} \text{ cm}^2\text{-s}$ . For the same wavelengths, a 2-cm-long KTA that is mentioned in the first example would have  $\kappa^2 l_n^2 = 1.8 \times 10^{-26} \text{ cm}^2\text{-s}$ . A 2-cm-long PPLN crystal would have  $d_{\text{eff}} = 16 \text{ pm/V}$  for quasi-phase matching the same interaction with all fields polarized along the  $z$ -axis of the crystal, yielding  $\kappa^2 l_n^2 = 2.5 \times 10^{-25} \text{ cm}^2\text{-s}$ . Hence, we have chosen the  $\kappa^2 l_n^2$  range as  $1 \times 10^{-27} \leq \kappa^2 l_n^2 \leq 5 \times 10^{-25} \text{ cm}^2\text{-s}$ .

Figure 5.5 shows the contour plots for the maximum pump-to-signal photon conversion efficiency and the corresponding  $L_{oc}$  as functions of  $\phi_p(z_l = 0)$  and  $\kappa^2 l_n^2$ , when  $\alpha_l = 0.01 \text{ cm}^{-1}$ . For instance, for the IOPO based on the PPLN crystal mentioned above, it is possible to obtain a maximum of 73% pump-to-signal photon conversion efficiency with the optimum  $L_{oc} = 77\%$  at  $\phi_p(z_l = 0) = 2.5 \times 10^{24} \text{ photons/cm}^2\text{-s}$ . It is evident that for large values of  $\phi_p(z_l = 0)$  and  $\kappa^2 l_n^2$  the assumption of high-finesse OPO cavity cannot be valid when optimum OCs, whose useful losses can be quite large, are used.

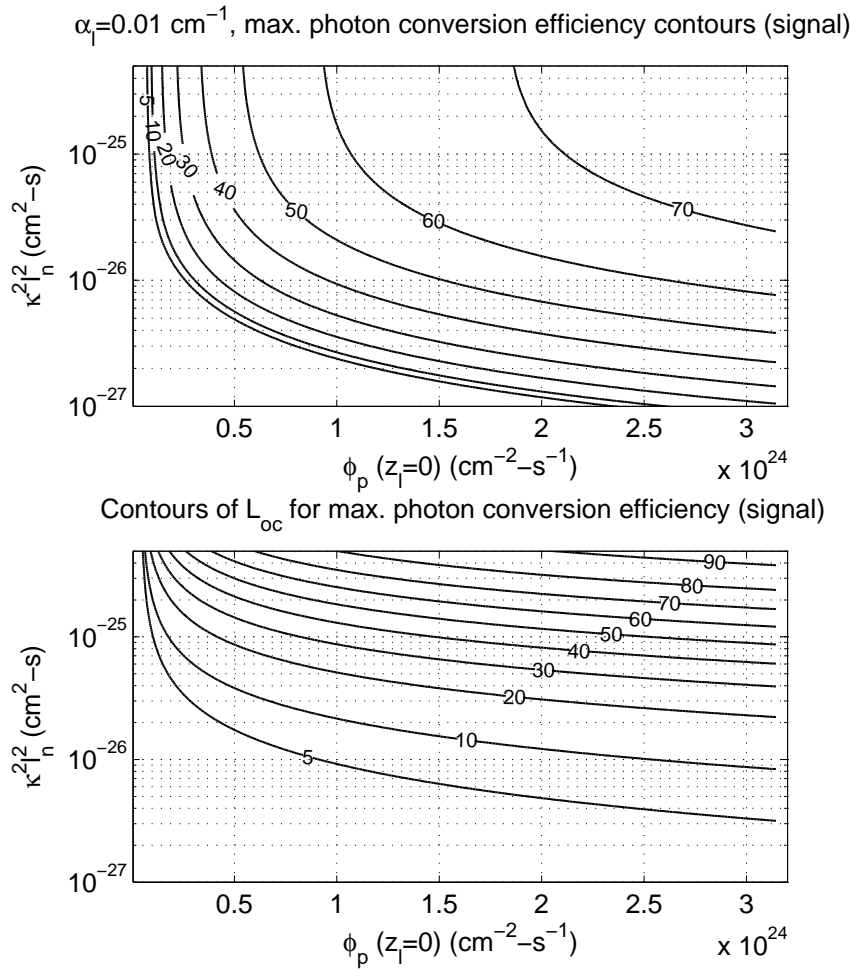


Figure 5.5: Contour plots for the maximum pump-to-signal photon conversion efficiency and the corresponding  $L_{oc}$  as functions of  $\phi_p(z_l = 0)$  and  $\kappa^2 l_n^2$ . For these calculations, in addition to the laser parameters given in Table 5.1,  $\alpha_l = 0.01 \text{ cm}^{-1}$ ,  $\eta_c = 1.0$ , and  $L_s = 2\%$ . The values shown on the contours are in percent.

Figure 5.6 shows the contour plots for the maximum pump-to-signal photon conversion efficiency and the corresponding  $L_{oc}$  as functions of  $\phi_p(z_l = 0)$  and  $\kappa^2 l_n^2$ , when  $\alpha_l = 0.07 \text{ cm}^{-1}$ . In this case, maximum achievable conversion efficiencies are lower than the case with  $\alpha_l = 0.01 \text{ cm}^{-1}$ . For instance, for the IOPO based on the same PPLN crystal, it is possible to obtain a maximum of 50% pump-to-signal photon conversion efficiency with the optimum  $L_{oc} = 50\%$  at  $\phi_p(z_l = 0) = 2.5 \times 10^{24} \text{ photons/cm}^2\text{-s}$ .

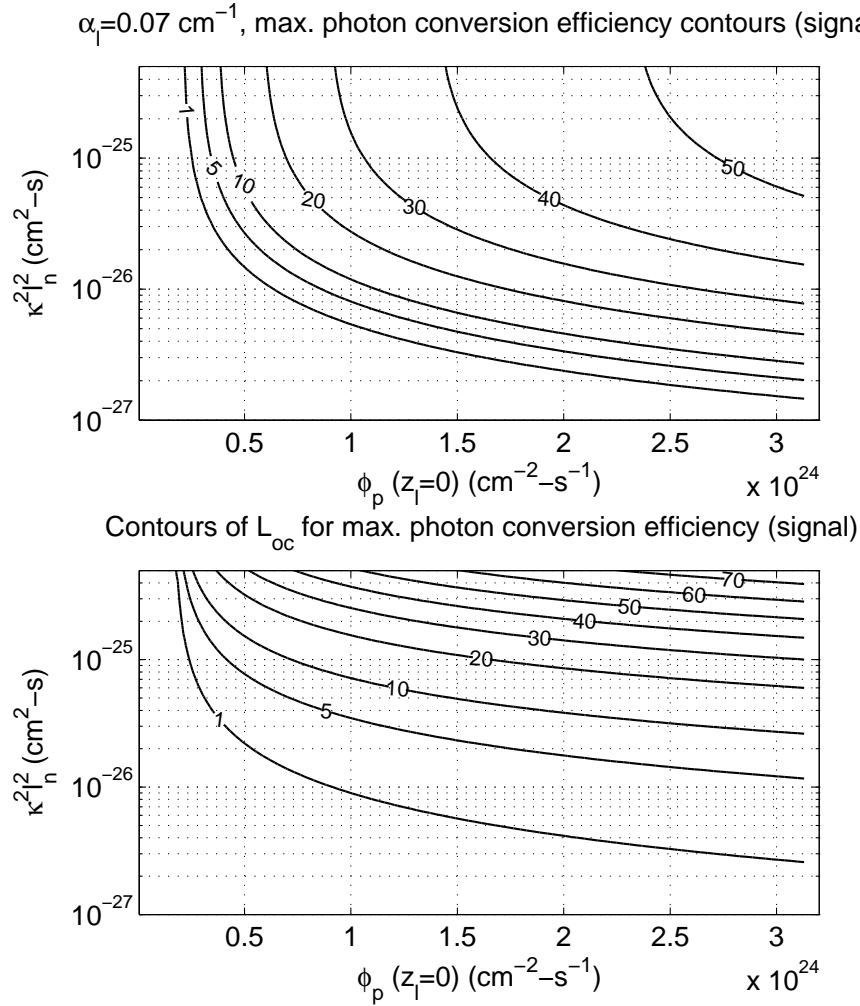


Figure 5.6: Contour plots for the maximum pump-to-signal photon conversion efficiency and the corresponding  $L_{oc}$  as functions of  $\phi_p(z_l = 0)$  and  $\kappa^2 l_n^2$ . For these calculations, in addition to the laser parameters given in Table 5.1,  $\alpha_l = 0.07 \text{ cm}^{-1}$ ,  $\eta_c = 1.0$ , and  $L_s = 2\%$ . The values shown on the contours are in percent.

Figures 5.7 and 5.8 show the contour plots for the maximum pump-to-idler photon conversion efficiency and the corresponding  $L_{oc}$  as functions of  $\phi_p(z_l = 0)$  and  $\kappa^2 l_n^2$ , when  $\alpha_l = 0.01 \text{ cm}^{-1}$  and  $\alpha_l = 0.07 \text{ cm}^{-1}$ , respectively. The plots for the maximum pump-to-idler conversion efficiency (top plots in these figures) contains straight lines as the contours, rather than curves. This means that at a certain input photon flux density, the maximum photon conversion efficiency stays constant for changing values of  $\kappa^2 l_n^2$ . Similar to the case for the signal photon conversion, with increasing  $\alpha_l$ , lower efficiencies are achievable at given values of  $\phi_p(z_l = 0)$  and  $\kappa^2 l_n^2$ .

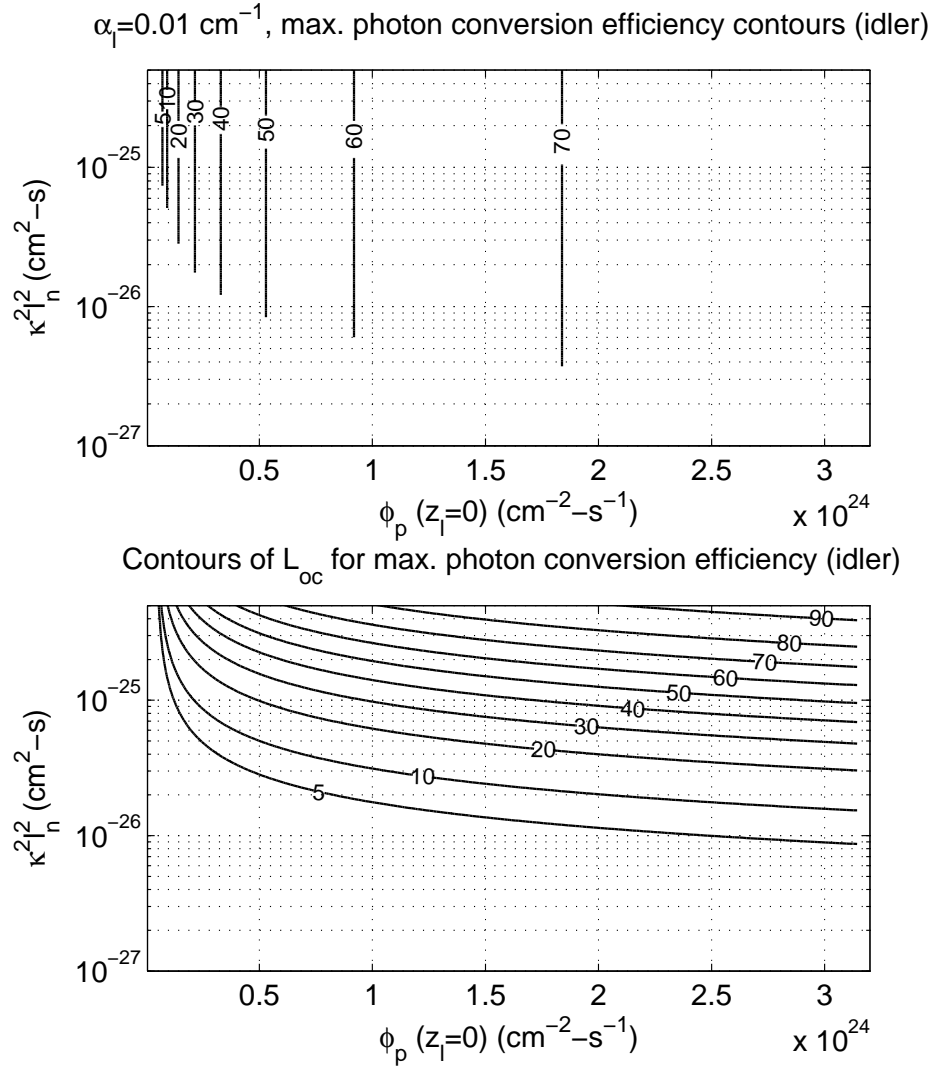


Figure 5.7: Contour plots for the maximum pump-to-idler photon conversion efficiency and the corresponding  $L_{oc}$  as functions of  $\phi_p(z_l = 0)$  and  $\kappa^2 l_n^2$ . For these calculations, in addition to the laser parameters given in Table 5.1,  $\alpha_l = 0.01 \text{ cm}^{-1}$ ,  $\eta_c = 1.0$ , and  $L_s = 2\%$ . In both plots, the values shown on the contours are in percent and in the top plot, only the values corresponding to  $L_{oc} > 0.2\%$  are shown.

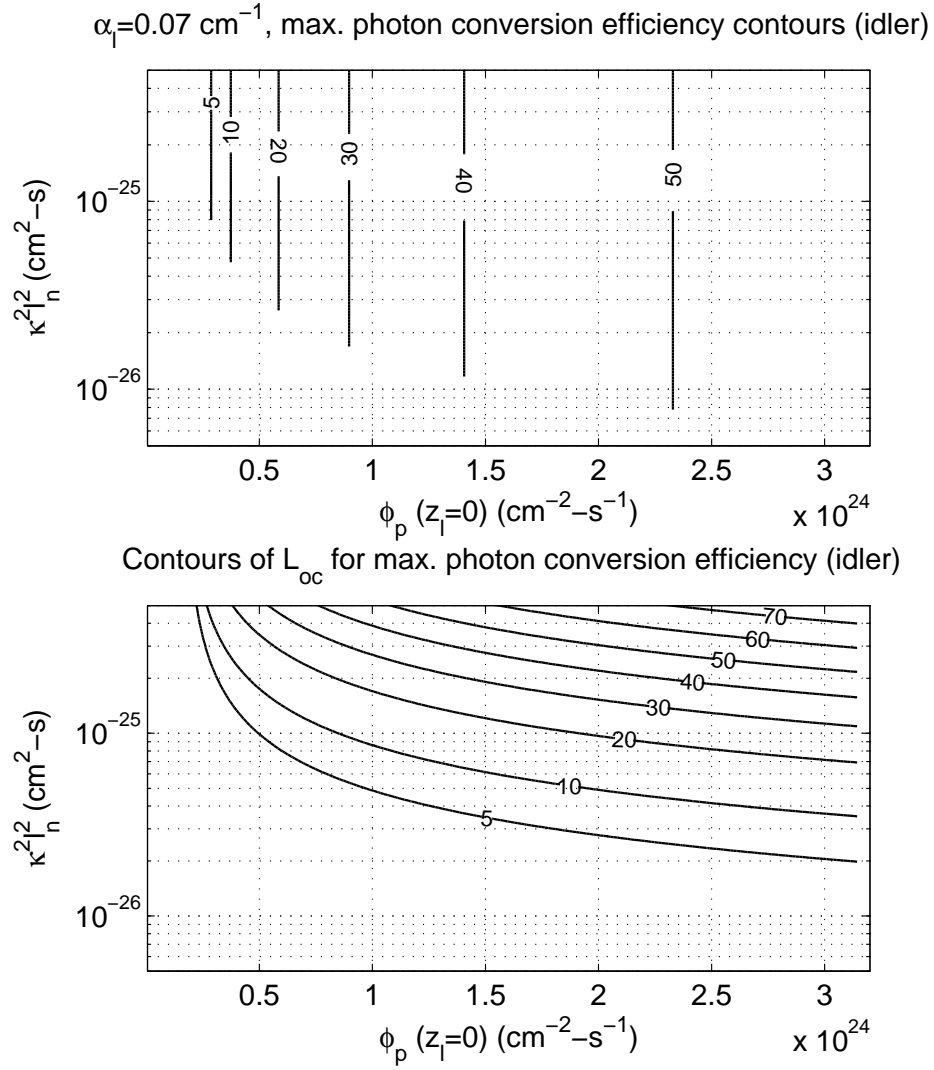


Figure 5.8: Contour plots for the maximum pump-to-idler photon conversion efficiency and the corresponding  $L_{oc}$  as functions of  $\phi_p(z_l = 0)$  and  $\kappa^2 l_n^2$ . For these calculations, in addition to the laser parameters given in Table 5.1,  $\alpha_l = 0.07 \text{ cm}^{-1}$ ,  $\eta_c = 1.0$ , and  $L_s = 2\%$ . In both plots, the values shown on the contours are in percent and in the top plot, only the values corresponding to  $L_{oc} > 0.2\%$  are shown.

# Chapter 6

## Conclusions

In this thesis, we have presented the results of our experiments on nanosecond OPOs and upconversion OPOs that are based on KTA crystals and pumped by a  $Q$ -switched Nd:YAG laser operating at 1064 nm. We have also presented our model for cw IOPOs and results of this model.

In Chapter 3, we have presented the experimental results of our nanosecond OPOs. We used three different KTA crystals with different cut-angles in these experiments: crystal-1, 2, and 3. The highest pump-to-signal energy conversion efficiency obtained in these experiments is 22.9%, which is achieved with the OPO based on crystal-1. Maximum energy conversion efficiencies obtained with the OPOs based on crystal-2 and crystal-3 using the OCs with reflectivities of  $R = 85\%$  and  $R = 74\%$  are 19.5% and 18.2%, respectively. In general, the conversion efficiencies achieved with the OPOs based on crystal-2 and crystal-3 are lower and energy thresholds are higher than those with the OPOs based on crystal-1. Possible reasons for the better performance of the crystal-1 OPO is its slightly larger  $d_{\text{eff}}$  (3.0 pm/V for crystal-1 versus 2.8 pm/V for the other two crystals) due to the larger propagation angle  $\phi$  in this crystal, possible differences in the manufacturing processes used for the crystals, and the slightly larger signal wavelength generated by the crystal-1 OPO ( $\sim 6$  nm larger than the others) and the corresponding change in the cavity residual losses. However, among these factors the change in the  $d_{\text{eff}}$  coefficient is usually the dominant factor and even

a few percent decrease in this coefficient can lead to up to a decrease which is in the order of 10% percent in the output signal energy.

In Chapter 4, we have presented a new technique for highly efficient red beam generation. We have successfully implemented nanosecond SF-OPOs based on KTA crystals that are simultaneously phase matched for optical parametric generation and SFG. The detailed characterization of these devices is presented in terms of their energy output as functions of polarization rotation angle and input pump energy, time profiles, spatial beam profiles, and spectra of the output. In particular, the SF-OPO based on crystal-2 is the first demonstration of a nanosecond upconversion OPO using simultaneous phase matching. This device generates 627 nm pulses with a pulse-width of 10.4 ns and with a pulse energy of 8.3 mJ, corresponding to a 1064-nm-to-627-nm energy conversion efficiency of 21%, when pumped in a single-pass configuration. The double-pass SF-OPO based on crystal-3 generates 627 nm output pulses with a pulse-width of 14.2 ns and with a pulse energy of 5.8 mJ, corresponding to a 1064-nm-to-627-nm energy conversion efficiency of 29%.

There are several advantages associated with our technique for red beam generation. Our devices are simpler in design compared to other devices converting the nanosecond Nd:YAG laser radiation into red wavelengths. With its small size, a typical device can easily be shaped into a module to be placed in front of widely-used Nd:YAG lasers and high energy red pulses can be achieved. Unlike the OPOs based on poled crystals, our devices have energy scalability, hence the energy per pulse of the pump laser can be increased along with the beam size to achieve higher-energy red pulses without reaching the limit for the intensity damage threshold of the KTA crystal. Unlike some OPOs based on PPLN, our devices operate at room temperature and temperature stabilization is not necessary due to the relatively large temperature acceptance bandwidth of KTA. Furthermore, the damage threshold of KTA is larger than most of the widely-used nonlinear crystals. The damage threshold of a KTA crystal is usually set by the damage threshold of the surface coatings, since both the surface and bulk damage thresholds of uncoated KTA are relatively large. Improvements in the surface coating deposition techniques will probably push the limit for the damage

threshold to larger values, thereby making the KTA crystal even more valuable for use at larger pump intensities and energy conversion efficiencies.

In our SF-OPOs, accurate determination of the simultaneous phase-matching angle is essential for achieving high conversion efficiencies. For both SF-OPOs based on crystal-2 and crystal-3, we determined that this angle is quite close to the theoretically predicted value of  $\theta = 90^\circ$  and  $\phi = 30.1^\circ$ . We have also observed that the sum-frequency output is conveniently maximized by adjusting the rotation angle of the intracavity retarder plate inside the cavity. Moreover, the output energy of the device varies rather slowly with a change in the polarization rotation angle at around the optimum. The double-pass pumping scheme proves to be useful for boosting the energy conversion efficiency. In fact, with this pumping scheme, the threshold energy is almost 50% of the value obtained with the single-pass pumping scheme and the energy conversion efficiency is almost 50% larger. For the double-pass pumping scheme, the use of a Faraday isolator for preventing the return pump beam from reaching the pump laser may be necessary if the distance between the pump laser and the SF-OPO is relatively small.

As future work, the device can be manufactured as a monolithic optical device on a single KTA crystal for which the mirrors can be realized by anti-reflection coatings deposited onto the faces of the crystal. A thin retarder plate, whose rotation angle is set beforehand, with one of its faces coated for high reflection and the other for high transmission at the signal wavelength can be attached onto the crystal thereby minimizing the total cavity length and decreasing the energy threshold. Another interesting demonstration would be the cw operation of the device. In this case, the output beam of a cw Nd:YAG laser should be tightly focused into KTA and the cavity mirrors should be selected accordingly to enable the matching between the spatial profiles of the pump and the fundamental cavity modes. Another possible demonstration could be the use of a tunable pump laser and hence obtaining tunable output.

In Chapter 5, we have described our method for modelling cw IOPOs. In this method, unlike the previous models for cw IOPOs, the spatial variation of the resonant fields, intracavity laser and signal, along the direction of propagation is

taken into account. We have shown that the clamping behavior of the intracavity laser power that is predicted by the previous models for cw IOPOs is not valid for high input pump levels and nonlinear crystals with relatively large nonlinearities. Furthermore, the optimization of the output coupling loss at large input pump levels and/or nonlinearities for maximum output signal and idler efficiencies has revealed that optimum output coupling losses can reach large values ( $> 10\%$ ), hence the assumption of the previous models that the OPO cavity has a high finesse also becomes invalid. We have applied our method for OPOs placed internal to the cavities of Ti:sapphire lasers and obtained results which could serve as a guideline when designing IOPOs based on Ti:sapphire lasers for generating the maximum pump-to-signal and pump-to-idler conversion efficiencies for a given nonlinear crystal and at an available input pump power. The method is general and can easily be applied to IOPOs based on other laser crystals. As future work, this method can be modified for modelling IOPOs based on nonlinear crystals that are simultaneously phase-matched for multiple processes.

# Bibliography

- [1] T. H. Maiman, “Stimulated optical radiation in ruby,” *Nature*, vol. 187, pp. 493–494, 1960.
- [2] P. A. Franken, A. E. Hill, C. W. Peters, and G. Weinrich, “Generation of optical harmonics,” *Physical Review Letters*, vol. 7, pp. 118–119, 1961.
- [3] J. Falk, “Instabilities in the doubly resonant parametric oscillator: A theoretical analysis,” *IEEE Journal of Quantum Electronics*, vol. QE-7, pp. 230–235, 1971.
- [4] D. A. Kleinman, “Nonlinear dielectric polarization in optical media,” *Physical Review*, vol. 126, pp. 1977–1979, 1962.
- [5] P. D. Maker, R. W. Terhune, M. Nisenhoff, and C. M. Savage, “Effects of dispersion and focusing on the production of optical harmonics,” *Physical Review Letters*, vol. 8, pp. 21–22, 1962.
- [6] J. A. Armstrong, N. Bloembergen, J. Ducuing, and P. S. Pershan, “Interactions between light waves in a nonlinear dielectric,” *Physical Review*, vol. 127, pp. 1918–1939, 1962.
- [7] R. H. Kingston, “Parametric amplification and oscillation of optical frequencies,” *Proceedings of the Institute of Radio Engineers*, vol. 50, p. 472, 1962.
- [8] N. M. Kroll, “Parametric amplification in spatially extended media and amplification to the design of tuneable oscillators at optical frequencies,” *Physical Review*, vol. 127, pp. 1207–1211, 1962.

- [9] S. A. Akhmanov and R. V. Khokhlov, “Concerning one possibility of amplification of light waves,” *Soviet Physics Journal of Experimental and Theoretical Physics*, vol. 16, pp. 252–254, 1963.
- [10] C. C. Wang and G. W. Racette, “Measurement of parametric gain accompanying optical difference frequency generation,” *Applied Physics Letters*, vol. 6, pp. 169–171, 1965.
- [11] J. A. Giordmaine and R. C. Miller, “Tunable coherent parametric oscillation in  $\text{LiNbO}_3$  at optical frequencies,” *Physical Review Letters*, vol. 14, pp. 973–976, 1965.
- [12] R. G. Smith, J. E. Geusic, H. J. Levinstein, S. Singh, and L. G. van Uitert, “Continuous optical parametric oscillator in  $\text{Ba}_2\text{NaNb}_5\text{O}_{15}$ ,” *Applied Physics Letters*, vol. 13, p. 308, 1968.
- [13] R. L. Byer, M. K. Oshman, J. F. Young, and S. E. Harris, “Visible cw parametric oscillator,” *Applied Physics Letters*, vol. 13, pp. 109–111, 1968.
- [14] M. Yamada, N. Nada, M. Saitoh, and K. Watanabe, “First-order quasi-phase-matched  $\text{LiNbO}_3$  waveguide periodically poled by applying an external electric field for efficient blue second-harmonic generation,” *Applied Physics Letters*, vol. 62, pp. 435–436, 1993.
- [15] W. K. Burns, W. McElhanon, and L. Goldberg, “Second harmonic generation in field poled, quasi-phase-matched, bulk  $\text{LiNbO}_3$ ,” *IEEE Photonics Technology Letters*, vol. 6, pp. 252–254, 1994.
- [16] L. E. Myers, R. C. Eckardt, M. M. Fejer, R. L. Byer, W. R. Bosenberg, and J. W. Pierce, “Quasi-phase-matched optical parametric oscillators in bulk periodically poled  $\text{LiNbO}_3$ ,” *Journal of the Optical Society of America B - Optical Physics*, vol. 12, pp. 2102–2116, 1995.
- [17] R. W. Wallace, “Stable, efficient optical parametric oscillator pumped with doubled Nd:YAG,” *Applied Physics Letters*, vol. 17, pp. 497–499, 1970.
- [18] J. E. Bjorkholm, “Efficient optical parametric oscillation using doubly and singly resonant cavities,” *Applied Physics Letters*, vol. 13, pp. 53–55, 1968.

- [19] L. S. Goldberg, "Optical parametric oscillation in lithium iodate," *Applied Physics Letters*, vol. 17, pp. 489–491, 1970.
- [20] R. L. Herbst and R. L. Byer, "Singly-resonant Cd:Se infrared optical parametric oscillator," *Applied Physics Letters*, vol. 21, pp. 189–191, 1972.
- [21] D. C. Hanna, B. Luther-Davis, and R. C. Smith, "Singly-resonant proustite parametric oscillator tuned from 1.22 to 8.5  $\mu\text{m}$ ," *Applied Physics Letters*, vol. 22, pp. 440–442, 1973.
- [22] Y. X. Fan, R. C. Eckardt, R. L. Byer, R. K. Route, and R. S. Feigelson, "AgGaS<sub>2</sub> infrared optical parametric oscillator," *Applied Physics Letters*, vol. 45, pp. 313–315, 1984.
- [23] L. K. Cheng, W. R. Bosenberg, and C. L. Tang, "Broadly tunable optical parametric oscillation in  $\beta\text{-BaB}_2\text{O}_4$ ," *Applied Physics Letters*, vol. 53, pp. 175–177, 1988.
- [24] Y. X. Fan, R. C. Eckardt, R. L. Byer, J. Nolting, and R. Wallenstein, "Visible BaB<sub>2</sub>O<sub>4</sub> optical parametric oscillator pumped at 355 nm by a single-axial-mode pulsed source," *Applied Physics Letters*, vol. 53, pp. 2014–2016, 1988.
- [25] A. Fix, T. Schröder, and R. Wallenstein, "The optical parametric oscillators of beta-barium borate and lithium triborate: new sources of powerful tunable laser radiation in the ultraviolet, visible and near infrared," *Laser Optoelektronik*, vol. 23, pp. 106–110, 1991.
- [26] C. L. Tang, W. R. Bosenberg, T. Ukachi, R. J. Lane, and L. K. Cheng, "Optical parametric oscillators," *Proceedings of the IEEE*, vol. 80, pp. 365–374, 1992.
- [27] A. Fix, T. Schröder, R. Wallenstein, J. G. Haub, M. J. Johnson, and B. J. Orr, "Tunable  $\beta$ -barium borate optical parametric oscillator: operating characteristics with and without injection seeding," *Journal of the Optical Society of America B - Optical Physics*, vol. 10, pp. 1744–1750, 1993.

- [28] H. Komine, "Optical parametric oscillation in a beta-barium borate crystal pumped by an XeCl excimer laser," *Optics Letters*, vol. 13, pp. 643–645, 1988.
- [29] M. Ebrahimzadeh, A. J. Henderson, and M. H. Dunn, "An excimer-pumped  $\beta$ -BaB<sub>2</sub>O<sub>4</sub> optical parametric oscillator tunable from 354 nm to 2.370  $\mu$ m," *IEEE Journal of Quantum Electronics*, vol. 26, pp. 1241–1252, 1990.
- [30] Y. Cui, D. E. Withers, C. F. Rae, C. J. Norrie, Y. Tang, B. D. Sinclair, W. Sibbett, and M. H. Dunn, "Widely tunable all-solid-state optical parametric oscillator for the visible and near infrared," *Optics Letters*, vol. 18, pp. 122–124, 1993.
- [31] D. E. Withers, G. Robertson, A. J. Henderson, Y. Tang, Y. Cui, W. Sibbett, B. D. Sinclair, and M. H. Dunn, "Comparison of lithium triborate and  $\beta$ -barium borate as nonlinear media for optical parametric oscillators," *Journal of the Optical Society of America B - Optical Physics*, vol. 10, pp. 1737–1743, 1993.
- [32] K. Kato, "Parametric oscillation at 3.2  $\mu$ m in KTP pumped at 1.064  $\mu$ m," *IEEE Journal of Quantum Electronics*, vol. 27, pp. 1137–1140, 1991.
- [33] L. R. Marshall, J. Kasinski, A. D. Hays, and R. L. Burnham, "Efficient optical parametric oscillation at 1.6  $\mu$ m," *Optics Letters*, vol. 16, pp. 681–683, 1991.
- [34] W. R. Bosenberg, L. K. Cheng, and J. D. Bierlein, "Optical parametric frequency conversion properties of KTiOAsO<sub>4</sub>," *Applied Physics Letters*, vol. 65, pp. 2765–2767, 1994.
- [35] L. E. Myers and W. R. Bosenberg, "Periodically poled lithium niobate and quasi-phase-matched optical parametric oscillators," *IEEE Journal of Quantum Electronics*, vol. 33, pp. 1663–1672, 1997.
- [36] U. Bäder, J.-P. Meyn, J. Bartschke, T. Weber, A. Borsutzky, R. Wallenstein, R. G. Batchko, M. M. Fejer, and R. L. Byer, "Nanosecond periodically poled lithium niobate optical parametric generator pumped at 532 nm

- by a single-frequency passively  $Q$ -switched Nd:YAG laser,” *Optics Letters*, vol. 24, pp. 1608–1610, 1999.
- [37] J. Hellstrom, V. Pasiskevicius, F. Laurell, and H. Karlsson, “Efficient nanosecond optical parametric oscillators based on periodically poled KTP emitting in the 1.8-2.5  $\mu\text{m}$  spectral range,” *Optics Letters*, vol. 24, pp. 1233–1235, 1999.
- [38] V. Pasiskevicius, H. Karlsson, F. Laurell, R. Butkus, V. Smilgevičius, and A. Piskarskas, “High-efficiency parametric oscillation and spectral control in the red spectral region with periodically poled  $\text{KTiOPO}_4$ ,” *Optics Letters*, vol. 26, pp. 710–712, 2001.
- [39] H. Ishizuki, I. Shoji, and T. Taira, “High-energy quasi-phase-matched optical parametric oscillation in a 3-mm-thick periodically poled  $\text{MgO:LiNbO}_3$  device,” *Optics Letters*, vol. 29, pp. 2527–2529, 2004.
- [40] J. Hellstrom, V. Pasiskevicius, H. Karlsson, and F. Laurell, “High-power optical parametric oscillation in large-aperture periodically poled  $\text{KTiOPO}_4$ ,” *Optics Letters*, vol. 25, pp. 174–176, 2000.
- [41] H. Karlsson, M. Olson, G. Arvidsson, F. Laurell, U. Bader, A. Borsutzky, R. Wallenstein, S. Wickstrom, and M. Gustafsson, “Nanosecond optical parametric oscillator based on large-aperture periodically poled  $\text{RbTiOAsO}_4$ ,” *Optics Letters*, vol. 24, pp. 330–332, 1999.
- [42] R. L. Byer and A. Piskarskas, eds., “Optical parametric oscillation and amplification,” *Journal of the Optical Society of America B - Optical Physics*, vol. 10, pp. 1656–1791, 2148–2243, 1993.
- [43] W. R. Bosenberg and R. C. Eckardt, eds., “Optical parametric devices,” *Journal of the Optical Society of America B - Optical Physics*, vol. 12, pp. 2084–2322, 1995.
- [44] M. Ebrahimzadeh, R. C. Eckardt, and M. H. Dunn, eds., “Optical parametric devices and processes,” *Journal of the Optical Society of America B - Optical Physics*, vol. 16, pp. 1477–1602, 1999.

- [45] M. Bass, J. M. Enoch, E. W. van Stryland, and W. L. Wolfe, eds., *Handbook of Optics: Fiber Optics and Nonlinear Optics*. McGraw-Hill, 2001, vol. 4.
- [46] R. A. Andrews, H. Rabin, and C. L. Tang, “Coupled parametric down-conversion and upconversion with simultaneous phase matching,” *Physical Review Letters*, vol. 25, pp. 605–608, 1970.
- [47] V. Petrov and F. Noack, “Frequency upconversion of tunable femtosecond pulses by parametric amplification and sum-frequency generation in a single nonlinear crystal,” *Optics Letters*, vol. 20, pp. 2171–2173, 1995.
- [48] T. Kartaloğlu, K. G. Köprülü, and O. Aytür, “Phase-matched self-doubling optical parametric oscillator,” *Optics Letters*, vol. 22, pp. 280–282, 1997.
- [49] T. Kartaloğlu and O. Aytür, “Femtosecond self-doubling optical parametric oscillator based on  $\text{KTiOAsO}_4$ ,” *IEEE Journal of Quantum Electronics*, vol. 39, pp. 65–67, 2003.
- [50] T. Kartaloğlu, Z. G. Figen, and O. Aytür, “A self-doubling optical parametric oscillator based on aperiodically-poled lithium niobate,” in *2001 IEEE/LEOS Annual Meeting Conference Proceedings*. Institute of Electrical and Electronics Engineers, Piscataway, NJ, 2001, pp. 243–244.
- [51] T. Kartaloğlu, Z. G. Figen, and O. Aytür, “Simultaneous phase matching of optical parametric oscillation and second-harmonic generation in aperiodically poled lithium niobate,” *Journal of the Optical Society of America B - Optical Physics*, vol. 20, pp. 343–350, 2003.
- [52] Z. G. Figen and O. Aytür, “Simultaneous optical parametric oscillation and sum-frequency generation within a single crystal for converting 1064 nm into 627 nm,” in *International Conference on Quantum Electronics and the Pacific Rim Conference on Lasers and Electro-Optics*. IEEE Lasers and Electro-Optics Society and Optical Society of America, Tokyo, 2005, paper no. CFI3-3.
- [53] Z. G. Figen and O. Aytür, “Nanosecond sum-frequency generating optical parametric oscillator using simultaneous phase matching,” *Optics Express*, vol. 13, pp. 4896–4902, 2005.

- [54] C. McGowan, D. T. Reid, Z. E. Penman, M. Ebrahimzadeh, W. Sibbett, and D. H. Jundt, “Femtosecond optical parametric oscillator based on periodically poled lithium niobate,” *Journal of the Optical Society of America B - Optical Physics*, vol. 15, pp. 694–701, 1998.
- [55] X. Zhang, J. Hebling, J. Kuhl, W. W. Rühle, L. Palfalvi, and H. Giessen, “Femtosecond near-IR optical parametric oscillator with efficient intracavity generation of visible light,” *Journal of the Optical Society of America B - Optical Physics*, vol. 19, pp. 2479–2488, 2002.
- [56] S. D. Butterworth, P. G. R. Smith, and D. C. Hanna, “Picosecond Ti:sapphire-pumped optical parametric oscillator based on periodically poled LiNbO<sub>3</sub>,” *Optics Letters*, vol. 22, pp. 618–620, 1997.
- [57] K. G. Köprülü, T. Kartaloğlu, Y. Dikmelik, and O. Aytür, “Single-crystal sum-frequency-generating optical parametric oscillator,” *Journal of the Optical Society of America B - Optical Physics*, vol. 16, pp. 1546–1552, 1999.
- [58] O. Aytür and Y. Dikmelik, “Plane-wave theory of self-doubling optical parametric oscillators,” *IEEE Journal of Quantum Electronics*, vol. 34, pp. 447–458, 1998.
- [59] Y. Dikmelik, G. Akgün, and O. Aytür, “Plane-wave dynamics of optical parametric oscillation with simultaneous sum-frequency generation,” *IEEE Journal of Quantum Electronics*, vol. 35, pp. 897–912, 1999.
- [60] G. T. Moore, K. Koch, M. E. Dearborn, and M. Vaidyanathan, “A simultaneously phase-matched tandem optical parametric oscillator,” *IEEE Journal of Quantum Electronics*, vol. 34, pp. 803–810, 1998.
- [61] K. C. Burr, C. L. Tang, M. A. Arbore, and M. M. Fejer, “High-repetition-rate femtosecond optical parametric oscillator based on periodically poled lithium niobate,” *Applied Physics Letters*, vol. 70, pp. 3341–3343, 1997.
- [62] O. Pfister, J. S. Wells, L. Hollberg, L. Zink, D. A. V. Baak, M. D. Levenson, and W. R. Bosenberg, “Continuous-wave frequency tripling and quadrupling by simultaneous three-wave mixings in periodically poled crystals:

- application to a two-step 1.19–10.71- $\mu\text{m}$  frequency bridge,” *Optics Letters*, vol. 22, pp. 1211–1213, 1997.
- [63] D.-W. Chen and K. Masters, “Continuous-wave 4.3- $\mu\text{m}$  intracavity difference frequency generation in an optical parametric oscillator,” *Optics Letters*, vol. 26, pp. 25–27, 2001.
- [64] G. Z. Luo, S. N. Zhu, J. L. He, Y. Y. Zhu, H. T. Wang, Z. W. Liu, C. Zhang, and N. B. Ming, “Simultaneously efficient blue and red light generations in a periodically poled  $\text{LiTaO}_3$ ,” *Applied Physics Letters*, vol. 78, pp. 3006–3008, 2001.
- [65] J. Feng, Y. Y. Zhu, and N. B. Ming, “Harmonic generations in an optical Fibonacci superlattice,” *Physical Review B*, vol. 41, pp. 5578–5582, 1990.
- [66] S. N. Zhu, Y. Y. Zhu, and N. B. Ming, “Quasi-phase-matched third-harmonic generation in a quasi-periodic optical superlattice,” *Science*, vol. 278, pp. 843–846, 1997.
- [67] S. N. Zhu, Y. Y. Zhu, Y. Q. Qin, H. F. Wang, C. Z. Ge, and N. B. Ming, “Experimental realization of second harmonic generation in a Fibonacci optical superlattice of  $\text{LiTaO}_3$ ,” *Physical Review Letters*, vol. 78, pp. 2752–2755, 1997.
- [68] Y. Y. Zhu, R. F. Xiao, J. S. Fu, G. K. L. Wong, and N. B. Ming, “Third harmonic generation through coupled second-order nonlinear optical parametric processes in quasiperiodically domain-inverted  $\text{Sr}_{0.6}\text{Ba}_{0.4}\text{Nb}_2\text{O}_6$  optical superlattices,” *Applied Physics Letters*, vol. 73, pp. 432–434, 1998.
- [69] X. Liu, Z. Wang, J. Wu, and N. Ming, “Characterization of third-harmonic generation in Fibonacci optical superlattices,” *Physical Review A*, vol. 58, pp. 4956–4960, 1998.
- [70] Y. Q. Qin, Y. Y. Zhu, S. N. Zhu, G. P. Luo, J. Ma, and N. B. Ming, “Nonlinear optical characterization of a generalized Fibonacci optical superlattice,” *Applied Physics Letters*, vol. 75, pp. 448–450, 1999.

- [71] Y. B. Chen, Y. Y. Zhu, Y. Q. Qin, C. Zhang, S. N. Zhu, and N. B. Ming, "Second-harmonic and third-harmonic generation in a three-component Fibonacci optical superlattice," *Journal of Physics: Condensed Matter*, vol. 12, pp. 529–537, 2000.
- [72] Y. B. Chen, C. Zhang, Y. Y. Zhu, S. N. Zhu, H. T. Wang, and N. B. Ming, "Optical harmonic generation in a quasi-phase-matched three-component Fibonacci superlattice LiTaO<sub>3</sub>," *Applied Physics Letters*, vol. 78, pp. 577–579, 2001.
- [73] Y. Y. Zhu and N. B. Ming, "Dielectric superlattices for nonlinear optical effects," *Optical and Quantum Electronics*, vol. 31, pp. 1093–1128, 1999.
- [74] K. F. Kashi and A. Arie, "Multiple-wavelength quasi-phase-matched nonlinear interactions," *IEEE Journal of Quantum Electronics*, vol. 35, pp. 1649–1656, 1999.
- [75] K. F. Kashi, A. Arie, P. Urenski, and G. Rosenman, "Multiple nonlinear optical interactions with arbitrary wave vector differences," *Physical Review Letters*, vol. 88, p. art. no. 023903, 2002.
- [76] C. Zhang, H. Wei, Y. Y. Zhu, H. T. Wang, S. N. Zhu, and N. B. Ming, "Third-harmonic generation in a general two-component quasi-periodic optical superlattice," *Optics Letters*, vol. 26, pp. 899–901, 2001.
- [77] B. Y. Gu, B. Z. Dong, Y. Zhang, and G. Z. Yang, "Enhanced harmonic generation in aperiodic optical superlattices," *Applied Physics Letters*, vol. 75, pp. 2175–2177, 1999.
- [78] B. Y. Gu, Y. Zhang, and B. Z. Dong, "Investigations of harmonic generations in aperiodic optical superlattices," *Journal of Applied Physics*, vol. 87, pp. 7629–7637, 2000.
- [79] Y. Zhang and B. Y. Gu, "Optimal design of aperiodically poled lithium niobate crystals for multiple wavelengths parametric amplification," *Optics Communications*, vol. 192, pp. 417–425, 2001.

- [80] H. Liu, Y. Y. Zhu, S. N. Zhu, C. Zhang, and N. B. Ming, "Aperiodic optical superlattices engineered for optical frequency conversion," *Applied Physics Letters*, vol. 79, pp. 728–730, 2001.
- [81] J. Liao, J. L. He, H. Liu, H. T. Wang, S. N. Zhu, Y. Y. Zhu, and N. B. Ming, "Simultaneous generation of red, green, and blue quasi-continuous-wave coherent radiation based on multiple quasi-phase-matched interactions from a single, aperiodically-poled LiTaO<sub>3</sub>," *Applied Physics Letters*, vol. 82, pp. 3159–3161, 2003.
- [82] J. L. He, J. Liao, H. Liu, J. Du, F. Xu, H. T. Wang, S. N. Zhu, Y. Y. Zhu, and N. B. Ming, "Simultaneous cw red, yellow, and green light generation, "traffic signal lights," by frequency doubling and sum-frequency mixing in an aperiodically-poled LiTaO<sub>3</sub>," *Applied Physics Letters*, vol. 83, pp. 228–230, 2003.
- [83] J. Liao, J. L. He, H. Liu, J. Du, F. Xu, H. T. Wang, S. N. Zhu, Y. Y. Zhu, and N. B. Ming, "Red, yellow, green, and blue-four-color light from a single, aperiodically-poled LiTaO<sub>3</sub> crystal," *Applied Physics B: Lasers and Optics*, vol. 78, pp. 265–267, 2004.
- [84] T. W. Ren, J. L. He, C. Zhang, S. N. Zhu, Y. Y. Zhu, and Y. Hang, "Simultaneous generation of three primary colors using aperiodically-poled LiTaO<sub>3</sub>," *Journal of Physics: Condensed Matter*, vol. 16, pp. 3289–3294, 2004.
- [85] H. X. Li, P. Xu, Y. A. Fan, P. Lu, Z. D. Gao, S. Liu, S. N. Zhu, and J. L. He, "All-solid-state red and green laser by temperature tuning," *Journal of Physics D: Applied Physics*, vol. 37, pp. L21–L24, 2004.
- [86] D. Botez and D. R. Scifres, eds., *Diode Laser Arrays*. Cambridge University Press, 1994.
- [87] G. J. Hall and A. I. Ferguson, "Generation of single-frequency radiation at 1064, 1319, and 659.5 nm with an all-solid-state, out-of-plane Nd:YAG ring laser," *Optics Letters*, vol. 19, pp. 557–559, 1994.

- [88] Y. Inoue, S. Konno, T. Kojima, and S. Fujikawa, "High-power red beam generation by frequency-doubling of a Nd:YAG laser," *IEEE Journal of Quantum Electronics*, vol. 35, pp. 1737–1740, 1999.
- [89] Z. Sun, R. Li, Y. Bi, X. Yang, Y. Bo, Y. Zhang, G. Wang, W. Zhao, H. Zhang, W. Hou, D. Cui, and Z. Xu, "Generation of 11.5 W coherent red-light by intra-cavity frequency-doubling of a side-pumped Nd:YAG laser in a 4-cm LBO," *Optics Communications*, vol. 241, pp. 167–172, 2004.
- [90] J. R. Lincoln and A. I. Ferguson, "All-solid-state intracavity-doubled Nd:YLF laser producing 300 mw of 659-nm light," *Optics Letters*, vol. 19, pp. 1213–1215, 1994.
- [91] G. R. Morrison, M. Ebrahimzadeh, C. F. Rae, and M. H. Dunn, "Diode-pumped, Q-switched, 1.321  $\mu\text{m}$  Nd:YLF laser and its frequency doubling," *Optics Communications*, vol. 118, pp. 55–60, 1995.
- [92] A. Agnesi, A. Guandalini, and G. Reali, "Efficient 671-nm pump source by intracavity doubling of a diode-pumped Nd:YVO<sub>4</sub> laser," *Journal of the Optical Society of America B - Optical Physics*, vol. 19, pp. 1078–1082, 2002.
- [93] H. Ogilvy, M. J. Withford, P. Dekker, and J. A. Piper, "Efficient diode double-end-pumped Nd:YVO<sub>4</sub> laser operating at 1342 nm," *Optics Express*, vol. 11, pp. 2411–2415, 2003.
- [94] A. Agnesi, A. Guandalini, G. Reali, S. Dell'Acqua, and G. Piccinno, "High-brightness 2.4-W continuous-wave Nd:GdVO<sub>4</sub> laser at 670 nm," *Optics Letters*, vol. 29, pp. 56–58, 2004.
- [95] C. Du, S. Ruan, Y. Yu, and F. Zeng, "6-W diode-end-pumped Nd:GdVO<sub>4</sub>/LBO quasi-continuous-wave red laser at 671 nm," *Optics Express*, vol. 13, pp. 2013–2018, 2005.
- [96] W. R. Bosenberg, L. K. Cheng, and C. L. Tang, "Ultraviolet optical parametric oscillation in  $\beta$ -BaB<sub>2</sub>O<sub>4</sub>," *Applied Physics Letters*, vol. 54, pp. 13–15, 1989.

- [97] W. R. Bosenberg, J. I. Alexander, L. E. Myers, and R. W. Wallace, “2.5-W, continuous-wave, 629-nm solid-state laser source,” *Optics Letters*, vol. 23, pp. 207–209, 1998.
- [98] B. Ruffing, A. Nebel, and R. Wallenstein, “High-power picosecond  $\text{LiB}_3\text{O}_5$  optical parametric oscillators tunable in the blue spectral range,” *Applied Physics B: Lasers and Optics*, vol. 72, pp. 137–149, 2001.
- [99] T. Sandrock, H. Scheife, E. Heumann, and G. Huber, “High-power continuous-wave upconversion fiber laser at room temperature,” *Optics Letters*, vol. 22, pp. 808–810, 1997.
- [100] P. Xie and T. R. Gosnell, “Room-temperature upconversion fiber laser tunable in the red, orange, green, and blue spectral regions,” *Optics Letters*, vol. 20, pp. 1014–1016, 1995.
- [101] P. A. Champert, S. V. Popov, M. A. Solodyankin, and J. R. Taylor, “1.4-W red generation by frequency mixing of seeded Yb and Er fiber amplifiers,” *IEEE Photonics Technology Letters*, vol. 14, pp. 1680–1682, 2002.
- [102] A. Sennaroglu, C. R. Pollock, and H. Nathel, “Generation of tunable femtosecond pulses in the 1.21–1.27  $\mu\text{m}$  and 605–635 nm wavelength region by using a regeneratively initiated self-mode-locked Cr:forsterite laser,” *IEEE Journal of Quantum Electronics*, vol. 30, pp. 1851–1861, 1994.
- [103] D. Jaque, J. A. Sanz-García, J. Capmany, and J. G. Solé, “Continuous wave laser radiation at 693 nm from  $\text{LiNbO}_3:\text{ZnO}:\text{Nd}^{3+}$  nonlinear laser crystal,” *Applied Physics B: Lasers and Optics*, vol. 70, pp. 483–486, 2000.
- [104] A. Yalabık, “A numerical solution for nanosecond single crystal upconversion optical parametric oscillators,” Master’s thesis, Bilkent University, 2005.
- [105] R. W. Boyd, *Nonlinear Optics*. Academic Press, 1992.
- [106] R. A. Baumgartner and R. L. Byer, “Optical parametric amplification,” *IEEE Journal of Quantum Electronics*, vol. QE-15, pp. 432–444, 1979.

- [107] G. T. Moore and K. Koch, "Optical parametric oscillation with intracavity sum-frequency generation," *IEEE Journal of Quantum Electronics*, vol. 29, pp. 961–969, 1993.
- [108] M. Abramowitz and I. A. Stegun, eds., *Handbook of Mathematical Functions with Formulas, Graphs, and Mathematical Tables*. Dover, 1965.
- [109] E. C. Cheung, K. Koch, and G. T. Moore, "Frequency upconversion by phase-matched sum-frequency generation in an optical parametric oscillator," *Optics Letters*, vol. 19, pp. 1967–1969, 1994.
- [110] D. T. Reid, M. Ebrahimzadeh, and W. Sibbett, "Efficient femtosecond pulse generation in the visible in a frequency-doubled optical parametric oscillator based on RbTiOAsO<sub>4</sub>," *Journal of the Optical Society of America B - Optical Physics*, vol. 12, pp. 1157–1163, 1995.
- [111] V. G. Dmitriev, G. G. Gurzadyan, and D. N. Nikogosyan, *Handbook of Nonlinear Optical Crystals*. Springer-Verlag, 1999.
- [112] B. E. A. Saleh and M. C. Teich, *Fundamentals of Photonics*. John-Wiley & Sons, 1991.
- [113] J. Yao, W. Sheng, and W. Shi, "Accurate calculation of the optimum phase-matching parameters in three-wave interactions with biaxial nonlinear-optical crystals," *Journal of the Optical Society of America B - Optical Physics*, vol. 9, pp. 891–902, 1992.
- [114] G. J. Zhang, S. Horinouchi, T. Kinoshita, and K. Sasaki, "Theoretical analysis of the spatial phase-matching loci for second-harmonic generation and multiwave-mixing interactions," *Applied Optics*, vol. 34, pp. 5301–5311, 1995.
- [115] M. M. Fejer, G. A. Magel, D. H. Jundt, and R. L. Byer, "Quasi-phase-matched second harmonic generation: tuning and tolerances," *IEEE Journal of Quantum Electronics*, vol. 28, pp. 2631–2654, 1992.

- [116] J. D. Bierlein, H. Vanherzeele, and A. A. Ballman, "Linear and nonlinear optical properties of flux-grown  $\text{KTiOAsO}_4$ ," *Applied Physics Letters*, vol. 54, pp. 783–785, 1989.
- [117] G. Hansson, H. Karlsson, S. Wang, and F. Laurell, "Transmission measurements in KTP and isomorphic compounds," *Applied Optics*, vol. 39, pp. 5058–5069, 2000.
- [118] M. S. Webb, P. F. Moulton, J. J. Kasinski, R. L. Burnham, G. Loiacono, and R. Stolzenberger, "High-average-power  $\text{KTiOAsO}_4$  optical parametric oscillator," *Optics Letters*, vol. 23, pp. 1161–1163, 1998.
- [119] R. F. Wu, K. S. Lai, H. F. Wong, W. J. Xie, Y. L. Lim, and E. Lau, "Multiwatt mid-IR output from a Nd:YALO laser pumped intracavity KTA OPO," *Optics Express*, vol. 8, pp. 694–698, 2001.
- [120] S. C.-Blanc, A. Ivanov, D. Lupinski, and E. Freysz, " $\text{KTiOPO}_4$ ,  $\text{KTiOAsO}_4$ , and  $\text{KNbO}_3$  crystals for mid-infrared femtosecond optical parametric amplifiers: analysis and comparison," *Applied Physics B: Lasers and Optics*, vol. 70, pp. S247–S252, 2000.
- [121] C. McGowan, D. T. Reid, M. Ebrahimzadeh, and W. Sibbett, "Femtosecond pulses tunable beyond  $4 \mu\text{m}$  from a KTA-based optical parametric oscillator," *Optics Communications*, vol. 134, pp. 186–190, 1997.
- [122] K. Kato, "Second-harmonic and sum-frequency generation in  $\text{KTiOAsO}_4$ ," *IEEE Journal of Quantum Electronics*, vol. 30, pp. 881–883, 1994.
- [123] L. K. Cheng, L.-T. Cheng, J. D. Bierlein, F. C. Zumsteg, and A. A. Ballman, "Properties of doped and undoped crystals of single domain  $\text{KTiOAsO}_4$ ," *Applied Physics Letters*, vol. 62, pp. 346–348, 1993.
- [124] L. K. Cheng, L. T. Cheng, J. Galperin, P. A. M. Hotsenpiller, and J. D. Bierlein, "Crystal growth and characterization of  $\text{KTiOPO}_4$  isomorphs from the self-fluxes," *Journal of Crystal Growth*, vol. 137, pp. 107–115, 1994.
- [125] B. Boulanger, J.-P. Fève, G. Marnier, and B. Ménaert, "Methodology for optical studies of nonlinear crystals: application to the isomorph family

- KTiOPO<sub>4</sub>, KTiOAsO<sub>4</sub>, RbTiOAsO<sub>4</sub>, and CsTiOAsO<sub>4</sub>,” *Pure Applied Optics*, vol. 7, pp. 239–256, 1998.
- [126] W. J. Alford and A. V. Smith, “Wavelength variation of the second-order nonlinear coefficients of KNbO<sub>3</sub>, KTiOPO<sub>4</sub>, KTiOAsO<sub>4</sub>, LiNbO<sub>3</sub>, LiIO<sub>3</sub>,  $\beta$ -BaB<sub>2</sub>O<sub>4</sub>, KH<sub>2</sub>PO<sub>4</sub>, and LiB<sub>3</sub>O<sub>5</sub> crystals: a test of Miller wavelength scaling,” *Journal of the Optical Society of America B - Optical Physics*, vol. 18, pp. 524–533, 2001.
- [127] M. V. Pack, D. J. Armstrong, and A. V. Smith, “Measurement of the  $\chi^{(2)}$  tensors of KTiOPO<sub>4</sub>, KTiOAsO<sub>4</sub>, RbTiOPO<sub>4</sub>, and RbTiOAsO<sub>4</sub> crystals,” *Applied Optics*, vol. 43, pp. 3319–3323, 2004.
- [128] D. A. Roberts, “Simplified characterization of uniaxial and biaxial nonlinear optical crystals: a plea for standardization of nomenclature and conventions,” *IEEE Journal of Quantum Electronics*, vol. 28, pp. 2057–2074, 1992.
- [129] D. L. Fenimore, K. L. Schepler, U. B. Ramabadran, and S. R. McPherson, “Infrared corrected sellmeier coefficients for potassium titanyl arsenate,” *Journal of the Optical Society of America B - Optical Physics*, vol. 12, pp. 794–796, 1995.
- [130] K. Kato, N. Umemura, and E. Tanaka, “90° phase-matched mid-infrared parametric oscillation in undoped KTiOAsO<sub>4</sub>,” *Japanese Journal of Applied Physics*, vol. 36, pp. L403–L405, 1997.
- [131] J.-P. Fève, B. Boulanger, O. Pacaud, I. Rousseau, B. Ménaert, G. Marnier, P. Villeval, C. Bonnin, G. M. Loiacono, and D. N. Loiacono, “Phase-matching measurements and Sellmeier equations over the complete transparency range of KTiOAsO<sub>4</sub>, RbTiOAsO<sub>4</sub>, and CsTiOAsO<sub>4</sub>,” *Journal of the Optical Society of America B - Optical Physics*, vol. 17, pp. 775–780, 2000.
- [132] S. J. Brosnan and R. L. Byer, “Optical parametric oscillator threshold and linewidth studies,” *IEEE Journal of Quantum Electronics*, vol. QE-15, pp. 415–431, 1979.

- [133] G. Arisholm, “Quantum noise initiation and macroscopic fluctuations in optical parametric oscillators,” *Journal of the Optical Society of America B - Optical Physics*, vol. 16, pp. 117–127, 1999.
- [134] G. Arisholm and K. Stenersen, “Optical parametric oscillator with non-ideal mirrors and single- and multi-mode pump beams,” *Optics Express*, vol. 4, pp. 183–192, 1999.
- [135] S. T. Yang, R. C. Eckardt, and R. L. Byer, “Power and spectral characteristics of continuous-wave parametric oscillators: The doubly to singly resonant transition,” *Journal of the Optical Society of America B - Optical Physics*, vol. 10, pp. 1684–1695, 1993.
- [136] F. Bréhat and B. Wyncke, “Calculation of double-refraction walk-off angle along the phase-matching directions in nonlinear biaxial crystals,” *Journal of Physics B: Atomic, Molecular, and Optical Physics*, vol. 22, pp. 1891–1898, 1989.
- [137] T. Debuisschert, J. Raffy, J.-M. Dupont, and J.-P. Pocholle, “Nanosecond optical parametric oscillators,” *Comptes Rendus de l’Academie des Sciences Serie IV Physique Astrophysique*, vol. 1, pp. 561–583, 2000.
- [138] W. Koechner, *Solid-State Laser Engineering*. Springer-Verlag, 1996.
- [139] S. Guha, F.-J. Wu, and J. Falk, “The effects of focusing on parametric oscillation,” *IEEE Journal of Quantum Electronics*, vol. QE-18, pp. 907–912, 1982.
- [140] J. A. C. Terry, Y. Cui, Y. Yang, W. Sibbett, and M. H. Dunn, “Low-threshold operation of all-solid-state KTP optical parametric oscillator,” *Journal of the Optical Society of America B - Optical Physics*, vol. 11, pp. 758–769, 1994.
- [141] J. M. Breteau, C. Jourdain, T. Lepine, and F. Simon, “Numerical simulation and realization of a KTP optical parametric oscillator,” in *OSA Proceedings on Advanced Solid-State Lasers*, vol. 20. Optical Society of America, Washington, D.C., 1993, pp. 118–120.

- [142] A. V. Smith, W. J. Alford, T. D. Raymond, and M. S. Bowers, “Comparison of a numerical model with measured performance of a seeded, nanosecond KTP optical parametric oscillator,” *Journal of the Optical Society of America B - Optical Physics*, vol. 12, pp. 2253–2267, 1995.
- [143] R. Urschel, A. Borsutzky, and R. Wallenstein, “Numerical analysis of the spatial behaviour of nanosecond optical parametric oscillators of beta-barium borate,” *Applied Physics B: Lasers and Optics*, vol. 70, pp. 203–210, 2000.
- [144] G. Anstett, M. Nittmann, and R. Wallenstein, “Experimental investigation and numerical simulation of the spatio-temporal dynamics of the light-pulses in nanosecond optical parametric oscillators,” *Applied Physics B: Lasers and Optics*, vol. 79, pp. 305–313, 2004.
- [145] E. S. Cassedy and M. Jain, “A theoretical study of injection tuning of optical parametric oscillators,” *IEEE Journal of Quantum Electronics*, vol. QE-15, pp. 1290–1301, 1979.
- [146] K.-J. Boller and T. Schroder, “Demonstration of broadband intracavity spectroscopy in a pulsed optical parametric oscillator made of  $\beta$ -barium borate,” *Journal of the Optical Society of America B - Optical Physics*, vol. 10, pp. 1778–1784, 1993.
- [147] Y. Kong, Z. Xu, Y. Zhou, D. Deng, X. Zhu, and L. Wu, “The compound cavity optical parametric oscillator: theory and experiment,” *IEEE Journal of Quantum Electronics*, vol. 34, pp. 439–446, 1998.
- [148] A. Fix and R. Wallenstein, “Spectral properties of pulsed nanosecond optical parametric oscillators: experimental investigation and numerical analysis,” *Journal of the Optical Society of America B - Optical Physics*, vol. 13, pp. 2484–2497, 1996.
- [149] A. V. Smith, R. J. Gehr, and M. S. Bowers, “Numerical models of broadband nanosecond optical parametric oscillators,” *Journal of the Optical Society of America B - Optical Physics*, vol. 16, pp. 609–619, 1999.

- [150] A. Yariv and W. H. Louisell, "Theory of the optical parametric oscillator," *IEEE Journal of Quantum Electronics*, vol. QE-2, pp. 418–424, 1966.
- [151] W. H. Press, B. P. Flannery, S. A. Teukolsky, and W. T. Vetterling, *Numerical Recipes*. Cambridge University Press, 1992.
- [152] R. L. Byer and S. E. Harris, "Power and bandwidth of spontaneous parametric emission," *Physical Review*, vol. 168, pp. 1064–1068, 1968.
- [153] M. Ebrahimzadeh, G. A. Turnbull, T. J. Edwards, D. J. M. Stothard, I. D. Lindsay, and M. H. Dunn, "Intracavity continuous-wave singly resonant optical parametric oscillators," *Journal of the Optical Society of America B - Optical Physics*, vol. 16, pp. 1499–1511, 1999.
- [154] F. G. Colville, M. H. Dunn, and M. Ebrahimzadeh, "Continuous-wave, singly resonant, intracavity parametric oscillator," *Optics Letters*, vol. 22, pp. 75–77, 1997.
- [155] G. A. Turnbull, T. J. Edwards, M. H. Dunn, and M. Ebrahimzadeh, "Continuous-wave singly-resonant intracavity optical parametric oscillator based on periodically-poled LiNbO<sub>3</sub>," *Electronics Letters*, vol. 33, pp. 1817–1818, 1997.
- [156] T. J. Edwards, G. A. Turnbull, M. H. Dunn, M. Ebrahimzadeh, and F. G. Colville, "High-power, continuous-wave, singly resonant, intracavity optical parametric oscillator," *Applied Physics Letters*, vol. 72, pp. 1527–1529, 1998.
- [157] T. J. Edwards, G. A. Turnbull, M. H. Dunn, M. Ebrahimzadeh, H. Karlsson, G. Arvidsson, and F. Laurell, "Continuous-wave singly resonant optical parametric oscillator based on periodically poled RbTiOAsO<sub>4</sub>," *Optics Letters*, vol. 23, pp. 837–839, 1998.
- [158] D. J. M. Stothard, M. Ebrahimzadeh, and M. H. Dunn, "Low-pump-threshold continuous-wave singly resonant optical parametric oscillator," *Optics Letters*, vol. 23, pp. 1895–1897, 1998.

- [159] G. A. Turnbull, D. J. M. Stothard, M. Ebrahimzadeh, and M. H. Dunn, “Transient dynamics of cw intracavity singly resonant optical parametric oscillators,” *IEEE Journal of Quantum Electronics*, vol. 35, pp. 1666–1672, 1999.
- [160] T. J. Edwards, G. A. Turnbull, M. H. Dunn, and M. Ebrahimzadeh, “Continuous-wave, singly-resonant, optical parametric oscillator based on periodically poled KTiOPO<sub>4</sub>,” *Optics Express*, vol. 6, pp. 58–63, 2000.
- [161] A. Carleton, D. J. M. Stothard, I. D. Lindsay, M. Ebrahimzadeh, and M. H. Dunn, “Compact, continuous-wave, singly resonant optical parametric oscillator based on periodically poled RbTiOAsO<sub>4</sub> in a Nd:YVO<sub>4</sub> laser,” *Optics Letters*, vol. 28, pp. 555–557, 2003.
- [162] H. Abitan and P. Buchhave, “Continuous-wave singly resonant optical parametric oscillator placed inside a ring laser,” *Applied Optics*, vol. 42, pp. 6630–6635, 2003.
- [163] D. J. M. Stothard, P.-Y. Fortin, A. Carleton, M. Ebrahimzadeh, and M. H. Dunn, “Comparison of continuous-wave optical parametric oscillators based on periodically poled LiNbO<sub>3</sub> and periodically poled RbTiOAsO<sub>4</sub> pumped internal to a high-power Nd:YVO<sub>4</sub> laser,” *Journal of the Optical Society of America B - Optical Physics*, vol. 20, pp. 2102–2108, 2003.
- [164] R. Lavi, A. Englander, and R. Lallouz, “Highly efficient low-threshold tunable all-solid-state intracavity optical parametric oscillator,” *Optics Letters*, vol. 21, pp. 800–802, 1996.
- [165] U. J. Greiner and H. H. Klingenberg, “Picosecond intracavity optical parametric oscillator,” *Optics Letters*, vol. 22, pp. 43–45, 1997.
- [166] A. Dubois, S. Victori, T. Lépine, P. Georges, and A. Brun, “High-repetition-rate eyesafe intracavity optical parametric oscillator,” *Applied Physics B: Lasers and Optics*, vol. 67, pp. 181–183, 1998.
- [167] Y. Yashkir and H. M. van Driel, “Passively Q-switched 1.57- $\mu\text{m}$  intracavity optical parametric oscillator,” *Applied Optics*, vol. 38, pp. 2554–2559, 1999.

- [168] P. B. Phua, K. S. Lai, and R. Wu, “Multiwatt high-repetition-rate 2- $\mu\text{m}$  output from an intracavity KTiOPO<sub>4</sub> optical parametric oscillator,” *Applied Optics*, vol. 39, pp. 1435–1439, 2000.
- [169] J. E. Nettleton, B. W. Schilling, D. N. Barr, and J. S. Lei, “Monoblock laser for a low-cost, eyesafe, microlaser range finder,” *Applied Optics*, vol. 39, pp. 2428–2432, 2000.
- [170] R. F. Wu, P. B. Phua, K. S. Lai, Y. L. Lim, E. Lau, A. Chng, C. Bonnin, and D. Lupinski, “Compact 21-W 2- $\mu\text{m}$  intracavity optical parametric oscillator,” *Optics Letters*, vol. 25, pp. 1460–1462, 2000.
- [171] R. Dabu, C. Fenic, and A. Stratan, “Intracavity pumped nanosecond optical parametric oscillator emitting in the eye-safe range,” *Applied Optics*, vol. 40, pp. 4334–4340, 2001.
- [172] O. B. Jensen, T. Skettrup, O. B. Petersen, and M. B. Larsen, “Diode-pumped intracavity optical parametric oscillator in pulsed and continuous-wave operation,” *Journal of Optics A: Pure and Applied Optics*, vol. 4, pp. 190–193, 2002.
- [173] W. Zendzian, J. K. Jabczynski, and J. Kwiatkowski, “Intracavity optical parametric oscillator at 1572-nm wavelength pumped by passively Q-switched diode-pumped Nd:YAG laser,” *Applied Physics B: Lasers and Optics*, vol. 76, pp. 355–358, 2003.
- [174] Y. F. Chen, S. W. Chen, Y. C. Chen, Y. P. Lan, and S. W. Tsai, “Compact efficient intracavity optical parametric oscillator with a passively Q-switched Nd:YVO<sub>4</sub>/Cr<sup>4+</sup>:YAG laser in a hemispherical cavity,” *Applied Physics B: Lasers and Optics*, vol. 77, pp. 493–495, 2003.
- [175] W. Yong, Z. Q. Yong, Z. D. Yong, H. Kai, L. Tong, H. Hong, Y. S. Fan, and S. X. Zhi, “High repetition rate pulsed laser of twin wavelengths from KTiOPO<sub>4</sub> optical parametric oscillation,” *Chinese Physics*, vol. 13, pp. 1402–1406, 2004.

- [176] Y. F. Chen, Y. C. Chen, S. W. Chen, and Y. P. Lan, "High-power efficient diode-pumped passively Q-switched Nd:YVO<sub>4</sub>/KTP/Cr<sup>4+</sup>:YAG eye-safe laser," *Optics Communications*, vol. 234, pp. 337–342, 2004.
- [177] Y. F. Chen, S. W. Chen, L. Y. Tsai, Y. C. Chen, and C. H. Chien, "Efficient sub-nanosecond intracavity optical parametric oscillator pumped with a passively Q-switched Nd:GdVO<sub>4</sub> laser," *Applied Physics B: Lasers and Optics*, vol. 79, pp. 823–825, 2004.
- [178] X. Peng, L. Xu, and A. Asundi, "Highly efficient high-repetition-rate tunable all-solid-state optical parametric oscillator," *IEEE Journal of Quantum Electronics*, vol. 41, pp. 53–61, 2005.
- [179] W. Zendzian, J. K. Jabczynski, P. Wachulak, and J. Kwiatkowski, "High-repetition-rate, intracavity-pumped KTP OPO at 1572 nm," *Applied Physics B: Lasers and Optics*, vol. 80, pp. 329–332, 2005.
- [180] M. K. Oshman and S. E. Harris, "Theory of optical parametric oscillation internal to the laser cavity," *IEEE Journal of Quantum Electronics*, vol. QE-4, pp. 491–502, 1968.
- [181] J. Falk, J. M. Yarborough, and E. O. Ammann, "Internal optical parametric oscillation," *IEEE Journal of Quantum Electronics*, vol. QE-7, pp. 359–369, 1971.
- [182] T. Debuisschert, J. Raffy, J.-P. Pocholle, and M. Papuchon, "Intracavity optical parametric oscillator: study of the dynamics in pulsed regime," *Journal of the Optical Society of America B - Optical Physics*, vol. 13, pp. 1569–1587, 1996.
- [183] G. A. Turnbull, M. H. Dunn, and M. Ebrahimzadeh, "Continuous-wave, intracavity optical parametric oscillators: an analysis of power characteristics," *Applied Physics B: Lasers and Optics*, vol. 66, pp. 701–710, 1998.
- [184] P. Buchhave, P. T.-Lichtenberg, W. Hou, U. L. Andersen, and H. Abitan, "Modelling a singly resonant, intracavity ring optical parametric oscillator," *Optics Communications*, vol. 216, pp. 191–197, 2003.

- [185] P. F. Moulton, "Spectroscopic and laser characteristics of Ti:Al<sub>2</sub>O<sub>3</sub>," *Journal of the Optical Society of America B - Optical Physics*, vol. 3, pp. 125–133, 1986.
- [186] E. P. Maldonado and J. N. D. Vieira, "Optimization of the active medium length in longitudinally pumped continuous-wave lasers," *Journal of the Optical Society of America B - Optical Physics*, vol. 12, pp. 2482–2485, 1995.
- [187] R. L. Aggarwal, A. Sanchez, M. M. Stuppi, R. E. Fahey, A. J. Strauss, W. R. Rapoport, and C. P. Khattak, "Residual infrared absorption in as-grown and annealed crystals of Ti:Al<sub>2</sub>O<sub>3</sub>," *IEEE Journal of Quantum Electronics*, vol. 24, pp. 1003–1008, 1988.
- [188] I. T. McKinnie, A. L. Oien, D. M. Warrington, P. N. Tonga, L. A. W. Gloster, and T. A. King, "Ti<sup>3+</sup> ion concentration and Ti:sapphire laser performance," *IEEE Journal of Quantum Electronics*, vol. 33, pp. 1221–1230, 1997.
- [189] A. E. Siegman, *Lasers*. University Science Books, 1986.
- [190] J. T. Verdeyen, *Laser Electronics*. Prentice-Hall, 1995.
- [191] J. M. Eggleston, L. G. DeShazer, and K. W. Kangas, "Characteristics and kinetics of laser-pumped Ti:sapphire oscillators," *IEEE Journal of Quantum Electronics*, vol. QE-24, pp. 1009–1015, 1988.